Università
Ca'Foscari
Venezia

Doctoral Thesis

Improving long-term aerosol observing capabilities in polar areas

Author:
Simone Pulimeno

Supervisor:
Ch.Prof. Andrea Gambaro
Dr. Mauro Mazzola
Dr. Giovanni Muscari

A thesis submitted in fulfillment of the requirements for the degree of Doctor of Philosophy

in

Polar Sciences

Department of Environmental Sciences, Informatics and Statistics

Abstract

The primary objective of this doctoral thesis was to develop and test the applicability of optical techniques for studying aerosol properties in polar regions, their integrated use for the study of atmospheric phenomena involving particulate matter in polar regions and the characterization of their climatology in these remote areas.

The mail technique under study was photometry, used with Sun and Moon as radiation source in order to infer optical properties of the columnar aerosols. If until a few years ago it was not possible to obtain such information during the polar night, now with the development of lunar photometry, it is possible to fill this knowledge gap, with important implications for the evaluation of indirect (cloud mediated) aerosol radiative forcing. Beside that, also measurements of scattering and absorption properties of particles obtained with *in situ* instrumentation have been used, together with particle collection on filters for chemical characterization.

This work resulted in the publication of three scientific articles in international peer-review journals, which constitutes 3 of the chapters of this thesis (Chapter 4 to Chapter 6). They are reported here in publication chronological order.

The structure of this thesis is as follows: Chapter 1 provide an introduction to atmospheric aerosols, their sources, their formation and removal processes, their radiative effects, and on how they can be transported to the Arctic; Chapter 2 gives an overview of the optical and radiative properties and parameters of atmospheric aerosols (AOD, Ångström exponent, single scattering albedo, etc.), responsible for the determination of their radiative (climatic) effects; Chapter 3 explains how the photometric techniques work (solar and lunar) in order to obtain the above mentioned optical parameters. Chapter 4 reports on the possible detection of biomass burning events occurred in the Arctic during summer and fall 2019 using both optical and chemical measurements taken at Ny-Ålesund, Svalbard. The published paper can be found in Pulimeno et al. (2024). Chapter 5 illustrates how the lunar photometry technique has been for the first time extensively used in the Arctic, using two commercial photometers modified in order to measured the low irradiances coming from the Moon. The published paper can be found in Mazzola et al. (2024). Chapter 6 is an update of the climatologies of aerosol optical properties from polar regions published in the framework of the Polar-AOD network Tomasi et al. (2007, 2012, 2015). The paper is currently under public discussion at Pulimeno et al. (2025). Finally, Chapter 7 draws some conclusions.

Bibliography

Mazzola, M., Stone, R. S., Kouremeti, N., Vitale, V., Gröbner, J., Stebel, K., Hansen, G. H., Stone, T. C., Ritter, C., and Pulimeno, S. (2024). Monitoring aerosol optical depth during the arctic night: Instrument development and first results. *Atmospheric Research*, 311:107667.

Pulimeno, S., Bruschi, F., Feltracco, M., Mazzola, M., Gilardoni, S., Crocchianti, S., Cappelletti, D., Gambaro, A., and Barbaro, E. (2024). Investigating the presence of biomass burning events at ny-Ålesund: Optical and chemical insights from summer-fall 2019. *Atmospheric Environment*, 320:20336.

Pulimeno, S., Lupi, A., Vitale, V., Frangipani, C., Toledano, C., Kazadzis, S., Kouremeti, N., Ritter, C., Graßl, S., Stebel, K., Fioletov, V., Abboud, I., Blindheim, S., Ma, L., O'Neill, N., Sobolewski, P., Gupta, P., Lind, E., Eck, T. F., Hyvärinen, A., Aaltonen, V., Kivi, R., Csavina, J., Kabanov, D., Sakerin, S. M., Sidorova, O. R., Stone, R. S., Telg, H., Riihimaki, L., Cordero, R. R., Radenz, M., Engelmann, R., Van Roozendal, M., Chaikovsky, A., Goloub, P., Hisamitsu, J., and Mazzola, M. (2025). Recent advances in aerosol optical depth measurements in polar regions: Insights from the polar-aod program. *EGUsphere*, 2025:2527.

Tomasi, C., Kokhanovsky, A. A., Lupi, A., Petkov, B., Vitale, V., Yela, M., Blarel, L., Guirado, C., Berjón, A. J., Almansa, A. F., Cuevas, E., Barreto, , and Román, R. (2015). Aerosol remote sensing in polar regions. *Earth-Science Reviews*, 140:108–157.

Tomasi, C., Lupi, A., Mazzola, M., Stone, R. S., Dutton, E. G., Herber, A., Radionov, V., Holben, B. N., Sorokin, M., Sakerin, S. M., Twerpugova, S. A., Lanvonelli, C., Petkov, B., and Vitale, V. (2012). An update of the long-term trend of aerosol optical depth in the polar regions using polar-aod measurements performed during the international polar year. *Atmospheric Environment*, 52:29–47.

Tomasi, C., Vitale, V., Lupi, A., Di Carmine, C., Campanelli, M., Herber, A., Treffeisen, R., Stone, R. S., Andrews, E., Sharma, S., Radionov, V., von Hoyningen-Huene, W., Stebel, K., Hansen, G. H., Myhre, C. L., Wehrli, C., Aaltonen, V., Lihavainen, H., Virkkula, A., Hillamo, R., Ström, J., Toledano, C., Cachorro, V. E., Ortiz, P., de Frutos, A. M., Blindheim, S., Frioud, M., Gausa, M., Zielinski, T., Petelski, T., and Yamanouchi, T. (2007). Aerosols in polar regions: A historical overview based on optical depth and in situ observations. *Journal of Geophysical Research: Atmospheres*, 112(D16):D16205.

Contents

Chapter 1

Introduction

1.1 The atmospheric aerosols

Atmospheric aerosols constitute a mixture of particles suspended in the air, which may exist in liquid or solid form. These particles can originate from natural sources such as dust, sea salt, volcanic ash, and pollen, or from anthropogenic activities such as industrial emissions. Aerosols can be categorized as primary when directly released into the atmosphere or secondary when formed through chemical reactions involving atmospheric gases.

Their concentration varies from a few milligrams per cubic meter in clean air to several thousand milligrams per cubic meter in heavily polluted atmospheres. These particles can be naturally removed from the atmosphere through various processes, including gravitational settling, coagulation, condensation, and precipitation.

The residence time of aerosols in the atmosphere ranges from minutes to weeks in the troposphere and can extend to several years if the particles reach the stratosphere, as seen, for example, during volcanic eruptions.

This chapter provides an overview of current knowledge regarding atmospheric aerosols primary mechanisms influencing their formation and removal from the atmosphere.

1.2 Sources and formation

Aerosols arise from both natural and anthropogenic sources, whose relative contributions vary across regions and timescales. Volcanic eruptions, for example, inject large quantities of ash and sulfate precursors into the atmosphere, while oceanic processes produce sea salt aerosols through bubble-bursting at the sea surface. Mineral dust mobilized from arid and semi-arid landscapes represents another dominant natural component, and wildfires contribute substantial amounts of organic and black carbon. Human activities, however, have markedly increased the global aerosol burden since the industrial era. Fossil fuel combustion and industrial emissions release sulfates, nitrates, soot, and organic matter, while agricultural practices emit ammonia and particulates that lead to secondary aerosol formation. Biomass burning, both intentional and accidental, adds to this anthropogenic fraction. The combined influence of these natural and human-derived sources shapes the abundance, composition, and impacts of atmospheric aerosols (Figure 1.1).

As seen, natural sources of aerosols encompass a variety of origins. For instance, marine spray introduces aerosol particles into the atmosphere through the bursting of air bubbles generated by wave motion. This source is estimated to contribute significantly to aerosol production, including coarse particles exceeding a diameter of 2.5 μm, although with limited dispersion due to rapid gravitational deposition.

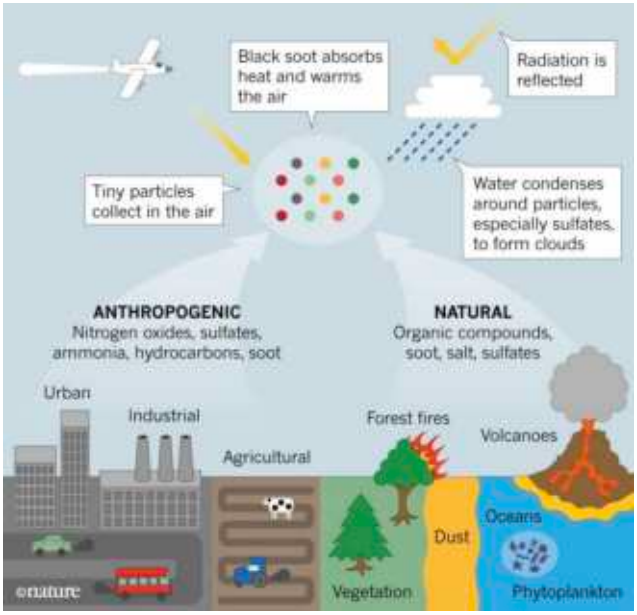

FIGURE 1.1: Diagram showing how tiny particles in the air, called aerosols, are let out and what they do in the atmosphere, based on Penner 2019.

Sea salt particles, predominantly abundant, pose challenges in precise quantification (Monahan et al. 1986). Wind-driven erosion of soil and rocksacts as a pivotal source of mineral dust, originating in arid and semi-arid regions, with particle sizes ranging from 0.1 μm to 10 μm. Dry lakes and their beds also contribute significantly to atmospheric dust (Prospero 1999). Volcanic eruptions release substantial quantities of particles and gases into the troposphere. Violent eruptions can inject significant amounts of gases into the lower stratosphere (15-25 km altitude), playing a crucial role in stratospheric chemistry (Tomasi et al. 2017). Furthermore, plants and animals contribute to biogenic aerosols, which include plant debris like cuticular waxes or leaf fragments, bacterial cells, spores, pollen, etc. Biogenic aerosol particles exhibit a diverse range of shapes and sizes, spanning from 0.1 μm to 250 μm (Tomasi et al. 2017).

Anthropogenic sources constitute a substantial portion of the annual aerosol particle release into the atmosphere. Notably impactful are aerosols generated from anthropogenic combustion processes, involving both fossil and biomass fuels. The magnitude of this emission is projected to double by 2040, primarily attributed to unregulated industrialization in developing nations, particularly China and India (Cooper et al. 2002, Yang et al. 2024). Biofuel combustion, uncontrolled fires, and agricultural field operations also contribute significantly to anthropogenic aerosol sources, emitting a diverse array of compounds and carbonaceous particles (Chung et al. 2005). These phenomena are predominantly prevalent in tropical regions, characterized by frequent and uncontrollable vegetation fires. Various industrial plants play a substantial role as anthropogenic aerosol sources, with metallurgical processes being the most prominent, followed closely by the cement industry. These industrial activities contribute significantly to the release of anthropogenic aerosols into the atmosphere. In the broader context, the contribution of aerosols from natural sources surpasses that of anthropogenic aerosols.

As a consequence of the variegated formation processes associated the different

TABLE 1.1: Global emission estimates of major aerosol sources and precursors. Values are given in teragrams per year (Tg yr^{-1}) or Tg C yr^{-1} / Tg S yr^{-1} where appropriate.

Source / Precursor	Estimated Emission Rate [References]
Natural Sources	
Mineral dust	1,000–4,000 Tg yr^{-1} [IPCC 2013; Textor et al. 2006]
Sea spray (sea salt)	1,400–6,800 Tg yr^{-1} [IPCC 2013; Grythe et al. 2014]
Biogenic VOCs → SOA	20–380 Tg C yr^{-1} [IPCC 2013; Guenther et al. 2012]
Dimethyl sulfide (DMS)	10–40 Tg S yr^{-1} [IPCC 2013; Lana et al. 2011]
Wildfires / biomass burning (OC + BC)	2–5 Tg C yr^{-1} (BC); 17–50 Tg C yr^{-1} (OC) [Bond et al. 2013; van der Werf et al. 2017]
Anthropogenic Sources	
Black carbon (BC)	∼6 Tg C yr^{-1} (2017) [McDuffie et al. 2020]
Organic carbon (OC)	∼13 Tg C yr^{-1} (2017) [McDuffie et al. 2020]
Sulfur dioxide (SO_2)	∼79 Tg S yr^{-1} (2017) [McDuffie et al. 2020]
Ammonia (NH_3)	∼61 Tg yr^{-1} (2017) [McDuffie et al. 2020]

sources of particles, their size distribution can be characterized by a multi-modal model, which involves the summation of log-normal functions of the form

$$n_N(D) = \frac{N}{\sqrt{2\pi} D ln\sigma_g} exp \frac{ln(D/\overline{D})^2}{2ln^2\sigma_g} \tag{1.1}$$

where σ_g is the geometric standard deviation, and $\overline{D}$ is the geometric mean diameter. The distribution is characterized by three distinct diameter ranges: ultrafine particles, with $D < 0.1$ μm (where D is the particle diameter); fine particles, with $D < 1$ μm (and hence including also the ultrafine particles); and coarse particles with $D > 1$ μm (Tomasi et al. 2017). Fig. 1.2 shows the different modes that can be identified in these ranges. Number and volume size distributions are reported in order to make all of them well identifiable.

The volumetric distribution is predominantly influenced by the accumulation mode (involving particles with diameters between 0.1 – 1.0 μm) and the coarse mode (where particles have diameters greater than 1 μm). The accumulation mode combines primary emission processes, condensation from gaseous phases, and coagulation processes from smaller particles. However, in some cases, this mode may consist of two overlapping sub-modes: the condensation sub-mode, resulting from the emission of primary particles and the growth of smaller particles through coagulation/condensation of water vapor on their surfaces, and the droplet sub-mode, which occurs when the accumulation mode of particles takes place within a cloud. The coarse mode, on the other hand, consists of particles that undergo atmospheric transport due to mechanical processes such as wind or erosion. The majority of the material is of primary origin, although secondary origin particles such as sulfates and nitrates are also present.

For the numerical distribution of ultrafine particles, those with a diameter less than 0.1 μm, a separate discussion is warranted. As depicted in the upper panel of Fig. 1.2, these particles exhibit two distinct modes: a nucleation mode, in which atmospheric aerosol particles with a diameter below 0.01 μm form through a process involving the attachment of gaseous monomers until reaching a critical size at which the new particle is thermodynamically stable. On the other hand, the formation of particles with diameters between 0.01 μm and 0.1 μm is dominated by the Aitken mode, wherein aerosol particles form through the condensation of secondary material onto primary origin particles.

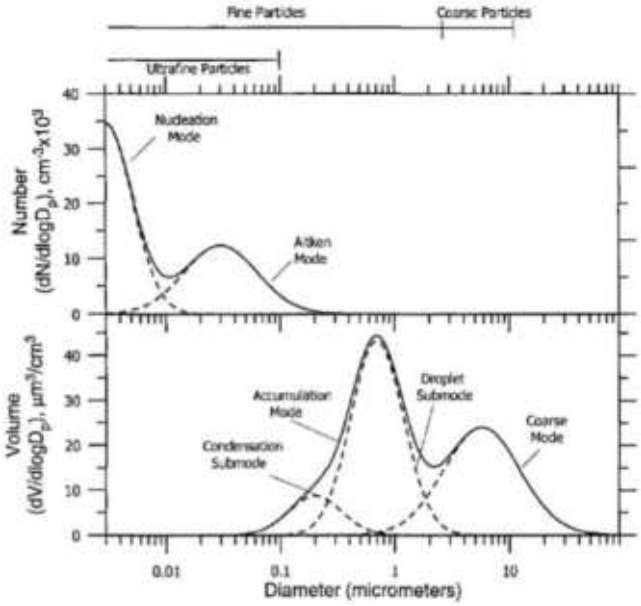

FIGURE 1.2: Representation of number and volume aerosol size distributions. (Seinfeld and Pandis 2006)

Aerosol particles play a crucial role in various meteorological, physical, and chemical processes occurring in the atmosphere. They can alter air conductivity, interact with shortwave solar radiation and longwave terrestrial radiation, impact the condensation process of water vapor into small nuclei, and more (Prospero et al. 1983). Through these processes, aerosol particles affect visibility, contribute to acidifying rainfall, expedite ozone depletion, and directly and indirectly influence the climate. The effects of aerosols on climate are twofold: particles with diameters closely matching the wavelength of visible light (approximately 0.1 – 1.0 μm) strongly interact with solar radiation through optical phenomena, termed direct effects. On the other hand, particles acting as nucleation centers, both in warm and cold clouds, have the ability to interact with the radiative balance through an indirect effect (Bodhaine 1983).

1.3 Removal mechanisms

The atmospheric lifespan of aerosol particles, whether emitted directly from primary sources or formed in the atmosphere through gaseous precursors, is regulated by nucleation, coagulation, condensation, and cloud formation processes. Aerosol removal from the atmosphere can occur through either dry deposition or wet deposition. Airborne aerosol particles undergo transformations in size and composition through processes like coagulation with other particles and condensation from gaseous species.

Generally, smaller particles with a diameter less than 0.1 μm experience coagulation, forming larger particles that are subsequently deposited by gravity. Intermediate-sized particles, ranging from 0.1 μm to 1 μm, exhibit a longer residence time in the atmosphere and can be removed through processes that integrate them into cloud or rain droplets. Coarse particles exceeding 1 μm are predominantly deposited through dry deposition or scavenging processes (atmospheric washing) as illustrated in Figure 1.3. The effectiveness of these removal processes is strongly influenced by the size distribution of the particles and their chemical composition. Deposition, the process

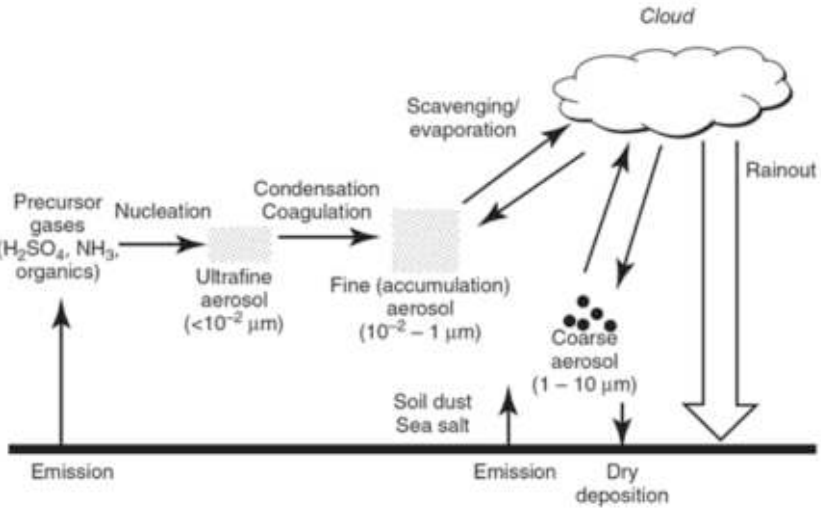

FIGURE 1.3: Processes in the atmospheric life of aerosol particles, from precursor gas emission to removal through dry deposition and wet mechanisms (Tomasi et al. 2017).

by which aerosols settle on solid surfaces, leads to a reduction in their concentration in the atmosphere (Tomasi et al. 2017).

Dry deposition stands out as a crucial atmospheric process, responsible for eliminating trace gases and aerosol particles in the absence of precipitation. However, the efficiency of this removal mechanism hinges on various factors, including atmospheric turbulence levels, the chemical characteristics and water solubility of the particles involved, and the natural terrain features. The quantity of particles deposited through dry deposition notably rises with increased turbulence levels and proximity to the ground. The morphological attributes of the terrain also play a pivotal role in the dry deposition process. In general, a smooth terrain may cause aerosol particles to bounce upon impact, whereas a rough terrain facilitates aerosol removal by impeding their movement. The interaction between these factors contributes to the intricate dynamics of dry deposition in the atmosphere.

In essence, the process of dry deposition involves aerodynamic transport through turbulent diffusion along the atmospheric surface layer to a thin layer of stagnant air adjacent to the surface. Subsequently, Brownian transport takes place through this thin layer of stagnant air until reaching the surface. Brownian transport refers to the movement of particles suspended in a fluid, where they come into contact due to their motion or as a consequence of turbulent or gravitational forces. On the other hand, wet deposition constitutes the second mechanism of removal, encompassing various natural processes through which atmospheric gases and aerosol particles are carried down by atmospheric hydrometeors, such as rain, fog, and snow, and deposited on the ground. Wet deposition occurs through precipitation events, where rain droplets impact the ground; fog deposition, where fog droplets settle and remove particles; and snow deposition, involving the direct removal of aerosols during extreme events like snowstorms. These processes collectively contribute to the comprehensive understanding of the removal mechanisms governing atmospheric aerosols.

1.4 Aerosol Radiative Forcing

Aerosols significantly influence Earth's climate system through their interactions with radiation. These interactions occur via two primary mechanisms: *aerosol-radiation interactions* (ARI) and *aerosol-cloud interactions* (ACI).

Globally, the net aerosol radiative forcing (RF) is predominantly negative, indicating a cooling effect on the climate system. Estimates suggest that the total anthropogenic aerosol RF is approximately -0.9 W m^{-2}, with a 90% confidence interval ranging from -1.9 to 0.1 W m^{-2} (Xian et al. 2020). This negative forcing arises from the combined effects of ARI and ACI, excluding contributions from light-absorbing aerosols on snow and ice.

The direct radiative effect, primarily due to scattering and absorption of solar radiation by all aerosol particles, is estimated at -0.7 ± 0.3 W m^{-2}.

Aerosol-cloud interactions (ACI) occur because aerosols can act as cloud condensation nuclei (CCN) or ice-nucleating particles (INP), thereby modifying cloud microphysical properties and radiative effects (IPCC 2013). The main effects can be described as follows.

First Indirect Effect (Twomey Effect): The presence of additional aerosols increases the number of cloud droplets for a given liquid water content, leading to smaller droplet sizes. Smaller droplets increase cloud reflectivity, resulting in a net cooling effect at the top of the atmosphere. Globally, the first indirect effect is estimated to contribute roughly -0.6 ± 0.4 W m^{-2} to the anthropogenic aerosol radiative forcing (Carslaw and et al. 2013).

Second Indirect Effect (Albrecht Effect): Aerosols can suppress precipitation by producing smaller cloud droplets that are less likely to coalesce into raindrops. This suppression prolongs cloud lifetime and increases cloud fraction, further enhancing the cooling effect. Estimates suggest that this second aerosols indirect effect may contribute an additional -0.3 to -0.5 W m^{-2} globally (Lohmann and Feichter 2000).

Aerosols Semi-Direct Effect: Absorbing aerosols, such as black carbon, can heat the atmosphere locally, which can lead to cloud evaporation or changes in cloud cover. This semi-direct effect can partially offset the cooling caused by the Twomey and Albrecht effects and may contribute between +0.1 and +0.3 W m^{-2} globally (IPCC 2013).

In the Arctic, ACI are particularly important due to the high prevalence of low-level stratiform clouds during summer. Aerosol-induced changes in cloud droplet size and lifetime can significantly modulate the surface energy budget, influencing sea ice melt and the regional radiation balance (Shupe 2011). Observations suggest that even small increases in CCN concentrations can enhance cloud albedo by 5–10% over Arctic summer clouds, with a corresponding reduction in surface solar radiation of 10–20 W m^{-2} (Persson and et al. 2017).

In the Arctic, aerosol radiative forcing exhibits distinct characteristics due to the region's unique environmental conditions. Observations indicate that the net top-of-atmosphere (TOA) aerosol RF has decreased over recent decades, from approximately -0.67 ± 0.06 W m^{-2} in 1980 to -0.19 ± 0.05 W m^{-2} in 2010 (Breider et al. 2017). This trend is largely attributed to reductions in anthropogenic sulfate aerosols.

However, the presence of light-absorbing aerosols, such as black carbon (BC), can lead to positive RF. For instance, during periods of extreme aerosol loading, such as

in August 2017, the Arctic aerosol RF exceeded 0.3 W m^{-2} Shi and et al. 2023. These aerosols contribute to regional warming by reducing surface albedo and enhancing absorption of solar radiation.

Table 1.2 highlights the temporal and spatial variability of aerosol radiative forcing, emphasizing the complex interplay between aerosol composition and climatic impacts.

TABLE 1.2: Global and Arctic aerosol radiative forcing estimates.

Region	**Net Aerosol RF (W m^{-2})**	**Dominant Aerosol Types**
Global	-0.9 (-1.9 to 0.1)	Sulfates, Organic Aerosols
Arctic (1980)	-0.67 ± 0.06	Sulfates
Arctic (2010)	-0.19 ± 0.05	Reduced Sulfates
Arctic (Extreme Events)	> 0.3	Black Carbon, Biomass Burning

1.5 Transport to the Arctic

In the Arctic, significant seasonal variations occur in the concentration of aerosol particles, as well as in their size distribution. Generally, the low Arctic troposphere is effectively insulated due to isentropes forming a closed barrier over the Arctic that is not easily penetrated (Iversen 1984).

During the winter season, the polar front tends to expand towards mid-latitudes, reaching up to 50° N, allowing the entry of particles from major industrial areas in Europe, Asia, and North America into the Arctic region (Treffeisen et al. 2004). Aerosol particles, when transported over snow-covered surfaces, rapidly cool, facilitating their deep penetration into the polar dome in less than a week. Additionally, the extreme dryness of the Arctic troposphere minimizes wet deposition processes, leading to an extended lifespan of particles during this season (Stohl 2006), and causing the Arctic Haze. The accumulation in mid-latitude industrial regions of small particles, presenting dimensions of the same order of magnitude as the incident wavelength, with long atmospheric lifetimes is responsible for this phenomenon. These particles tend to concentrate in the sub-micron size range and contain traces of black carbon and other highly-absorbent particles, exerting a direct warming effect on the polar environment (Shaw 1995). Since the discovery of this phenomenon in the 1950s, there has been an observed reduction in optical depth and aerosol light scattering. This reduction is attributed to the decline in atmospheric pollutant emissions (Bodhaine and Dutton 1993, Breider et al. 2017).

During the summer, the atmospheric circulation pattern undergoes significant changes. The polar front stably lies much farther north, at approximately 70° N, preventing the inflow of air masses from mid-latitudes into the Arctic (Polissar et al. 2001). Additionally, there is often an extensive low-cloud cover, leading to precipitation and facilitating the removal of atmospheric aerosol particles through wet deposition.

A particularly crucial atmospheric circulation pattern for the Arctic region is the North Atlantic Oscillation (NAO). Situated in the Northern Atlantic Ocean, it is characterized by the cyclic fluctuation in sea-level pressure difference between the Azores and Iceland. A semi-permanent low-pressure system (Icelandic low) and a semi-permanent high-pressure center over the Azores (Azores high) control the direction of westerly winds over Europe (Olsen et al. 2012). The relative strength of these two systems varies from year to year, giving rise to NAO variations. It has been

observed that during NAO^+ periods (lower-than-average air pressure over the Arctic and higher-than-average pressure at mid-latitudes), the transport of atmospheric pollution to the Arctic region is further intensified (Hurrell et al. 2003, Christoudias et al. 2012).

Bibliography

Bodhaine, B. A. (1983). Aerosol measurements at four background sites. *Journal of Geophysical Research: Oceans*, 88(C15):10753–10768.

Bodhaine, B. A. and Dutton, E. G. (1993). A long-term decrease in Arctic haze at Barrow, Alaska. *Geophysical Research Letters*, 20(10):947–950. _eprint: https://onlinelibrary.wiley.com/doi/pdf/10.1029/93GL01146.

Bond, T. C., Doherty, S. J., Fahey, D. W., Forster, P. M., Berntsen, T., DeAngelo, B. J., Flanner, M. G., Ghan, S., Kärcher, B., Koch, D., Kinne, S., Kondo, Y., Quinn, P. K., Sarofim, M. C., Schultz, M. G., Schulz, M., Venkataraman, C., Zhang, H., Zhang, S., Bellouin, N., Guttikunda, S. K., Hopke, P. K., Jacobson, M. Z., Kaiser, J. W., Klimont, Z., Lohmann, U., Schwarz, J. P., Shindell, D., Storelvmo, T., Warren, S. G., and Zender, C. S. (2013). Bounding the role of black carbon in the climate system: A scientific assessment. *Journal of Geophysical Research: Atmospheres*, 118(11):5380–5552.

Breider, T., Mickley, L., Jacob, D., Jun Wang, G., Payer Sulprizio, M., Croft, B., Ridley, D., McConnell, J., Sharma, S., Husain, L., Dutkiewicz, V., Eleftheriadis, K., Skov, H., and Hopke, P. (2017). Multidecadal trends in aerosol radiative forcing over the arctic: Contribution of changes in anthropogenic aerosol to arctic warming since 1980. *JGR Atmospheres*, 122(6):3573–3594.

Carslaw, K. S. and et al. (2013). Large contribution of natural aerosols to uncertainty in indirect forcing. *Atmospheric Chemistry and Physics*, 13:2045–2054.

Christoudias, T., Pozzer, A., and Lelieveld, J. (2012). Influence of the north atlantic oscillation on air pollution transport. *Atmospheric Chemistry and Physics*, 12(2):869–877.

Chung, C., Ramanathan, V., Kim, D., and Podgorny, I. (2005). Global Anthropogenic Aerosol Direct Forcing Derived from Satellite and Ground-Based Observations. *Journal of Geophysical Research Atmospheres*, 110, D24207.

Cooper, R. N., Houghton, J. T., McCarthy, J. J., and Metz, B. (2002). Climate Change 2001: The Scientific Basis. *Foreign Affairs*, 81(1):208.

Grythe, H., Ström, J., Krejci, R., Quinn, P., and Stohl, A. (2014). A review of sea spray aerosol source functions using a large global set of sea salt aerosol concentration measurements. *Atmospheric Chemistry and Physics*, 14:1277–1297.

Guenther, A. B., Jiang, X., Heald, C. L., Sakulyanontvittaya, T., Duhl, T., Emmons, L. K., and Wang, X. (2012). The model of emissions of gases and aerosols from nature version 2.1 (megan2.1): an extended and updated framework for modeling biogenic emissions. *Geoscientific Model Development*, 5:1471–1492.

Hurrell, J. W., Kushnir, Y., Ottersen, G., and Visbeck, M. (2003). An Overview of the North Atlantic Oscillation. In *The North Atlantic Oscillation: Climatic Significance and Environmental Impact*, pages 1–35. American Geophysical Union (AGU). _eprint: https://onlinelibrary.wiley.com/doi/pdf/10.1029/134GM01.

IPCC (2013). *Climate Change 2013: The Physical Science Basis. Contribution of Working Group I to the Fifth Assessment Report of the Intergovernmental Panel on Climate Change*. Cambridge University Press, Cambridge, United Kingdom and New York, NY, USA.

Iversen, T. (1984). On the atmospheric transport of pollution to the Arctic. *Geophysical Research Letters*, 11(5):457–460. _eprint: https://onlinelibrary.wiley.com/doi/pdf/10.1029/GL011i005p00457.

Lana, A., Bell, T. G., Simó, R., Vallina, S. M., Ballabrera-Poy, J., Kettle, A. J., Dachs, J., Bopp, L., Saltzman, E. S., Stefels, J., Johnson, J. E., and Liss, P. S. (2011). An updated climatology of surface dimethylsulfide concentrations and emission fluxes in the global ocean. *Global Biogeochemical Cycles*, 25(1).

Lohmann, U. and Feichter, J. (2000). Global indirect aerosol effects: a review. *Atmospheric Chemistry and Physics*, 1:469–478.

McDuffie, E. E., Smith, S. J., O'Rourke, P., Tibrewal, K., Venkataraman, C., Marais, E. A., Zheng, B., Crippa, M., Brauer, M., and Martin, R. V. (2020). A global anthropogenic emission inventory of atmospheric pollutants from sector- and fuel-specific sources (ceds–gbd–maps). *Earth System Science Data*, 12:3413–3442.

Monahan, E. C., Spiel, D. E., and Davidson, K. L. (1986). A Model of Marine Aerosol Generation Via Whitecaps and Wave Disruption. In Monahan, E. C. and Niocaill, G. M., editors, *Oceanic Whitecaps: And Their Role in Air-Sea Exchange Processes*, Oceanographic Sciences Library, pages 167–174. Springer Netherlands, Dordrecht.

Olsen, J., Anderson, N. J., and Knudsen, M. F. (2012). Variability of the North Atlantic Oscillation over the past 5,200 years. *Nature Geoscience*, 5(11):808–812. Number: 11 Publisher: Nature Publishing Group.

Penner, E. (2019). Soot, sulfate, dust and the climate — three ways through the fog. *Nature*, 570:158–159.

Persson, P. O. G. and et al. (2017). Observations of cloud condensation nuclei and their effects on arctic clouds. *Journal of Geophysical Research: Atmospheres*, 122:12345–12360.

Polissar, A., Hopke, P., and Harris, J. (2001). Source regions for atmospheric aerosol measured at Barrow, Alaska. Environmental Science & Technology 35, 4214-4226. Facilities. *Environ. Sci. Technol.*, 38:381–389.

Prospero, J. M. (1999). Long-term measurements of the transport of African mineral dust to the southeastern United States: Implications for regional air quality. *Journal of Geophysical Research*, 104:15,917–15,927. ADS Bibcode: 1999JGR...10415917P.

Prospero, J. M., Charlson, R. J., Mohnen, V., Jaenicke, R., Delany, A. C., Moyers, J., Zoller, W., and Rahn, K. (1983). The atmospheric aerosol system: An overview. *Reviews of Geophysics*, 21(7):1607–1629. _eprint: https://onlinelibrary.wiley.com/doi/pdf/10.1029/RG021i007p01607.

Seinfeld, J. and Pandis, S. (2006). *Atmospheric Chemistry and Physics: From Air Pollution to Climate Change. 2nd Edition*. John Wiley Sons, New York.

Shaw, G. E. (1995). The Arctic Haze Phenomenon. *Bulletin of the American Meteorological Society*, 76(12):2403–2414. Publisher: American Meteorological Society Section: Bulletin of the American Meteorological Society.

Shi, X. and et al. (2023). Observations of extreme aerosol radiative forcing events in the arctic. https://ntrs.nasa.gov/api/citations/20230017807/downloads/AGUslides_2023_Xian.pdf.

Shupe, M. (2011). Clouds at arctic atmospheric observatories. *Atmospheric Research*, 104-105:1–12.

Stohl, A. (2006). Characteristics of atmospheric transport into the Arctic troposphere. *Journal of Geophysical Research: Atmospheres*, 111(D11). _eprint: https://onlinelibrary.wiley.com/doi/pdf/10.1029/2005JD006888.

Textor, C., Schulz, M., Guibert, S., Kinne, S., Balkanski, Y., Bauer, S., Berntsen, T., Berglen, T. F., Boucher, O., Chin, M., Dentener, F., Diehl, T., Easter, R., Feichter, J., Fillmore, D., Ghan, S., Ginoux, P., Gong, S., Grini, A., Hendricks, J., Horowitz, L., Huang, P., Isaksen, I., Iversen, T., Kloster, S., Koch, D., Kirkevåg, A., Kristjansson, J. E., Krol, M., Lauer, A., Lamarque, J. F., Liu, X., Montanaro, V., Myhre, G., Penner, J., Pitari, G., Reddy, M. S., Seland, , Stier, P., Takemura, T., and Tie, X. (2006). Analysis and quantification of the diversities of aerosol life cycles within aerocom. *Atmospheric Chemistry and Physics*, 6:1777–1813.

Tomasi, C., Fuzzi, Sandro, A., and Kokhanovsky, A. (2017). Primary and Secondary Sources of Atmospheric Aerosol. In *Atmospheric Aerosols*, pages 1–86. John Wiley & Sons, Ltd. Section: 1 _eprint: https://onlinelibrary.wiley.com/doi/pdf/10.1002/9783527336449.ch1.

Treffeisen, R., Herber, A., Ström, J., Shiobara, M., Yamanouchi, T., Yamagata, S., Holmén, K., Kriew, M., and Schrems, O. (2004). Interpretation of Arctic aerosol properties using cluster analysis applied to observations in the Svalbard area. *Tellus B: Chemical and Physical Meteorology*, 56(5):457–476. Publisher: Taylor & Francis _eprint: https://doi.org/10.3402/tellusb.v56i5.16469.

van der Werf, G. R., Randerson, J. T., Giglio, L., van Leeuwen, T. T., Chen, Y., Rogers, B. M., Mu, M., van Marle, M. J. E., Morton, D. C., Collatz, G. J., Yokelson, R. J., and Kasibhatla, P. S. (2017). Global fire emissions estimates during 1997–2016. *Earth System Science Data*, 9:697–720.

Xian, Y., Robock, A., and et al. (2020). Global and arctic effective radiative forcing of anthropogenic gases and aerosols in mri-esm2.0. *Progress in Earth and Planetary Science*, 7:38.

Yang, Y., Mou, S., Wang, H., Wang, P., Li, B., and Liao, H. (2024). Global source apportionment of aerosols into major emission regions and sectors over 1850-2017. *Atmospheric Chemistry and Physics*, 24(11):6509–6523.

Chapter 2

Properties of atmospheric aerosol

2.1 Optical properties

The average size of most aerosols is comparable to the wavelength of visible light, which ranges from 390 nm to 700 nm (0.39 μm to 0.70 μm). Optical methods are therefore highly effective for investigating aerosol properties, using instruments deployed on the ground, in the atmosphere, and in space. In these applications, Maxwell's electromagnetic theory is used to model the optical signals measured by different detection systems.

Optical techniques make it possible to gain a detailed understanding of the complex interactions between electromagnetic waves and aerosol particles—whether solid or liquid—within the visible light spectrum (Tomasi et al. 2017). This problem is systematically addressed through a three-step process: (i) the selected instrument calculates the scattering and absorption coefficients for an individual particle, taking into account its shape, internal structure, and chemical composition, based on Maxwell's theory; (ii) the computed coefficients are statistically averaged to account for variations in particle shape, size, and refractive index within a given air volume; (iii) the resulting averaged coefficients are used as input parameters in the radiative transfer equation under specified atmospheric conditions. This approach provides a thorough understanding of the optical behavior of aerosols and their influence on radiative processes in the atmosphere.

Hence, the optical properties of aerosols play a crucial role in field measurements and in estimating radiative forcing, offering valuable insights into optical phenomena observed in the atmosphere. Radiative forcing mathematically describes the change in the balance of atmospheric radiation resulting from variations in key atmospheric constituents—such as gases, aerosol particles, or the amount of water in either gaseous or condensed phases—or from changes in Earth–Sun system properties (Haywood and Boucher 2000).

From this perspective, aerosol particles are critical because they can influence Earth's climate through two distinct mechanisms. First, aerosols can directly interact with solar and terrestrial infrared radiation through scattering and absorption processes, resulting in direct radiative forcing (Charlson et al. 1992). Second, they can modify cloud properties and thereby alter the planetary albedo, contributing to indirect radiative forcing (Twomey 1991).

It is important to note that the radiative and optical properties of aerosols are generally modeled under the assumption that particles are homogeneous spheres. While this assumption is valid for wet particles and those formed through gas-to-particle conversion processes, it may not be appropriate for carbonaceous particles, marine salt particles, or soil-derived particles. Accurately describing the effects of non-spherical

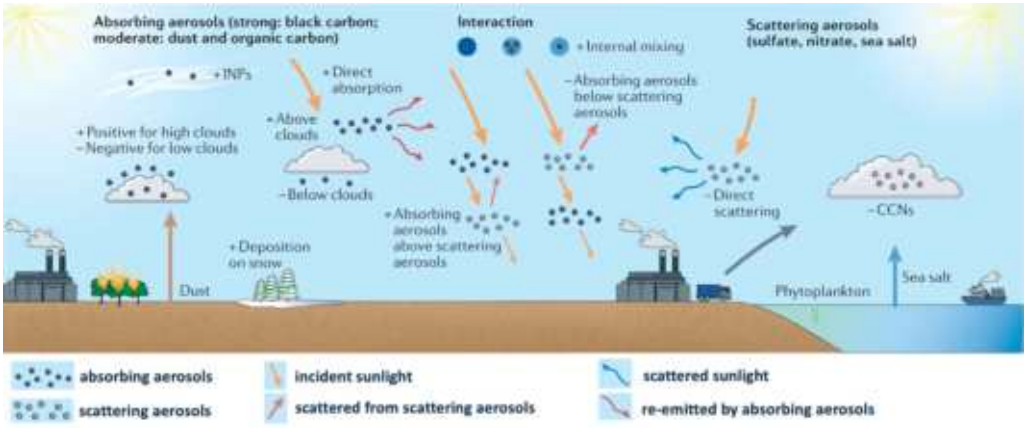

FIGURE 2.1: The radiative effects of aerosols. Schematic of radiative effects of absorbing (dark grey dots) and scattering aerosols (light grey dots), as well as their interactive effects. Light orange arrows represent incident sunlight; dark orange, scattered radiation by scattering aerosols; red, the radiation re-emitted by absorbing aerosols; and dark blue, scattered sunlight. CCN, cloud condensation nuclei; INPs, ice-nucleating particles (Li et al. 2022).

aerosols is practically impossible due to the wide variety of shapes and sizes present in the atmosphere (Iqbal 1983).

Figure 2.1 illustrates the difference between scattering aerosols and absorbing aerosols, shown as light grey and dark grey dots, respectively. Scattering aerosols, such as sulfates, nitrates, and sea salt, are typically similar in size to visible wavelengths, which makes them highly effective at scattering light, especially in the ultraviolet range. However, their scattering efficiency decreases with increasing wavelength. Among the various interactions between atmospheric aerosols and incoming solar radiation, scattering is the dominant mechanism. When a layer of scattering aerosols exists in isolation—such as that depicted on the right side of Figure 2.1 — it increases the fraction of radiation reflected back into space. This results in a net cooling effect, known as negative radiative forcing, which contributes to a reduction in atmospheric temperatures.

Absorbing aerosols, such as black carbon (BC), dust, and organic carbon, have the opposite effect of scattering aerosols. Among these, BC is the most strongly absorbing aerosol present in the atmosphere. Unlike scattering aerosols, absorbing aerosols contribute to positive radiative forcing, resulting in a net warming effect. However, the magnitude of this warming depends on atmospheric conditions, particularly the presence and position of clouds. When absorbing aerosols are located below a cloud layer, their warming effect is reduced because a portion of the incoming solar radiation is scattered back into space by the clouds. Conversely, if the absorbing aerosol layer is situated above the clouds, it not only absorbs direct solar radiation but also captures some of the radiation reflected by the clouds, thereby enhancing the warming effect. This makes the overall impact of absorbing aerosols more complex and highly dependent on their vertical distribution. In addition, absorbing aerosols can deposit on bright surfaces such as ice or snow, where they absorb solar radiation and accelerate surface melting.

The role of atmospheric aerosols depends not only on their optical properties but also on their surrounding environment. Adding to this complexity, scattering and

absorbing aerosols can interact with each other, further modifying their radiative effects. For example, when black carbon (BC) is internally mixed with biomass burning aerosols, its absorption capacity increases significantly compared to its pure form. The vertical positioning of aerosol layers in the atmosphere also plays a crucial role in determining their overall impact. If an absorbing aerosol layer is located above a scattering layer, absorption is enhanced through the same mechanism observed when an absorbing layer lies above clouds. In contrast, when a scattering layer is positioned above an absorbing layer, the absorption effect is reduced, as part of the incoming radiation is scattered before it can be absorbed.

In the atmosphere, aerosols can also interact with clouds, altering their properties and influencing the climate. For example, sulfate and other water-soluble aerosols can act as cloud condensation nuclei (CCNs), modifying the macro-physical characteristics of clouds. By increasing the number of droplets within a cloud, these aerosols can enhance its liquid water content, which strengthens the cloud's cooling effect. However, smaller droplets tend to evaporate more easily, and under certain conditions, additional processes can reduce the overall liquid water content, potentially resulting in a warming effect instead.

Another complex interaction, illustrated in Figure 2.1, occurs when aerosols act as ice-nucleating particles (INPs). The impact of INPs depends on the dominant freezing processes within clouds. In cases of heterogeneous freezing, the presence of INPs promotes ice crystal formation, leading to a warming effect. Conversely, in clouds dominated by homogeneous freezing, the addition of INPs reduces the number of ice crystals, resulting in a net cooling effect. These complex interactions contribute to considerable uncertainties in quantifying the role of aerosols in critical climate processes, such as Earth's radiation budget, climate change, and atmospheric forecasting models.

2.2 Scattering, absorption, and extinction coefficient

When solar radiation enters the Earth's atmosphere, its intensity is reduced by the combined effects of scattering and absorption by atmospheric gases and particles. This reduction in intensity is called extinction. The phenomenon of extinction is mathematically described by the Beer-Lambert Law:

$$I_\lambda = \frac{I_{0,\lambda}}{R^2} e^{-\tau_\lambda m} \tag{2.1}$$

The signal measured at wavelength λ is denoted as I_λ. The theoretical signal measured at the top of the atmosphere (TOA) at the mean Earth-Sun distance r_0 is represented by $I_{0,\lambda}$.The atmospheric parameters influencing the measurement include the relative optical air mass, denoted by m, and the atmospheric total optical depth, denoted by τ_λ. Furthermore, the ratio R between the actual Earth-Sun distance r and r_0 accounts for the Earth's orbit and is numerically equivalent to the Sun-Earth distance expressed in astronomical units (AU).

When a beam of light strikes a particle, the electric charges within the particle begin to oscillate. These excited charges re-radiate energy in all directions, causing scattering, and may convert a portion of the incident radiation energy into thermal energy through absorption. The energy scattered by a particle is proportional to the intensity of the incident radiation by the scattering cross-section of the particle C_s, expressed in m^2. For absorption, the absorbed energy is determined in an entirely analogous manner, with C_a (in m^2) indicating the absorption cross-section of the

particle. The theory of conservation of energy states that the energy removed from the incident light beam is equal to the sum of the energy scattered and the energy absorbed by the particle. The combined effect of scattering and absorption is referred to as extinction and can be defined as:

$$C_{ext} = C_s + C_a \tag{2.2}$$

With C_s having dimensions of an area, we can subsequently define the scattering efficiency of the particle (Q_s), a dimensionless number defined as the ratio C_s/A, where A represents the area of the particle's cross-section. Similarly, defining Q_a and Q_{ext}, we get:

$$Q_{ext} = Q_s + Q_a. \tag{2.3}$$

See Chapter 4 for an application of measurements of aerosol absorption coefficient for the characterization of biomass burning events.

2.3 Single Scattering Albedo (SSA)

The ratio between Q_s (the scattering efficiency of particle) and Q_{ext} (the extinction efficiency of particles) defines the Single Scattering Albedo ω:

$$\omega = \frac{Q_s}{Q_{ext}} = \frac{C_s}{C_{ext}}. \tag{2.4}$$

The fraction of attenuated radiation that has been scattered by the particle is then equal to ω, while the fraction absorbed is 1 - ω (Seinfeld and Pandis 2016). The scattering mechanism of a particle can be divided into three categories: (i) *elastic scattering*, where the wavelength of the scattered light is equal to that of the incident beam, λ_0; (ii) *quasi-elastic scattering*, where the wavelength shifts due to the Doppler effect; (iii) *inelastic scattering*, where the radiation emitted by the particle has a wavelength different from that of the incident radiation. Figure 2.2 illustrates the various processes that can occur when radiation with wavelength λ_0 interacts with a particle. For the interaction of solar radiation with atmospheric aerosol particles, elastic scattering is the primary process of interest.

The energy scattered by spherical particles can be theoretically obtained by solving Maxwell's electromagnetic wave equation in spherical polar coordinates. A simplified solution arises when the particle is spherical and much smaller than the wavelength of the incident radiation (diameter $D = 0.2\lambda$). This approximation is described by Rayleigh's theory, which is particularly useful for studying the scattering of solar radiation by air molecules.

For example, the Sun appears weaker and redder during the evening because its energy is attenuated while passing through the atmosphere, primarily affecting the shorter (blue and green) wavelengths. For the same reason, when observing the sky it looks blue, as these wavelengths are scattered more effectively. Therefore, in this case, scattering contributes to the extinction of light rather than absorption.

The absorption and elastic scattering of light by spherical particles with sizes comparable to the incident wavelength is a classical problem in physics. This problem was solved by the mathematical formulation known as Mie theory, of which Rayleigh's solution is a special case.

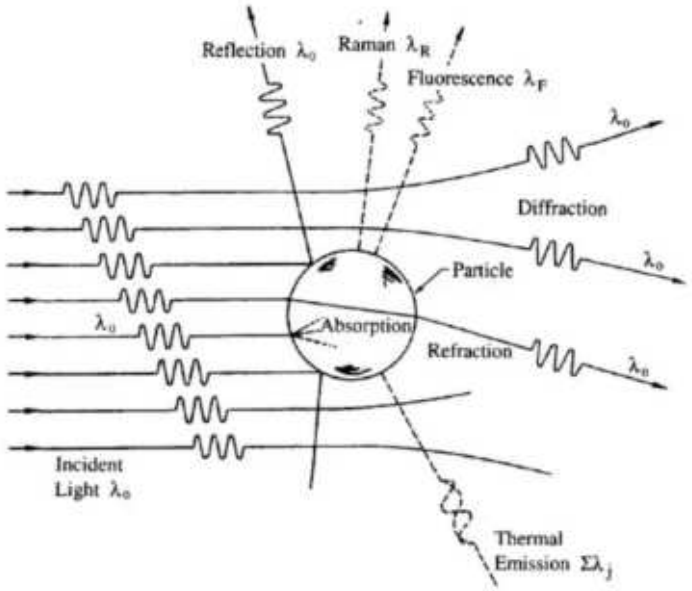

FIGURE 2.2: Mechanisms of interaction between radiation and a particle (Seinfeld and Pandis 2016).

2.4 Aerosol Optical Depth (AOD)

The Aerosol Optical Depth (AOD) stands as a crucial parameter, delineating the quantity of aerosol particles within a column of air extending from the instrument, notably a photometer, to the top of the atmosphere (TOA). As light traverses the atmosphere, it undergoes attenuation owing to interactions with atmospheric constituents . This attenuation finds quantification through the Lambert-Beer equation, previously delineated in Section 2.2, and also reported here:

$$I_\lambda = \frac{I_{0,\lambda}}{R^2} e^{-\tau_\lambda m} \tag{2.5}$$

Eq. 2.5 enables the derivation of the AOD by subtracting the contribution to extinction due to Rayleigh scattering and absorption by gases. This necessitates consideration of several air mass factors m for various species, owing to their differing vertical distributions within the atmosphere. For instance, ozone predominantly resides in the stratosphere, while carbon dioxide is uniformly mixed throughout. Consequently, Eq. 2.5 can be reformulated as:

$$\ln I_\lambda = \ln \frac{I_{0,\lambda}}{R^2} - [\tau_{a,\lambda} m_a + \tau_{R,\lambda} m_R + \tau_{g,\lambda} m_g] \tag{2.6}$$

Here, $\tau_{a,\lambda} m_a$ represents the contribution of aerosols to the TOD, $\tau_{R,\lambda} m_R$ express the contribution attributed to scattering, and $\tau_{g,\lambda} m_g$ denotes the contribution attributed to gas absorption. Finally, the AOD (τ_a) can be directly derived from Eq. 2.6 as:

$$\tau_{a,\lambda} = -\frac{1}{m_a} \left[\ln \left(\frac{I_\lambda}{I_{0,\lambda} R^{-2}} \right) - \tau_{R,\lambda} m_R - \tau_{g,\lambda} m_g \right] \tag{2.7}$$

The gaseous species considered in the absorption process tipically are nitrogen dioxide (NO_2), water (H_2O), carbon dioxide (CO_2), and methane (CH_4).

2.5 Ångström Exponent

The *Ångström exponent* (α) is a key parameter used to characterize the spectral dependence of aerosol optical thickness (AOT, τ) and provides information about the size distribution of atmospheric aerosols. For spherical particles, it is defined by the empirical relationship:

$$\tau(\lambda) = \beta\,\lambda^{-\alpha} \tag{2.8}$$

where β is the turbidity coefficient, related to the aerosol load, and α is the Ångström exponent, which quantifies the wavelength dependence.

High values of α (typically > 1) indicate dominance of fine-mode particles (e.g., urban pollution, biomass burning), while low values of α (typically < 1) are associated with coarse-mode particles (e.g. sea spray) Ångström 1929; Holben et al. 1998.

The Ångström exponent is commonly estimated from multi-wavelength sun photometer measurements of AOT. Taking logarithms of the Ångström formula gives a linear relationship:

$$\ln\tau(\lambda) = \ln\beta - \alpha\ln\lambda \tag{2.9}$$

Thus, α can be obtained from a linear regression of $\ln\tau$ versus $\ln\lambda$ using measurements at two or more wavelengths. Typically, in Sun photometry the two channels centered at 440 and 870 nm are used in the two wavelengths formula:

$$\alpha = -\frac{\ln\tau(\lambda_1) - \ln\tau(\lambda_2)}{\ln\lambda_1 - \ln\lambda_2} \tag{2.10}$$

where λ_1 and λ_2 are the selected wavelengths (i.e., 440 and 870 nm).

When more than two wavelengths are available, a least-squares fit over all measured wavelengths provides a more robust estimate of α (Holben et al. 1998; Liou 2002).

See Chapter 6 for an update of the climatologies of AOD and α in polar regions.

2.6 Further Aerosol Optical Properties

In addition to aerosol optical thickness and Ångström exponent, sun photometers and sky radiometers allow the retrieval of further aerosol optical properties, including size distribution, phase function, and complex refractive index. These parameters are critical for understanding aerosol radiative effects and their role in climate.

Sky radiance measurements, typically taken at multiple angles around the sun (e.g., Almucantar and plan parallel scans) or across the sky dome, provide the angular distribution of scattered sunlight. The measured radiance, $I(\theta,\lambda)$, depends on the aerosol size distribution, $n(r)$, the phase function, $P(\theta,r,\lambda)$, and the complex refractive index, $m(\lambda) = n - ik$, according to the radiative transfer equation:

$$I(\theta,\lambda) = \int_0^\infty n(r)\,P(\theta,r,\lambda)\,Q_{\text{ext}}(r,\lambda,m)\,dr \tag{2.11}$$

where r here is the particle radius, Q_{ext} is the extinction efficiency, and θ is the scattering angle (Holben et al. 1998; Louka et al. 2000).

By fitting radiative transfer simulations to measured sky radiances at multiple wavelengths, inversion algorithms (e.g., using Mie theory for spherical particles) can retrieve the volume size distribution and complex refractive index of the aerosols. The

phase function, describing the angular scattering probability, is also constrained by the directional radiance measurements. These retrievals typically assume homogeneous, externally mixed aerosols, and errors increase for highly absorbing or nonspherical particles. Single scattering albedo ω is another parameter that can be obtained by such method.

Such measurements provide essential input for modeling aerosol radiative forcing, interpreting satellite observations, and assessing regional climate impacts (Dubovik et al. 2002). In particular, the combination of spectral and angular sky radiance data allows distinguishing fine-mode anthropogenic aerosols from coarse natural aerosols such as dust or sea salt, based on their size-dependent scattering and absorption properties.

Bibliography

Charlson, R., Schwartz, S., Hales, J., Cess, R., Coakley, J., Hansen, J., and Hofmann, D. (1992). Climate Forcing by Anthropogenic Aerosols. *Science (New York, N.Y.)*, 255:423–30.

Dubovik, O., Holben, B. N., Eck, T. F., Smirnov, A., Kaufman, Y. J., King, M. D., Tanré, D., and Slutsker, I. (2002). Variability of absorption and optical properties of key aerosol types observed in worldwide locations. *Journal of the Atmospheric Sciences*, 59:590–608.

Haywood, J. and Boucher, O. (2000). Estimates of the direct and indirect radiative forcing due to tropospheric aerosols: A review. *Reviews of Geophysics*, 38.

Holben, B. N., Eck, T. F., Slutsker, I., Tanré, D., Buis, J. P., Setzer, A., Vermote, E., Reagan, J. A., Kaufman, Y. J., Nakajima, T., Lavenu, F., Jankowiak, I., and Smirnov, A. (1998). Aeronet—a federated instrument network and data archive for aerosol characterization. *Remote Sensing of Environment*, 66:1–16.

Iqbal, M. (1983). *An Introduction To Solar Radiation - 1st Edition*. Elsevier Science.

Li, J., Carlson, B. E., Yung, Y. L., Lv, D., Hansen, J., Penner, J. E., Liao, H., Ramaswamy, V., Kahn, R. A., Zhang, P., Dubovik, O., Ding, A., Lacis, A. A., Zhang, L., and Dong, Y. (2022). Scattering and absorbing aerosols in the climate system. *Nature Reviews Earth & Environment*, 3(6):363–379.

Liou, K. N. (2002). *An Introduction to Atmospheric Radiation*. Academic Press, San Diego, CA, USA, 2nd edition.

Louka, P., Karol, I., and Holben, B. N. (2000). Retrieval of aerosol optical properties from sky radiance measurements: Comparison of different inversion methods. *Applied Optics*, 39:5477–5486.

Seinfeld, J. H. and Pandis, S. N. (2016). *Atmospheric Chemistry and Physics: From Air Pollution to Climate Change, 3rd Edition | Wiley*. John Wiley & Sons.

Tomasi, C., Fuzzi, Sandro, A., and Kokhanovsky, A. (2017). Primary and Secondary Sources of Atmospheric Aerosol. In *Atmospheric Aerosols*, pages 1–86. John Wiley & Sons, Ltd. Section: 1 _eprint: https://onlinelibrary.wiley.com/doi/pdf/10.1002/9783527336449.ch1.

760 Twomey, S. (1991). Aerosols, clouds and radiation. *Atmospheric Environment. Part*
761 *A. General Topics*, 25(11):2435–2442.

762 Ångström, A. (1929). On the atmospheric transmission of sun radiation and on dust
763 in the air. *Geografiska Annaler*, 11:156–166.

Chapter 3

Aerosol Retrieval with Photometry

A photometer is an optical instrument designed to measure the intensity of radiation, and in atmospheric applications, a sun photometer specifically measures the direct solar irradiance at selected wavelengths. By comparing the measured solar signal with the extraterrestrial solar irradiance, it allows the determination of the column-integrated aerosol optical depth. A sky radiometer, on the other hand, measures the diffuse radiance of the sky at multiple angles and wavelengths, providing information not only on the total aerosol load but also on aerosol size distribution, scattering phase function, and, when combined with inversion algorithms, the complex refractive index. While the photometer focuses on the direct solar beam to quantify overall extinction, the sky radiometer samples scattered light from different regions of the sky, offering a more detailed characterization of aerosol optical properties.

3.1 Solar photometry technique

As seen, a sun-photometer is an instrument that measures the direct radiation coming from a light source, namely the Sun, at several wavelengths. For doing this, it incorporates (or is installed on) a solar tracker, a device that follow the Sun as it moves during the day, using both theoretic calculation and active sensors. As seen before, the photometry technique relies on the Beer-Lambert law. If we rewrite it in terms of the voltages measured by the instrument, we obtain:

$$V_\lambda = \frac{V_{0,\lambda}}{R^2} e^{-\tau_\lambda m} \tag{3.1}$$

This equation relates the irradiance measured by the instrument at a given wavelength V_λ to the irradiance expected at the top of the atmosphere at the same wavelength $V_{0,\lambda}$. The Beer-Lambert law also accounts for the Earth-Sun distance R expressed in astronomical units, the optical air mass m, which describes the ratio between the slant path and the vertical path of the radiation through the atmosphere, and the total optical thickness τ_λ.

It is worth noting that $V_{0,\lambda}$ corresponds now to the calibration coefficient at wavelength λ, denoting the photometer's output voltage when hypothetically measuring solar irradiance at the TOA at the mean Sun-Earth distance.

In specific high-altitude stations characterized by stable atmospheric conditions, the Langley calibration method can be employed to retrieve the calibration constant $V_{0,\lambda}$ (Schmid and Wehrli 1995). Applying the natural logarithm to the Equation 3.1 yields to:

$$\ln V_\lambda = \ln \frac{V_{0,\lambda}}{R^2} - m\tau_\lambda. \tag{3.2}$$

Essentially, through a linear fitting between $\ln V_\lambda$ and the optical airmass m, we can extrapolate the voltage corresponding to the solar constant to zero-air-mass, typically for m values ranging between 2 and 5. Airmass values lower than 2 are avoided because the rate of change in air mass is small, which increases the chance that changing atmospheric conditions will affect the regression. Airmass values greater than 5 are excluded due to the greater uncertainty in air mass caused by refraction corrections, which become more sensitive to the atmospheric temperature profile (Harrison and Michalsky 1994). The calibration is presumed to remain constant over time, barring variations due to degradation of the instrument sensor or filters. It is therefore recommended to repeat it approximately every year.

3.2 Cloud Screening

Aerosol optical depth (AOD) measurements from ground-based sun photometers and sky radiometers are often affected by the presence of clouds. Clouds can strongly attenuate or scatter solar radiation, leading to overestimation or large variability in AOD. Therefore, careful cloud screening is essential to ensure that AOD represents aerosol properties alone.

Cloud contamination introduces spurious signals in the measured direct solar irradiance and sky radiances, because (i) clouds can partially or fully block the sun, reducing measured irradiance; (ii) multiple scattering within clouds increases sky radiance at off-zenith angles; (iii) rapidly changing cloud cover leads to temporal fluctuations not associated with aerosols.

Without cloud screening, derived aerosol properties such as AOD and Angström exponent may be biased or highly uncertain.

Several methods have been developed and standardized, particularly in the AErosol RObotic NETwork (AERONET) network (Holben et al. 1998). For example, the Triplet Stability Test compares three consecutive measurements at the same wavelength. If the relative variability exceeds a threshold (commonly 1–2%), the data point is flagged as cloud-contaminated. The Excess AOD Test flags measurements where AOD significantly exceeds typical values for the location and season, which may indicate cloud enhancement. When using a sky radiomter, the Angular Sky Radiance Check uses almucantar scans to identify deviations from expected aerosol scattering patterns; large deviations suggest cloud contamination.

Cloud screening substantially reduces noise and bias in AOD datasets, allowing robust retrieval of aerosol optical and microphysical properties. Typical results show that up to 20–30% of raw measurements may be flagged as cloud-affected in regions with variable cloud cover (Smirnov et al. 2000).

3.3 Contribution of Gases to Total Optical Depth

Measurements of total optical depth (TOD) from sun photometers or sky radiometers include not only the extinction by aerosols but also contributions from Rayleigh scattering and gaseous absorbers such as ozone (O_3), nitrogen dioxide (NO_2), and water vapor (H_2O). Accurate aerosol optical depth (AOD) retrieval requires removing these contributions from TOD.

Rayleigh scattering occurs due to the scattering of radiation by air molecules (N_2, O_2). Its contribution to optical depth, $\tau_R(\lambda)$, decreases rapidly with wavelength, approximately following a λ^{-4} dependence:

$$\tau_{\mathrm{R}}(\lambda) \approx \frac{P}{P_0}\left(\frac{\lambda_0}{\lambda}\right)^4 \tau_{\mathrm{R}}(\lambda_0) \tag{3.3}$$

where P is the local atmospheric pressure, P_0 is standard pressure, and λ_0 is a reference wavelength (Bodhaine et al. 1999). Rayleigh scattering is largest in the UV and blue regions, significantly affecting short-wavelength AOD retrievals.

Gaseous absorption affects the measured solar irradiance at specific wavelengths:

- Ozone absorbs especially in the UV-B (280-325 nm).
- Nitrogen dioxide has narrow absorption bands, mainly in the visible (400–450 nm).
- Water vapor absorbs in the near-infrared (e.g., 940 nm).

If uncorrected, these contributions lead to overestimation of AOD, particularly at wavelengths coinciding with strong absorption bands.

Typical correction methods involve the use of spectral windows, selecting wavelengths minimally affected by gas absorption to derive aerosol optical depth (e.g., 440, 675, 870 nm), and use of climatological or satellite-based column abundances to estimate the optical depth of gases:

$$\tau_a(\lambda) = \tau(\lambda) - \sum_i \tau_{g,i}(\lambda) \tag{3.4}$$

where τ is the measured total optical depth, and $\tau_{g,i}$ is the optical depth of the i-th gas absorber (Harrison and Michalsky 1994; Holben et al. 1998).

Combining measurements with radiative transfer calculations is possbile to estimate and subtract gas absorption for each wavelength, particularly for water vapor in the near-infrared.

3.4 Lunar photometry technique

While sun photometers provide high-quality measurements of aerosol optical depth (AOD) during daytime, obtaining comparable information at night requires alternative radiation sources. Lunar photometry utilizes the Moon as a stable and predictable illumination source, allowing the measurement of direct lunar irradiance at selected wavelengths. By applying similar principles as in solar photometry, the observed lunar signal is compared to the extraterrestrial lunar irradiance, corrected for the lunar phase and Earth-Moon distance, to retrieve the column-integrated AOD (Kieffer and Stone 2005; Schmidt and Shaw 2005).

Lunar photometry faces unique challenges, including lower irradiance levels compared to the Sun, phase-dependent spectral variations of lunar reflectance, and higher relative uncertainties due to instrumental noise. Nevertheless, modern instruments and calibration strategies, such as those employed in the Lunar-Langley method (Barreto et al. 2017), enable the derivation of nighttime AOD with sufficient accuracy for climatological and aerosol process studies (Kieffer and Stone 2005; Leon and et al. 2006). Nighttime measurements are particularly valuable in regions with strong diurnal variations of aerosol load or, such as Polar Regions, where the Sun doesn't rise for several months, providing a more complete understanding of aerosol optical properties and their temporal evolution. See Chapter 5 for an application to the Arctic atmosphere.

The main difference between solar and lunar photometry is that the Moon does not emit radiation. Instead, the Moon reflects solar radiation, resulting in a signal that is thousands (with respect to Full Moon) to millions of times (with respect to New Moon) weaker than direct sunlight. To estimate the aerosol optical thickness using moonlight, it is necessary to measure the amount of light reflected by the Moon as observed from space. For this purpose, a model known as the ROLO (RObotic Lunar Observatory) irradiance model was developed (Kieffer and Stone 2005).

The ROLO facility was located at the USGS Field Center campus in Flagstaff, Arizona, USA. It housed two nearly identical telescopes mounted side by side. Both telescopes had an effective focal length of approximately 1 m. The VNIR camera used a 512 × 512 Thomson TH7895 CCD array. Dual filter wheels held 23 passband filters covering wavelengths from 350 nm to 950 nm, each with a bandwidth of about 15 to 20 nm. The SWIR camera was equipped with a 256 × 256 HgCdTe array (Rockwell), similar to the NICMOS camera on the Hubble Space Telescope. Its filter wheel contained nine filters spanning wavelengths from 950 nm to 2350 nm, with one blocked position for acquiring dark frames. Some of these wavelengths were selected for remote sensing applications, while others were chosen for stellar photometry studies. In the latter case, adjacent spectral bands were compared to monitor stellar color variations. The same method was applied consistently for each spectral band.

The ROLO model is based on images of the Moon's brightness collected by the observatory over a period of more than eight years. The uncertainties in the model are generally less than 1%. The parameters of the model were determined using observations taken at lunar phase angles ranging from 1.55° to 97°. The ROLO project, funded by NASA, was developed to provide a means of calibrating Earth Observing System (EOS) satellite instruments using the Moon as a stable reference. The empirically derived analytical expression, based on the primary geometric variables, is given as follows:

$$lnA_k = \sum_{i=0}^{3} a_{ik} g^i + \sum_{j=1}^{3} b_{jk} \Phi^{2j-1} + c_1\phi + c_2\theta + c_3\Phi\phi + c_4\Phi\theta + d_{1k} e^{-g/p_1} + d_{2k} e^{-g/p_2} + d_{3k} cos((g - p_3)/p_4) \tag{3.5}$$

where A_k is the disk-equivalent reflectance, g is the absolute phase angle of the Moon, θ and ϕ are the selenographic latitude and longitude of the observer (in degrees), and Φ is the selenographic longitude of the Sun (in radians).

The first polynomial describes how the brightness varies with the phase angle of the Moon, excluding any opposition effect. The second polynomial estimates the brightness variation due to the distribution of illuminated lunar surface features, primarily capturing the contrast between the dark maria and the bright highlands. The four terms with coefficients c_n account for the appearance of the lunar surface as a function of its illumination geometry. The last three terms, all nonlinear in g, are purely empirical: the first two represent the opposition surge, while the final term accounts for a residual pattern observed in the brightness measurements.

This formula requires careful application because there are known errors in the equation as presented by Kieffer and Stone 2005. In Eq. 3.5, the variables θ and ϕ are interchanged relative to the original intended expression. In addition, the coefficients p_1, p_2, p_3, and p_4 are given in degrees. Therefore, to maintain consistency, the phase angle g in the exponential and cosine terms must be converted to degrees (Uchiyama and et al. 2019).

Due to the much weaker irradiance coming from the Moon compared to that of direct sunlight, this technique can be applied only during a limited period, specifically between the first and third quarters of the lunar cycle, which corresponds to roughly two weeks per month. Outside this range, the Moon's brightness is insufficient to be detected by a lunar photometer and becomes indistinguishable from instrumental noise.

Also, the lunar reflectance in the UV range of the spectra is very low, further limiting the applicability of the lunar photometry technique at these wavelengths.

Bibliography

Barreto, , Román, R., Cuevas, E., Berjón, A. J., Almansa, A. F., Téllez, C., González, R., Hernández, Y., Blarel, L., Goloub, P., Guirado, C., and Yela, M. (2017). Assessment of nocturnal aerosol optical depth from lunar photometry at the izaña high mountain observatory. *Atmospheric Measurement Techniques*, 10(8):3191–3203.

Bodhaine, B. A., Wood, N. B., Dutton, E. G., and Slusser, J. R. (1999). On rayleigh optical depth calculations. *Journal of Atmospheric and Oceanic Technology*, 16:1854–1861.

Harrison, L. and Michalsky, J. (1994). Evaluation of measurement uncertainties for direct solar irradiance and diffuse sky radiation. *Applied Optics*, 33(12):2160–2170.

Holben, B. N., Eck, T. F., Slutsker, I., Tanré, D., Buis, J. P., Setzer, A., Vermote, E., Reagan, J. A., Kaufman, Y. J., Nakajima, T., Lavenu, F., Jankowiak, I., and Smirnov, A. (1998). Aeronet—a federated instrument network and data archive for aerosol characterization. *Remote Sensing of Environment*, 66:1–16.

Kieffer, H. H. and Stone, T. C. (2005). The spectral irradiance of the moon. *The Astronomical Journal*, 110:1477–1488.

Leon, J.-F. and et al. (2006). Lunar photometry for night-time aerosol optical depth retrieval. *Atmospheric Chemistry and Physics*, 6:4573–4585.

Schmid, B. and Wehrli, C. (1995). Comparison of Sun photometer calibration by use of the Langley technique and the standard lamp. *Applied Optics*, 34(21):4500–4512. Publisher: Optica Publishing Group.

Schmidt, C. and Shaw, G. E. (2005). Nighttime aerosol optical depth measurements using lunar photometry. *Applied Optics*, 44:539–548.

Smirnov, A., Holben, B. N., Slutsker, I., Eck, T. F., Dubovik, O., Kaufman, Y. J., Pietras, C., and Nakajima, T. (2000). Cloud-screening and quality control algorithms for the aeronet database. *Remote Sensing of Environment*, 73:337–349.

Uchiyama, A. and et al. (2019). Nocturnal aerosol optical depth measurements with modified sky radiometer pom-02 using the moon as a light source. *Atmospheric Measurement Techniques*, 12:6465–6488.

Chapter 4

Investigating the presence of Biomass Burning events at Ny-Ålesund: optical and chemical insights from summer-fall 2019

Atmospheric aerosols are an important part of the Earth's climate system because they interact in multiple ways with incoming solar radiation. In this first research paper, we explored how to study atmospheric aerosols effectively by combining both their optical and chemical properties. The study focused on whether the intense biomass burning events of summer 2019 in the Northern Hemisphere could be detected at the Gruvebadet Atmospheric Laboratory (GAL) near Ny-Ålesund, Svalbard, during the second half of 2019. To address this, we integrated optical measurements, chemical analyses, and air mass back-trajectory modeling to identify and characterize biomass burning aerosols in the Arctic region. The results showed that, although twelve potential biomass burning events were detected, their contribution to the total aerosol mass concentration was very small (only 2%, as estimated by Positive Matrix Factorization). Events in early summer were mainly linked to North American wildfires, while a pronounced peak in December 2019 was attributed to local residential heating, which was amplified by winter conditions and polar vortex dynamics.

Published as:

PULIMENO S., Bruschi F., Feltracco M., Mazzola M., Gilardoni S., Crocchianti S., Cappelletti D., Gambaro A., Barbaro E., 2024, *Investigating the Presence of Biomass Burning Events at Ny-Ålesund: Optical and Chemical Insights from Summer-Fall 2019*, Atm. Env., 320, https://doi.org/10.1016/j.atmosenv.2024.120336.

4.1 Abstract

Summer 2019 is remembered as one of the most intense biomass burning (BB) seasons on record for the Northern Hemisphere. During the MOSAiC expedition, a smoke-dominated layer was identified in the upper troposphere over the North Pole region. The origin of this layer remains unclear, and no evidence has been found to indicate the intrusion of such particles into the Arctic Boundary Layer. The main aim of this work was to evaluate if biomass burning events in the summer 2019 were detectable at Gruvebadet Atmospheric Laboratory, close to Ny-Ålesund (Svalbard Islands) during the second half of 2019. This paper proposes an innovative approach to discriminate biomass burning events based on optical measurements combined with chemical analysis and air mass back-trajectories. Monthly background values of optical coefficients were defined using multi-annual (2018-2021) statistics and twelve possible events were identified. Source apportionment through positive matrix factorization (PMF) identified that the biomass burning factor by PMF accounted for only 2% of the total investigated concentration. The specific biomass burning tracers such as levoglucosan and phenolic compounds were compared with optical measurements and with the PMF results. Air mass trajectory analysis revealed that the early summer fires detected at Ny-Ålesund originated mainly from North America, as also confirmed by the presence of BB factor of PMF, levoglucosan and also vanillic species (softwood combustion tracers). In contrast, the chemical composition and air masses analysis of the highest peak detected in early December suggested residential heating as plausible source, further amplified by the onset of the harsh winter season and the expansion of the polar vortex towards mid-latitudes.

4.2 Introduction

The Arctic is a unique environment that is undergoing enormous changes due to a rapid warming in the region (Boyer et al. 2022). It is clear from paleoclimate records and climate model projections that this region is under enormous stress, which is carrying to an increase of warm waters entrance from the Atlantic into the Arctic Ocean, northward advance of the treeline, permafrost thawing and modification to the global atmospheric circulation (Serreze and Barry 2011). In this fast-changing region, drier conditions and a general increase in mean and maximum air temperatures contribute to increased wildfire activity (Box et al. 2019), especially in Central Siberia, Northern America, and Canadian boreal forests (Kharuk and Ponomarev 2017; Veraverbeke et al. 2017; Kasischke and Turetsky 2006). What scientists typically considered 'fire-resistant' ecosystems (peatlands, tundra bogs) are now frequently hit by wildfires (McCarty et al. 2020). These are carbon-rich soils formed over thousands of years and represent the most carbon-dense ecosystems on our planet - e.g., a northern bog can contain up to ten times as much carbon as a boreal forest (Witze 2020). Fires cause extensive air pollution by emitting large amounts of primary atmospheric aerosols (mostly black carbon - BC and brown carbon - BrC) and other gaseous species. Secondary aerosols are also formed in the atmosphere by chemical reactions involving sulfur dioxide, nitrogen oxides, and other chemical species (Tomasi et al. 2017). Primary and secondary aerosol particles interact with shortwave solar radiation differently depending on their size and chemical composition (Iqbal 1983). Through the absorption and scattering of solar radiation, biomass burning (BB) aerosols can alter the surface energy budget, act as cloud condensation nuclei, and change the cloud albedo (Tomasi et al. 2017). Aerosol optical and chemical properties can strongly fluctuate seasonally

as meteorological conditions and sources (natural or anthropogenic, from inside or outside the Arctic region) change in time (Quinn et al. 2008). Shaw 1995 described the Arctic haze phenomenon, defining it as an inflow of polluted air from middle latitudes or an uplift outside the Arctic dominated by accumulation mode aerosols (size between 0.5-2 μm) during winter and spring. Contrariwise, the Arctic troposphere is relatively isolated during the summertime because of the absence of diabatic-surface cooling and the disappearance of high continental pressure (Shaw 1995; Stohl 2006). Thus, since the interactions of aerosols with solar radiation are at their maximum during summer, the concentration of light-absorbing aerosol can be very problematic, having the potential to act as a positive feedback mechanism to the Arctic amplification phenomenon (Gillett et al. 2004). The Arctic region is experiencing an increase in biomass burning events, which result in the release of aerosols into the atmosphere with significant impacts on the environment (Stockwell et al. 2015).

Summer 2019 was remembered as one of the most intense burning seasons on record for the northern hemisphere, especially because of the spread of wildfires in Yacutia (Siberia) with an unprecedented magnitude and size, and a total burned area of three million hectares (Voronova et al. 2020). In September 2019, the MOSAiC Expedition started with the German research icebreaker Polarstern drifted through the Arctic Ocean for a year. Throughout the campaign, researchers detected a persistent layer of aged wildfire smoke in the upper troposphere and lower stratosphere (UTLS) (Ohneiser et al. 2021). Furthermore, Lidar observations conducted at Ny-Ålesund revealed an increase in the stratospheric aerosol optical depth (AOD) during the summer period of 2019 (Engelmann et al. 2021). Ohneiser et al. 2021 emphasized that the question of whether the fires in central and eastern Siberia were the source of the smoke observed in the UTLS over the North Pole region during the MOSAiC expedition still remains unanswered. Engelmann et al. 2021 speculated that the smoke was lifted by the so-called self-lifting process to the UTLS. Then smoke particles became quickly distributed over large parts of the Northern Hemisphere within a few weeks.

This paper aims to investigate if the biomass burning occurred in summer 2019 was detectable at Ny-Ålesund (Svalbard) within the Arctic Boundary Layer. Aerosol sampling and measurements were performed at Gruvebadet Atmospheric Laboratory (GAL), close to the research village of Ny-Ålesund, from mid-June to December 2019, coinciding with MOSAiC's report on the presence of a thick 10 km layer of wildfire smoke. In this paper, we present an innovative multidisciplinary approach that combines aerosol optical properties with chemical characterization and source apportionment analysis throughout the entire period to identify events attributable to wildfires. Furthermore, we performed high-resolution back-trajectory analysis to determine the origins of air masses reaching Svalbard lower troposphere.

4.3 Materials and Methods

4.3.1 Area of Investigation

Observations of the atmospheric composition, with a particular focus on aerosols, were carried out at the Ny-Ålesund Research Station, on the Spitsbergen Island of Svalbard. The station is placed on the southern shore of Kongsfjorden, and the aerosol in situ measurements, for both optics and chemistry, were made at the Gruvebadet Atmospheric Laboratory (GAL, 78.91° N, 11.89° E; 61 m a.s.l., see Figure 4.1) located

FIGURE 4.1: View of Oscar II Land with the village of Ny-Ålesund on the southern shore of Kongsfjorden. The Gruvebadet Atmospheric Laboratory is marked with a red dot. Retrieved from TopoSvalbard (https://toposvalbard.npolar.no/; accessed May 2023)

about 1 km south from the settlement. The location of GAL ensures minimal anthropogenic influence of the village thanks to the dominant wind's regime, oriented along the north-west/south-east direction (Mazzola et al. 2016).

4.3.2 Aerosol Optical Characterization

Aerosol optical properties have been measured at GAL using a combination of different instruments since 2010. For our purposes, we used measurements collected from January 2018 to December 2021 to describe the average seasonal changes and discuss the variability during the investigated period (second half of 2019). During the period 2018-2021 measurements were continuous along the year and representative of both the cold and the warm seasons. A Radiance Research's M903 nephelometer was used to measure the light scattering extinction coefficient (b_s) at 530 nm, while the Particle Soot Absorption Photometer (PSAP), also by Radiance Research, retrieved the amount of light absorbed by the collected particles (b_a) at three wavelengths (467, 530, and 660 nm). The nephelometer and PSAP measurements were averaged hourly and corrected following Virkkula 2010. The meld between b_s and b_a at 530 nm allowed the evaluation of Single Scattering Albedo (SSA) at the same wavelength, which gives information about scattering efficiency with respect to total extinction efficiency. In this study it was derived as follows:

$$SSA = \frac{b_s}{b_s + b_a} = \frac{b_s}{b_{ext}} = 1 - \frac{b_a}{b_{ext}} \tag{4.1}$$

where the b_s is the scattering coefficient, b_a the absorption coefficient, both at 530 nm, and b_{ext} the extinction coefficient given by the sum of scattering and absorption. Furthermore, the b_a at 467 and 660 nm were used to calculate the Absorption Ångström Exponent (AAE) that, such as SSA, is an intensive property of particles which describes the wavelength dependence in aerosol absorption and it is defined as:

$$b_{a(\lambda)} = b_0 \lambda^{-AAE} \tag{4.2}$$

where $b_{a(\lambda)}$ is the aerosol absorption coefficient, λ represents the wavelength, and b_0 a wavelength independent constant equal to the absorption coefficient at λ=1 μm. AAE usually decreases exponentially with λ over the visible and near-infrared spectrum bands (Ångström 1929). In this manuscript, the Ångström parameter was retrieved as the slope passing through two points. Specifically, it was defined as:

$$AAE = \frac{-log(b_a(467)/b_a(660))}{log(467/660)} \tag{4.3}$$

where $b_a(467)$ and $b_a(660)$ are the absorption coefficients at wavelength 467 and 660 nm respectively.

Meteorological data were acquired from the Amundsen-Nobile Climate Change Tower (CCT), located about 2 km NW from Ny-Ålesund. The CCT provides continuous profile of meteorological parameters at four levels up to 34 m and, in this paper, data averaged every 30 minutes at a height of 5 m were used for temperature, relative humidity, wind speed, and wind direction (Mazzola et al. 2016).

For December 2019 only, we present corrected Level 1 Aerosol Optical Depth (AOD) data from AErosol RObotic NETwork (AERONET). At Ny-Ålesund, University of Valladolid and AWIPEV manage a solar-sky-moon CIMEL-318T photometer for the retrieval of AOD at 6 different wavelengths (440, 500, 675, 870, 1020, and 1640 nm) (Sinyuk et al. 2020). Moon-photometers enable the measurements of lunar irradiance and the derivation of AOD and other products also during night-time (Román et al. 2020; González et al. 2020). AOD is a measure of the amount of light scattering and absorption by aerosol particles along the path of the light beam. Because of the Arctic haze phenomenon, AOD in the Arctic is noticeably higher during winter and spring rather than in summer (Tomasi et al. 2015). Because level 1 lunar-AOD data exhibited disturbance due to the presence of clouds, we applied a correction procedure (more information will be provided in Supplementary material)

4.3.3 Aerosol Sampling and Chemical Characterization

Twenty-seven aerosol samples were collected from 16th June 2019 to 2nd January 2020 at the GAL. A multi-stage Andersen impactor (TE-6000 series, Tisch Environmental Inc.) was used to collect aerosol samples on six pre-combusted (4 hours at 400 °C in a muffle furnace) quartz fiber filters. The sampler accumulates particles with cut-off diameters of 10 μm, 7.2 μm, 3.0 μm, 1.5 μm, and 0.95 μm on slotted filters and $<$ 0.49 μm on the backup filters. The frequency of sampling varied from 6 to 10 days, for a total air volume of 9000 to 15000 m^3 per sample. Field blanks were obtained using the same filters installed on the sampler with the air pump switched off. Both samples and blanks were wrapped in a double layer of aluminium foil and stored at -20 °C until analysis.

Half of the filter was broken into small pieces and placed in a 50-mL polyethylene vial (previously cleaned with ultrapure water into ultrasonic batch for 30 min) with steel tweezers. The sample was spiked with 50 ng of ^{13}C-labelled internal standard mix of amino acids, $^{13}C_1$-vanillic acid and $^{13}C_6$-vanillin and 100 ng of $^{13}C_6$-glucose and $^{13}C_6$-levoglucosan. Extraction was carried out in an ultrasonic bath for 30 min with 15 mL and 30 mL of ultrapure water for slotted and back-up filters, respectively. The extract solution was filtered through a 0.45 μm PTFE filter to remove particles and quartz fiber traces before instrumental analysis. Previously validated methods were applied to the aerosol samples to determine inorganic ions and organic acids (methanesulfonic acid and C2-C7 carboxylic acids) (Barbaro et al. 2017; Feltracco et al. 2021), monosaccharides, alcohol-sugars, levoglucosan and its isomers, sucrose (Barbaro et al. 2015a), free amino acids (Barbaro et al. 2015b), phenolic compounds (Zangrando et al. 2016), and photo-oxidation products of α-pinene (Feltracco et al. 2018).

4.3.4 Source Apportionment using Positive Matrix Factorization

Positive Matrix Factorization (PMF) method (Paatero and Tapper 1994) was used to identify the number of factors/sources and their chemical profiles. The model uses data for all concentration and uncertainty values for j species and i days. Data confidence can be maintained by adjusting the uncertainties by real observations. For the current analysis, the U.S. EPA version of PMF was used (EPA PMF 5.0), which is based on the multilinear engine ME-2. In this study, the input dataset was created by compiling the concentrations of the detected chemical species (variables, n = 27) for each stage of the impactor (6 different sizes) across 27 samples, resulting in a total of m = 6 x 27 = 162 cases. This approach enables the allocation of different stages for assessing the temporal evolution of the samples while considering particle size distribution. The uncertainties in sample concentrations were assessed by considering the relative standard deviation of each variable obtained during the validation procedure. For the PMF application, an additional 10% uncertainty was incorporated for all species. Uncertainties in the PMF results were determined using the bootstrap method. The optimal number of factors was determined by analyzing the parameters IM (maximum individual column mean) and IS (maximum individual column standard deviation) derived from the scaled residual matrix, along with Q-values (goodness-of-fit parameters). Specifically, for Q-values, the optimal solution was identified at the point where the curve's slope exhibited a significant change. Conversely, for the IM and IS parameters, as the number of factors increased to a critical value, these parameters experienced a sharp decline. In this work, the values of Q, IM, and IS indicated a reasonable solution corresponding to 5 factors.

4.3.5 Satellite data and Back-Trajectory analysis

Satellite-derived fire data were obtained from the Fire Information for Resource Management System (FIRMS) active fire detection product of the Moderate Resolution Imaging Spectroradiometer (MODIS) instrument onboard the Terra and Aqua satellites. The data were obtained from the online platform FIRMS (https://firms.modaps.eosdis.nasa.gov; accessed March 2023) and cover the whole period from June to December 2019. Satellites capture a snapshot of Earth's surface as they orbit. These images contain hotspots that correspond to the center of pixels of approximately 1 km, flagged as containing thermal anomalies. To measure the brightness temperature of a hotspot, which is a measurements for the photons received by the spacecraft at a specific wavelength, FIRMS uses the MODIS channels 21/22 and 31. In this work we utilized the Fire Radiative Power (FRP) parameter from the MODIS data to create maps of active fires for each identified BB event. The FRP (W) represents the rate of radiant energy released by a fire, and is a useful parameter to estimate the fire intensity and burned area. By using the FRP data, we were able to accurately locate and visualize the active fire spots.

To identify possible sources of BB particles reaching the sampling site, we used the HYSPLIT model developed by the National Oceanic and Atmospheric Administration (NOAA) Air Resource Laboratory. HYSPLIT is a widely used tool for air mass trajectory analysis that can be used to simulate the trajectory of air masses based on meteorological data from the Global Data Assimilation System (GDAS). Using HYSPLIT, and in particular Global Forecast System (GFS) data at 0.25 degrees, we generated 240-hour back-trajectory frequency plots for air masses arriving at Ny-Ålesund, with a time step of 1 hour (24 trajectories per day). The starting height of the trajectories was set at 50 m above ground level. The back-trajectory frequency

plots show the parts of back-trajectories below the mixing height for different receptor locations. The plots were generated by dividing the region of interest into a grid of cells and counting the number of back-trajectories endpoints within the boundary layer in each cell. The frequency provided information about the potential areas of origin of the aerosol burning particles during extreme events. Overall, HYSPLIT back-trajectory analysis provided valuable insights into the transport patterns of aerosol burning particles during extreme events and helped us to identify the possible areas of origin of these particles.

4.3.6 NAAPS transport model

To identify the origin of BB smoke and assess the concentration of aerosols at Ny-Ålesund, the Navy Aerosol Analysis and Prediction System - Reanalysis (NAAPS-RA) has been employed. NAAPS is the US Navy's chemical transport model, operating at a spatial resolution of 1 x 1° with data updated every 6 hours, providing information on aerosol optical depth at 550 nm. This information is primarily based on the Danish Eulerian Hemispheric Model (Witek et al. 2007). The NAAPS model has the capability to characterize various types of aerosols, including biogenic and anthropogenic particles, sea salt, dust, and BB smoke. Specifically, in the case of BB smoke, it relies on near-real-time satellite-based thermal anomaly data to construct smoke source functions. In NAAPS reanalysis, additional orbital corrections for MODIS-based emissions are applied, and a two-day maximum approach (considering signals from the previous day and the present day) is utilized to minimize orbital effects (Lynch et al. 2016). This approach enables the accurate identification of the sources of BB smoke and the assessment of aerosol concentration in Ny-Ålesund, contributing to a better understanding of aerosol transport and its impact on the region. To gain a more in-depth knowledge of the aerosol plume's dynamics, please refer to the NAAPS animation provided at this link: https://youtu.be/5lXQU9HzSBU.

4.4 Results

The results section of this study provides a detailed analysis about the optical and chemical properties of aerosols detected at Ny-Ålesund during the latter half of 2019. Our findings present insights into the main characteristics, source areas, and transport of these events on the local and regional atmosphere. Through the use of aerosol characterization techniques, we have identified the optical properties and chemical composition of these aerosols, allowing for a better event detection.

4.4.1 Optical Properties and Events Detection

Identifying biomass burning events from aerosol optical properties remains a challenge, particularly in the Arctic, where other sources of aerosols, long-range transport, and particle aging processes can further complicate the analysis (Kyrö et al. 2013). While a well-defined procedure for such identification is not available, previous studies have attempted to identify wildfires using various aerosol optical parameters (Markowicz et al. 2016; Stohl et al. 2013; Dall'Osto et al. 2019; Zielinski et al. 2020). These studies typically rely on ground-based measurements and air mass trajectory analysis to confirm the source of aerosol particles. Scattering and absorption coefficients at 530 nm, from January 2018 to December 2021, are shown in Figure S1. During the winter-spring months, frequent episodes of high scattering and absorption values were

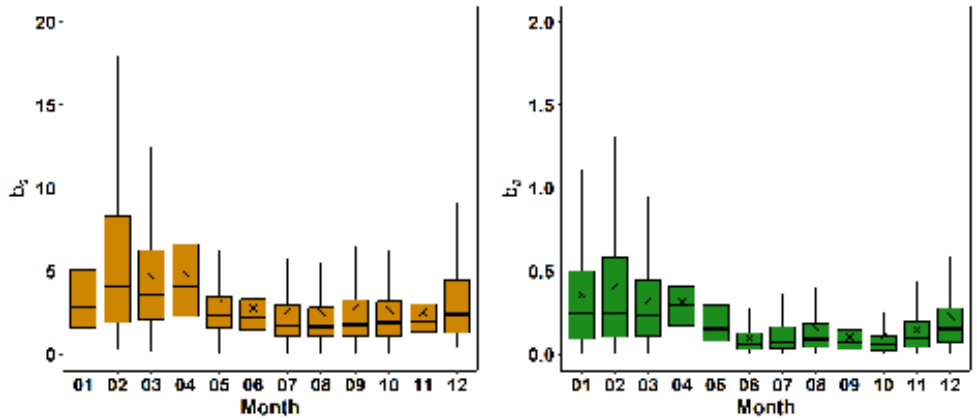

FIGURE 4.2: Monthly box-and-whisker plots of b_s and $b_a(530)$ obtained from hourly data over the period 2018 – 2021 at Ny-Ålesund. Each plot shows the 5, 25, 50 (median), 75, and 95th percentiles, as well as the mean value (cross) for each month.

observed at Ny-Ålesund, with maximum values of almost 48 Mm^{-1} and 5 Mm^{-1}, respectively, with events lasting from a few hours to few days. In line with previous studies, the mean (and median) value of b_s and $b_a(530)$ were found to be 3.63 (2.40) Mm^{-1} and 0.22 (0.13) Mm^{-1}, respectively. Specifically, Schmeisser et al. 2018 reported similar annual statistical values of 4.35 (2.82) Mm^{-1} and 0.18 (0.09) Mm^{-1} for scattering and absorption coefficients at the same location for years 2012-2014.

We obtained multi-annual monthly means of b_s and b_a from this 4-years time-series, which are presented in Figure 4.2. There is a clear seasonality for both parameters, consistent with findings from other studies (Pandolfi et al. 2018; Schmeisser et al. 2018). Specifically, aerosol scattering and absorption exhibit a significant peak during late winter-spring, which coincides with the Arctic haze phenomenon, due to the effective transport from the lower latitudes (Gilardoni et al. 2023). The monthly averages of b_s between February and April ranged from 4.74 to 6.04 Mm^{-1}, representing the highest values observed. Conversely, the summer months exhibited minimum values of approximately 2.44-2.57 Mm^{-1} for this parameter. Similarly, $b_a(530)$ displayed the highest values during late-winter and early-fall months, ranging from 0.32 to 0.40 Mm^{-1}, while the summer months exhibited the minimum values in the range of 0.09-0.15 Mm^{-1}. Throughout our study, we found that a log-normal frequency distribution accurately fits the data for both coefficients. Interestingly, the mean values were consistently higher than the median for all months. As a way to establish a baseline for our analysis, the multi-annual monthly statistics were evaluated (thus including the 5th, 25th, 50th, 75th, 95th percentile, and mean) in order to identify the most appropriate monthly background values for each coefficient (Figure 4.2). Table 4.1 shows the statistical values for the months of June-December, as they were used to assess the anomalies for the same period of 2019. Selecting a background value is crucial to accurately assess the contribution of BB events to the observed aerosol properties. In this work, the 50th percentile has been used as the background value for b_a during the identification of events, since it helps to minimize the influence of extreme values and outliers.

We focused on events that exceeded the 50th percentile of the reference month for at least 16 hours per day and for a minimum of three consecutive days. This criterion has been adopted to differentiate extreme wildfire events from short-term

Month	25th	Mean	50th	75th
June	0.03	0.11	0.06	0.14
July	0.03	0.14	0.08	0.17
August	0.04	0.16	0.10	0.21
September	0.02	0.09	0.06	0.13
October	0.02	0.07	0.04	0.09
November	0.04	0.14	0.10	0.19
December	0.07	0.23	0.15	0.28

TABLE 4.1: Means of $b_a(530)$ at Ny-Ålesund, including 25th, 50th, and 75th percentile calculated for each month from June to December based on 4-years of data (2018-2021).

absorption spikes that may originate from local sources or transient events. By using this criterion, identify 12 long-lasting BB events and ensure that they were not merely artifacts caused by short-term variability in the measurements (Table S1).

4.4.2 Aerosol chemical composition and PMF analysis

Biomass burning tracers, such as levoglucosan, its isomers and phenolic compounds were determined in the aerosol samples collected at GAL from mid-June to the end of December 2019 with low temporal resolution (6-10 days) compared to optical measurements (1 hour). Moreover, other chemical tracers (inorganic ions, organic acids, free amino acids and sugars) were investigated to perform a complete characterization of aerosol and to identify their sources.

The most abundant species (Table S2) were sulphate (40%), chloride (23%) and sodium (21%), while ammonium (4%), magnesium (3%), calcium (3%) and nitrate (3%) were below 5%. All other investigated species are below 1%. Sodium, chloride, and magnesium are the main components of the sea spray source (Giardi et al. 2016), whereas non-sea salt fraction of Ca^{2+} and SO_4^{2-} represented 72% and 86%, respectively. The contributions of the non-sea-salt fraction of Ca^{2+} and SO_4^{2-} were calculated for the difference between their concentrations and the sea salt values obtained using the Ca^{2+}/Na^{+} ratio in seawater (0.038 w/w) and the SO_4^{2-}/Na^{+} ratio (0.252 w/w). The particle size distribution of major ions (Figure S3a) confirmed the local sources of sea salt components because Na^{+}, Cl^{-} and Mg^{2+} were mainly distributed in the coarse mode. The most abundant species was sulphate and several sources can emit this ion. The sea-salt sulphate ($ss - SO_4^{2-}$) contributed minimally (14±7%) to the sulphate budget and exhibited an increase during the winter period, whereas the main sources were attributed to anthropogenic sources due to the atmospheric oxidation of SO_2 (Udisti et al. 2016). In fact, we evaluated also crustal components and the sulphate contribution from marine phytoplanktonic activity as suggested by Udisti et al. 2016 but these contributions are lower considering the total non-sea-salt sulphate (Figure S3b). The phytoplanktonic contribution has an increase during the summer period linked to the algal bloom (Becagli et al. 2019).

The total median concentration of carboxylic acids is 4 ng m^{-3} and C_2-oxalic acid (48%) and acetic acid (21%) are the most abundant carboxylic acids. The sugars composition is dominated by levoglucosan (32% of the total median concentration of sugars), glucose (19%), mannitol (16%) and arabitol (11%), two tracers of fungal spores. The median concentration of L-free amino acids is 202 ng m^{-3}, with L-arginine

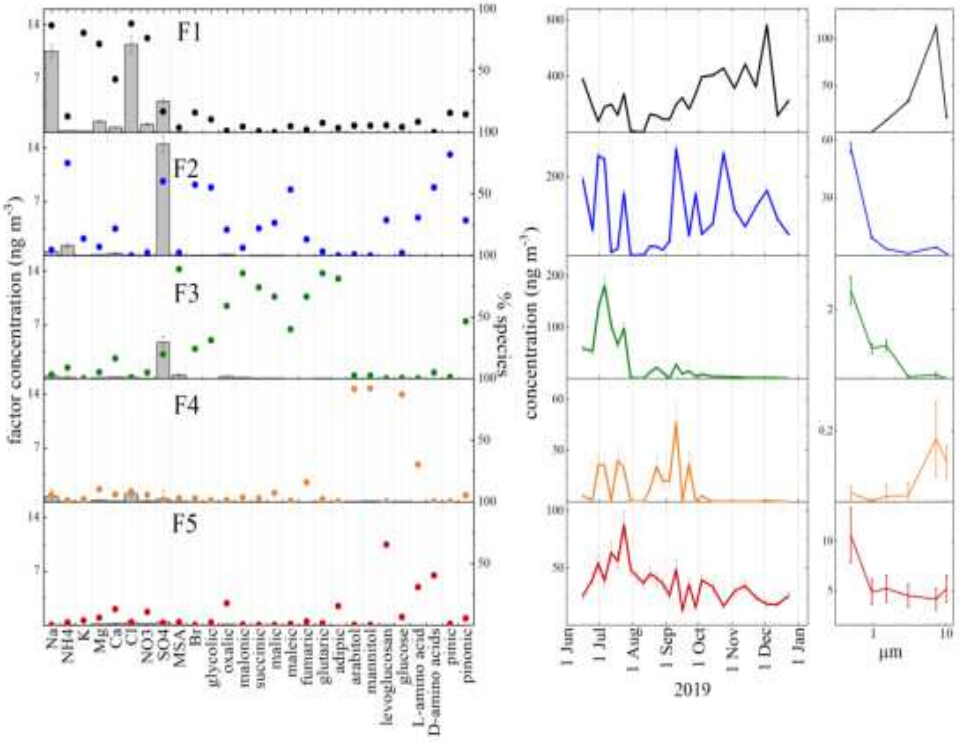

FIGURE 4.3: Results of Positive Matrix Factorization (PMF); A) source profiles where bars identify the species in ng m^{-3} that mainly characterize each factor (F1 - sea salt input; F2 - sulphate component and long range compounds; F3 - secondary products; F4 - fungal spores; F5 - biomass burning) profile while the points describe the percent of species; B) factor contributions during the sampling period; C) particle size distribution of each factor.

(36%) of the total median concentration of 20 ng m^{-3} with the only presence of D-alanine and D-aspartic acid. Finally, the main components of organic acids are the phenolic compounds with vanillin moieties, the main products of the combination of softwood, and two photo-oxidation products of α-pinene (cis-pinonic and pinic acids).

The comparison of aerosol concentrations reconstructed by the PMF and those measured showed that the PMF can reconstruct the data with a slope of 0.99 and an R^2 of 0.91. The profile of each factor, in terms of concentrations (bars) and in terms of percent of species (black points), the temporal trend and the particle size distribution of each factor are shown in Figure 4.3.

The first factor (F1) describes 51% of the total investigated concentration, and it is mainly characterized by saline ions. Na^+ and Cl^-, that are recognized as specific tracers of sea salt aerosol (O'Dowd et al. 1997), suggest that this factor represents the sea spray component. Moreover, the particle size distribution (Figure 4.3C) defines that this first factor is mainly distributed on the coarse mode, confirming a local marine source of this type of aerosols. The general trend of sea salt factor (Figure 4.3B) shows an increase starting in autumn due to more frequent cyclonic system. Sea salt emissions from sea-ice due to blowing snow reach their maximum in December (Huang and Jaeglé 2017).

The second factor (F2), loaded for 30% of the total investigated concentration,

is called "sulfate and long range compounds" because sulphate is the most abundant species but other organic compounds with long range transport sources are well represented in this factor. For example, photo-oxidation products of α-pinene (cis-pinonic and pinic acids), glycolic and maleic acids and also levoglucosan are included in this factor (Figure 4.3A). It consists mainly of fine aerosols and does not show a seasonal trend in the considered period.

The third factor (F3) describes the 12% of the total concentration estimated by PMF, and it loads with methanesulfonic acid (MSA), carboxylic acids and pinonic acid (Figure 4.3A). These species are the secondary photo oxidation products, mainly distributed on the fine particles (Figure 4.3C). Moreover, the Figure 4.3B well shows that these species have higher concentration until the end of July, which then drops dramatically.

The fourth factor (F4), loaded for 5%, is characterized by arabitol and mannitol, with also glucose and L-free amino acids. This factor represents the biogenic emission from fungal spores, occurred during the summer period (Figure 4.3B) and it is mainly distributed on the coarse fraction (Figure 4.3C).

Finally, the last factor (F5) represents the "biomass burning contribution" because levoglucosan characterizes it, with also a contribution of L- and D-free amino acids and oxalic acid. This factor is mainly distributed on the fine particles suggesting a source of atmospheric long-range transport. For the aim of this work this is the most important factor, but it loads only for 2% of the total investigated concentration.

4.5 Discussion

Figure 4.4 shows in situ surface optical observations for the period June - December 2019, plotted as daily averages. Despite some data gaps, our analysis reveals variable values of b_s and b_a, at all wavelengths, throughout most of the season.These values contrast with the relatively stable b_s and b_a coefficients observed during September and October 2019, which are consistent with values reported by other authors (Zielinski et al. 2020). Specifically, b_s was found to be around 2 Mm^{-1}, while b_a was lower than 0.07 Mm^{-1}. In Figure 4.4, it can be observed that between June and September, AAE values typically fell within the range of 1 to 2, displaying relatively limited variation. During this period, there was also a decrease in the SSA value. In contrast, in the months from October to December, higher and more widely dispersed AAE values were observed, while the SSA value remained relatively stable at around 1.

After comparing such observations with multi-annual monthly means values determined through the procedure described in section 4.4.1, twelve events were detected by the analysis of aerosol optical parameters (Table S1).

A careful analysis revealed that from the middle of June, when also chemical analysis was performed, only narrow peaks of b_a were detected until the end of July. However, data were missing for about two weeks from the end of June to the beginning of July. Despite the missing data, Figure S2 shows that $b_a(530)$ levels exceeded the monthly background value of June and July (0.03 Mm^{-1}, see Table 4.1) for two periods, June 19-22 and July 29-30, with peaks reaching about 0.6 Mm^{-1} and 0.5 Mm^{-1}, respectively. Based on the back-trajectory frequency plots (Figure S4), the first episode is plausibly linked to the mid-June fires that occurred in the Canadian provinces of Alberta and Saskatchewan as well as in the northeastern regions of the United States. Considering the chemical analysis of wildfire tracers, aerosol seems not affected by BB events during June, probably due to the intensity of fires or weak transport processes.

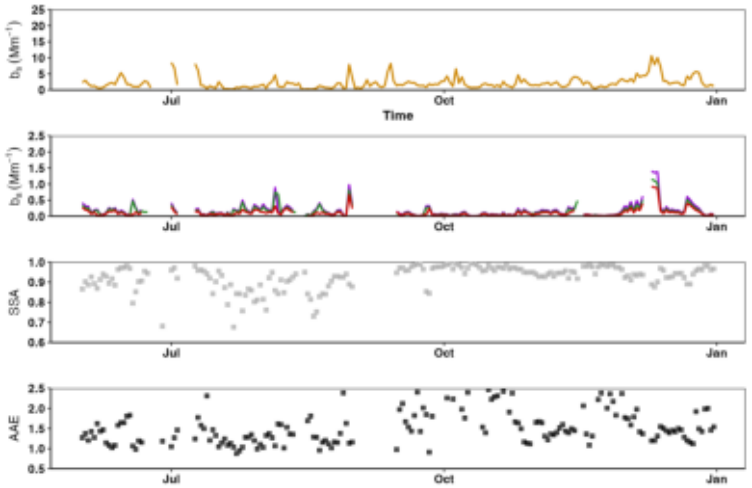

FIGURE 4.4: Daily aerosol optical parameters taken between June and December 2019. The upper panel shows scattering coefficient, while the middle panel displays absorption coefficients (467 nm in violet, 530 nm in green, and 660 nm in red). The bottom panel represents the AAE (black) and the SSA (gray), retrieved with b_a values higher than 0.07 Mm^{-1}.

For the late July event the air masses appear to have originated from both Canada and Alaska. From the end of July to the beginning of August, the wildfire afflicted mainly the North America and Siberia. The back-trajectories analysis showed that air masses weakly come from North America and then remain steady over the Svalbard archipelago. According to the wind direction analysis conducted using data from CCT (not shown), during this period a significant portion of air masses sampled at GAL was found to come from the E and NE (town centre). This suggests that the pollution event observed in early August may be attributed to a local source of pollution. However, Figure 4.5 reports a value of almost 50 ng m^{-3} for factor 5 by PMF, and spikes in the levoglucosan trend (almost 0.25 ng m^{-3}), vanillin (VAH, 0.05 ng m^{-3}), vanillic acid and acetovanillone (VA and VAC respectively, approximately 0.003 ng m^{-3}). The presence of such wildfire tracers, which are specific markers of conifer fires, seems to point out a long-range transport rather than a local influence despite the air masses being stable over the Svalbard archipelago. Furthermore, LIDAR measurements at Ny-Ålesund indicate a strong increase in the upper troposphere and lower stratosphere AOD in August 2019, suggesting the occurrence of long-range transport processes. Ohneiser et al., 2021.

Whereas the evaluation of events in the summer period was quite straightforward, during autumn the constrains of our approach seem to minimize some episodes. In particular, throughout the period August - December 2019, discernible spikes were observed that could potentially suggest the occurrence of biomass burning events. Nonetheless, the established criteria (exceeding the 50th percentile for at least 12h) for identifying events were not satisfied by these observations and consequently, these spikes were not included in our analysis. The majority of the events identified using our approach mainly occurred during the fall and early-winter months. During the late summer - early fall, aerosol scavenging along the pathways from lower latitudes to the Arctic decreases compared to previous months, leading to a more efficient transport of polluted air masses and the consequent increase in aerosol scattering and absorption coefficients (Gilardoni et al. 2023; Garrett et al. 2011). This may account

for the high number of events identified between September and December 2019 in our study. Moreover, Figure S4 shows an evident change of atmospheric transport regime, mainly from North America during the summer period to North Europe and Russia during autumn and early-winter.

In general, the increase in the aerosol absorption coefficient was not accompanied by a proportional increase in the scattering coefficient. This behavior indicates a shift towards a higher fraction of absorbing particles, likely caused by the presence of BB aerosols in the atmosphere. Accordingly, the SSA exhibited a decrease, with values dropping below 0.90 from an average background value of 0.95. In agreement with prior studies, there is a strong correlation between BB emissions and an increase in the aerosol absorbing coefficient at all wavelengths (Eck et al. 2003; Markowicz et al. 2016; Zielinski et al. 2020). The AAE values during the duration of the events are also consistent with the expected values of a burning event, with values tending to lay between 1 and 1.5. (Markowicz et al. 2016). For most of the events identified, the analysis of the aerosol optical properties alone appears to trace them back to the presence of particles attributable to fires, even if additional chemical information is needed to confirm this source.

In general, the mode of representing back trajectories based on frequencies (Figure S4) makes the main sources more legible when dealing with a large number of trajectories, as in our case. However, this type of graph emphasizes converging areas because, unless there is a prevailing current throughout the period, it is evident that as one moves away from the arrival point, the paths diverge. This implies that the frequency density decreases as one moves away from the source region, which is why a logarithmic scale was used. It is also the reason why the highest values are generally observed at the receptor site, which is furthermore always within the Planetary Boundary Layer (PBL). This discussion suggests that there might have been regions through which only a few trajectories passed, but they could have been significant in terms of collected material. However, such regions were not revealed by the frequency graph, and this could have been particularly true for the events that occurred on 19-22 June, 29-30 July, and 09-10 August. An animation has been created by merging daily NAAPS-RA smoke AOD distribution plots to illustrate the smoke transport path from June to December 2019 (https://youtu.be/5lXQU9HzSBU). The NAAPS-RA data reveal a noteworthy increase in AOD in the Arctic, spanning from mid-June to early September. Fires originating in Siberia, Canada, and Alaska were identified as the sources responsible for the transported BB smoke, as measured at Ny-Ålesund, specifically on July 29-30 and during all the episodes recorded in August. Since the beginning of September no discernible active hot spots have been recorded. The PMF analysis was performed including major ions, MSA, carboxylic acids, levoglucosan, arabitol and mannitol, glucose, L- and D-amino acids and pinic and pinoic acids. Na^+, Cl^-, and Mg^{2+} are originated by sea spray; conversely, Ca^{2+}, K^+, and SO_4^{2-} have relevant contributions from other sources, especially crustal aerosol and anthropogenic/biogenic emissions (Amore et al. 2022). MSA is originated by the atmospheric oxidation of dimethyl sulphide (DMS), emitted by phytoplankton (Udisti et al. 2016), while carboxilic acids are considered secondary organic aerosol (SOA) and they can have several sources, as recently demonstrated by Feltracco et al. 2021. A limited number of sugars are included in the PMF analysis to reduce the noise during the modelling: arabitol and mannitol were selected as fungal spore's tracers, glucose is a biogenic compound but it is not specific as tracer, while as already pointed out levoglucosan is the key indicator for biomass burning emissions. The source apportionment approach gave a reasonable solution with five factors.

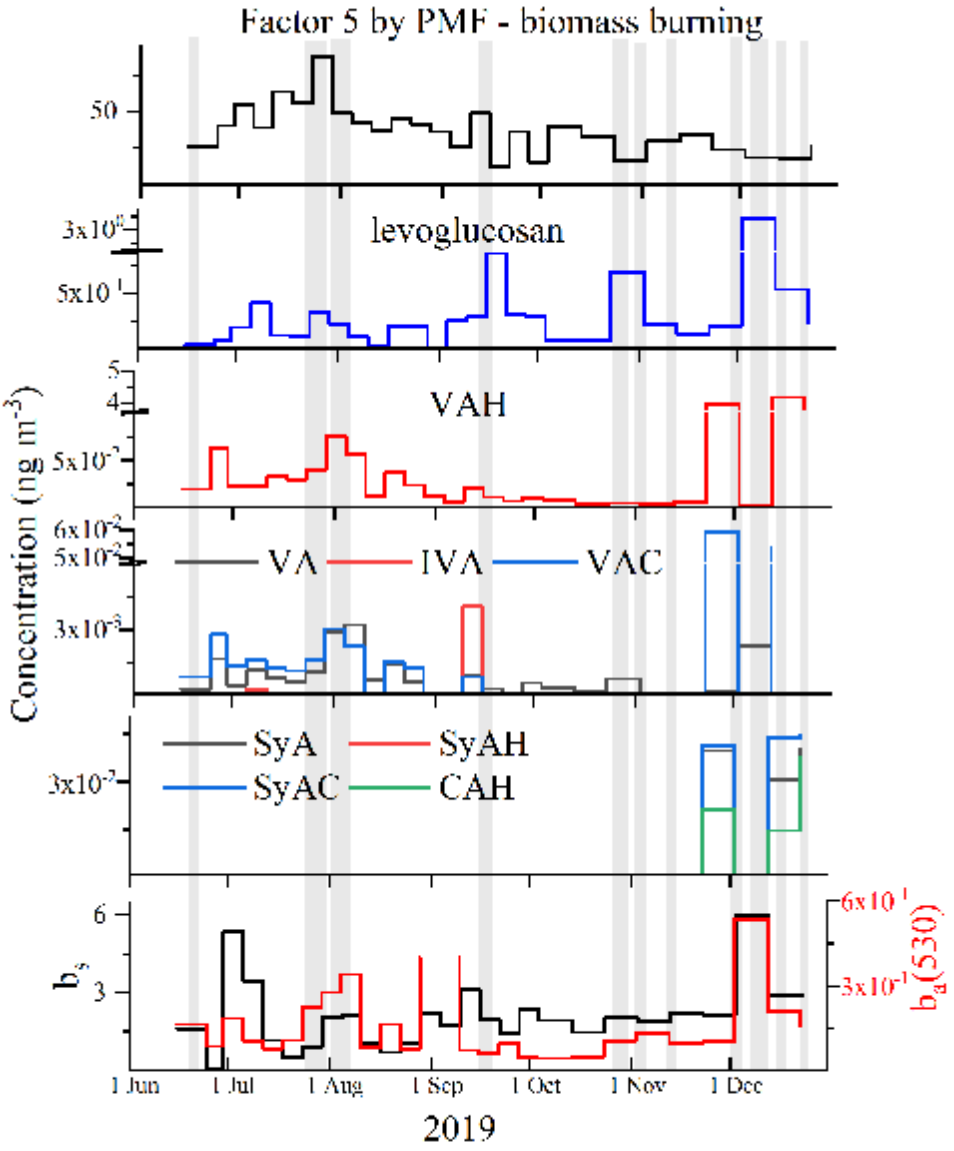

FIGURE 4.5: Trends of factor 5 by PMF, levoglucosan, phenolic compounds in PM_{10} samples, and scattering and absorption coefficient at 530nm (Mm^{-1}) collected at GAL from June to December 2019. The shaded vertical stripes refer to the event reported in Table S1.

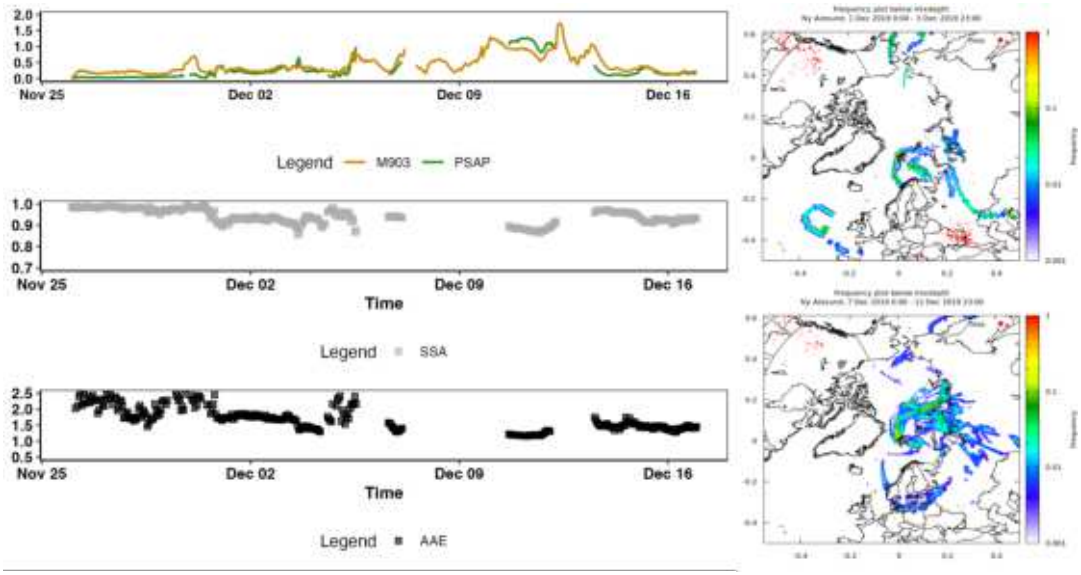

FIGURE 4.6: Hourly aerosol parameters for the early December events; b_s acquired from nephelometer M903, and $b_a(530)$ from PSAP are shown in the upper left panel, while SSA and AAE are shown in the lower left panel. The upper right and lower right panels illustrate the back-trajectory frequency plots below the mixing height for the first and second early December events, respectively.

Figure 4.5 shows the comparison between aerosol optical properties and chemical analysis. In particular, the fifth factor of PMF, attributed to BB contribution, and wildfire tracers, such as levoglucosan and phenolic compounds, are included in the Figure 5. There is a good agreement between optics and chemistry for the events occurred at the end of July and the beginning of August. The elevated values observed in absorption and scattering align well with the peaks in PMF and the chemical analysis of aerosol samples collected at GAL. As depicted in Figure 4.5, PMF factor 5 struggles to fully capture the peak associated with BB in December, primarily due to its low factor loading, which is only 2%. Nonetheless, the events identified in early December were of particular interest owing to their very high measurements in both optical properties and chemical composition, along with the timing of their occurrence. The presence of BB events is substantiated by chemical tracers, with the most prominent peaks observed in levoglucosan (3 ng m^{-3}) and vanillic acid (0.003 ng m^{-3}), both of which are specific markers of combustion.

Figure 4.6 presents a detailed view of the aerosol optical properties for the early December events. With a high temporal resolution of 1 hour, it was possible to identify two different episodes: the first occurring between December 1 and 3, and the second between December 7 and 12. It can be observed that the scattering and absorption coefficients remained relatively stable until the beginning of December (around 2.3 Mm^{-1} for b_s and 0.06 Mm^{-1} for b_a at 530 nm). During both these events, the SSA exhibited a significant decrease dropping to values close to 0.90. On the other hand, AAE provided limited information due to the scarcity of data and the presence of scattered values. Nevertheless, during the two early December episodes, the AAE values appear to be in the range of 1.3 and 1.7, indicating a potential contribution of biomass burning to the aerosol mix. The intensity of these events during December were considered anomalous, and it may suggest a local influence from Ny-Ålesund. However, to verify this hypothesis, we referred to Figure S5 , which includes the AOD

trend measured by the CIMEL photometer installed at the AWIPEV observatory. In Figure S5, it can be observed that data were not available for the first early-December event (December 1 to 3). However, for the second event, an increase in AOD was evident across all wavelengths. The AE values, which ranged between 1 and 1.5, suggest the presence of fine-mode aerosol particles, such as those originating from biomass burning. During both these episodes, the air masses were transported towards Svalbard from Russia, as revealed by the air mass back trajectory analyses. Given the high contribution of other wildfire tracers, such as vanillic compounds, coniferyl aldehyde (CAH), syringic acid (SyA), syringaldehyde (SyAH) and acetosyringone (SyAC) (as shown in Figure 4.5), it is probable that the early December episodes were caused by a mixture of sources. MODIS data-derived images reveal the presence of active fires in southern Russia, Georgia, and Azerbaijan. Nonetheless, the intensity and duration of these fires were inadequate to account for the high values observed in both the physical and chemical properties of the aerosols. Corroborating this, the NAAPS-RA did not highlight any active fires resulting in BB smoke influence during December. Thus, besides biomass fires, we propose an additional contribution from domestic heating. Additional information about the vertical aerosol structure during these events, and a comparison with Zeppelin station (managed by Norwegian Polar Institute and located on the Zeppelin mountain at 472 m a.s.l. at Ny-Ålesund) could provide new insight into this matter.

4.6 Conclusions

Although the MOSAiC campaign provided evidence of a thick aerosol layer in the UTLS with a clear wildfire smoke signature, the hourly mean values of b_s, b_a, SSA, and AAE obtained near the ground-level at GAL from mid-June to the end of December 2019 did not exhibit any notable peak events. The analysis of the measurements highlighted the seasonality of aerosol optical properties, showing that b_s ranges mainly from 0 to 25 Mm^{-1} throughout the investigated period, and $b_a(530)$ values were mainly lower than 0.03 Mm^{-1} in summer (for background) and appreciably higher during the winter-spring period (up to 0.07 Mm^{-1} in December). While the SSA time series is consistent with the trend we expected, with an average of 0.95 that drops and stays around 0.90 with the arrival of highly absorbing particles like BB-ones, the AAE trend is often too scattered to derive useful information, with only some exceptions when it assumes values in line with BB particles between 1 and 1.5. The investigation of aerosol optical properties provided the identification of 12 mild pollution events. The back-trajectory analysis indicated that the air masses predominantly originated from North America between June and August. Subsequently, a change in atmospheric circulation patterns led to a shift in the source area towards the Euro-Asian continent.

Chemical characterization of each event was carried out, together with a positive matrix factorization analysis, allowing for the identification of five different factors. The PMF analysis indicates that sea salt is the major contributor in the coarse fraction of aerosol (51%), while long-range atmospheric transport and anthropogenic sulfate deeply contribute (31%) to the fine mode. Secondary organic aerosols, including MSA and small organic acids, were predominantly observed in the fine particles during the light period. Conversely, another factor identified through PMF analysis exhibited fungal spore markers, with higher concentrations found in the coarse particles during the summer season. During the summer season, the notable presence of biogenic particles, including free amino acids and organic acids, was observed in both the coarse and accumulation modes. Further investigation is warranted to explore the potential role

of these findings in cloud formation. The final factor (F5), representing the contribution of biomass burning, accounted for only 2% of the total investigated concentration. It primarily consisted of specific biomass burning tracers, including levoglucosan, L- and D-free amino acids, and oxalic acid. This factor was predominantly associated with fine particles, indicating long-range transport.

Back-trajectory analysis, combined with MODIS data, revealed a weak correlation between active fires and optical and chemical measurements, implying the presence of highly aged particles (i.e., over 10 days old) over Svalbard from November to December. This finding is consistent with the existence of a layer of aged plume over the North Pole region during the same period as observed during the MOSAiC campaign (Engelmann et al. 2021; Boyer et al. 2022). Moreover, the latest events identified in December may have been influenced by emissions from home heating, given the onset of the winter season and the southward expansion of the polar vortex.

The primary outcome of this paper is the establishment of a multidisciplinary approach that integrates optical and chemical data with back-trajectory analysis. The synergy between optical and chemical measurements can effectively distinguish biomass burning events, even if any alteration in the evaluation criteria will inevitably impact the number of detected events. Therefore, careful consideration must be given to the selection and manipulation of these parameters to ensure accurate identification of wildfires.

Bibliography

Amore, A., Giardi, F., Becagli, S., Caiazzo, L., Mazzola, M., Severi, M., and Traversi, R. (2022). Source apportionment of sulphate in the High Arctic by a 10 yr-long record from Gruvebadet Observatory (Ny-Ålesund, Svalbard Islands). *Atmospheric Environment*, 270:118890. ADS Bibcode: 2022AtmEn.27018890A.

Barbaro, E., Kirchgeorg, T., Zangrando, R., Vecchiato, M., Piazza, R., Barbante, C., and Gambaro, A. (2015a). Sugars in Antarctic aerosol. *Atmospheric Environment*, 118:135–144.

Barbaro, E., Zangrando, R., Padoan, S., Karroca, O., Toscano, G., Cairns, W. R. L., Barbante, C., and Gambaro, A. (2017). Aerosol and snow transfer processes: An investigation on the behavior of water-soluble organic compounds and ionic species. *Chemosphere*, 183:132–138.

Barbaro, E., Zangrando, R., Vecchiato, M., Piazza, R., Cairns, W. R. L., Capodaglio, G., Barbante, C., and Gambaro, A. (2015b). Free amino acids in Antarctic aerosol: potential markers for the evolution and fate of marine aerosol. *Atmospheric Chemistry and Physics*, 15(10):5457–5469. Publisher: Copernicus GmbH.

Becagli, S., Amore, A., Caiazzo, L., Iorio, T. D., Sarra, A. d., Lazzara, L., Marchese, C., Meloni, D., Mori, G., Muscari, G., Nuccio, C., Pace, G., Severi, M., and Traversi, R. (2019). Biogenic Aerosol in the Arctic from Eight Years of MSA Data from Ny Ålesund (Svalbard Islands) and Thule (Greenland). *Atmosphere*, 10(7):349. Number: 7 Publisher: Multidisciplinary Digital Publishing Institute.

Box, J. E., Colgan, W. T., Christensen, T. R., Schmidt, N. M., Lund, M., Parmentier, F.-J. W., Brown, R., Bhatt, U. S., Euskirchen, E. S., Romanovsky, V. E., Walsh, J. E., Overland, J. E., Wang, M., Corell, R. W., Meier, W. N., Wouters, B., Mernild, S., Mård, J., Pawlak, J., and Olsen, M. S. (2019). Key indicators of Arctic climate

change: 1971–2017. *Environmental Research Letters*, 14(4):045010. Publisher: IOP Publishing.

Boyer, M., Aliaga, D., Pernov, J., Angot, H., Quéléver, L., Dada, L., Heutte, B., Dall´osto, M., Beddows, D., Brasseur, Z., Beck, I., Bucci, S., Dütsch, M., Stohl, A., Laurila, T., Asmi, E., Massling, A., Thomas, D., Nøjgaard, J., and Jokinen, T. (2022). A full year of aerosol size distribution data from the central Arctic under an extreme positive Arctic Oscillation: Insights from the MOSAiC expedition. *Atmospheric Chemistry and Physics*.

Dall'Osto, M., Beddows, D. C. S., Tunved, P., Harrison, R. M., Lupi, A., Vitale, V., Becagli, S., Traversi, R., Park, K.-T., Yoon, Y. J., Massling, A., Skov, H., Lange, R., Strom, J., and Krejci, R. (2019). Simultaneous measurements of aerosol size distributions at three sites in the European high Arctic. *Atmospheric Chemistry and Physics*, 19(11):7377–7395. Publisher: Copernicus GmbH.

Eck, T. F., Holben, B. N., Reid, J. S., O'Neill, N. T., Schafer, J. S., Dubovik, O., Smirnov, A., Yamasoe, M. A., and Artaxo, P. (2003). High aerosol optical depth biomass burning events: A comparison of optical properties for different source regions. *Geophysical Research Letters*, 30(20). _eprint: https://onlinelibrary.wiley.com/doi/pdf/10.1029/2003GL017861.

Engelmann, R., Ansmann, A., Ohneiser, K., Griesche, H., Radenz, M., Hofer, J., Althausen, D., Dahlke, S., Maturilli, M., Veselovskii, I., Jimenez, C., Wiesen, R., Baars, H., Bühl, J., Gebauer, H., Haarig, M., Seifert, P., Wandinger, U., and Macke, A. (2021). Wildfire smoke, Arctic haze, and aerosol effects on mixed-phase and cirrus clouds over the North Pole region during MOSAiC: an introduction. *Atmospheric Chemistry and Physics*, 21(17):13397–13423. Publisher: Copernicus GmbH.

Feltracco, M., Barbaro, E., Contini, D., Zangrando, R., Toscano, G., Battistel, D., Barbante, C., and Gambaro, A. (2018). Photo-oxidation products of λ-pinene in coarse, fine and ultrafine aerosol: A new high sensitive HPLC-MS/MS method. *Atmospheric Environment*, 180:149–155.

Feltracco, M., Barbaro, E., Spolaor, A., Vecchiato, M., Callegaro, A., Burgay, F., Vardè, M., Maffezzoli, N., Dallo, F., Scoto, F., Zangrando, R., Barbante, C., and Gambaro, A. (2021). Year-round measurements of size-segregated low molecular weight organic acids in Arctic aerosol. *Science of The Total Environment*, 763:142954.

Garrett, T., Brattström, S., Sharma, S., Worthy, D., and Novelli, P. (2011). The role of scavenging in the seasonal transport of black carbon and sulfate to the Arctic. *Geophysical Research Letters - GEOPHYS RES LETT*, 38.

Giardi, F., Becagli, S., Traversi, R., Frosini, D., Severi, M., Caiazzo, L., Ancillotti, C., Cappelletti, D., Moroni, B., Grotti, M., Bazzano, A., Lupi, A., Mazzola, M., Vitale, V., Abollino, O., Ferrero, L., Bolzacchini, E., Viola, A., and Udisti, R. (2016). Size distribution and ion composition of aerosol collected at Ny-Ålesund in the spring–summer field campaign 2013. *Rendiconti Lincei*, 27.

Gilardoni, S., Heslin-Rees, D., Mazzola, M., Vitale, V., Sprenger, M., and Krejci, R. (2023). Drivers controlling black carbon temporal variability in the lower troposphere of the European Arctic. *Atmospheric Chemistry and Physics*, 23(24):15589–15607. Publisher: Copernicus GmbH.

Gillett, N. P., Weaver, A. J., Zwiers, F. W., and Flannigan, M. D. (2004). Detecting the effect of climate change on Canadian forest fires. *Geophysical Research Letters*, 31(18). _eprint: https://onlinelibrary.wiley.com/doi/pdf/10.1029/2004GL020876.

González, R., Toledano, C., Román, R., Fuertes, D., Berjón, A., Mateos, D., Guirado-Fuentes, C., Velasco-Merino, C., Antuña-Sánchez, J. C., Calle, A., Cachorro, V. E., and de Frutos, á. M. (2020). Daytime and nighttime aerosol optical depth implementation in CÆLIS. *Geoscientific Instrumentation, Methods and Data Systems*, 9(2):417–433. Publisher: Copernicus GmbH.

Huang, J. and Jaeglé, L. (2017). Wintertime enhancements of sea salt aerosol in polar regions consistent with a sea ice source from blowing snow. *Atmospheric Chemistry and Physics*, 17(5):3699–3712. Publisher: Copernicus GmbH.

Iqbal, M. (1983). An Introduction To Solar Radiation - 1st Edition.

Kasischke, E. S. and Turetsky, M. R. (2006). Recent changes in the fire regime across the North American boreal region—Spatial and temporal patterns of burning across Canada and Alaska. *Geophysical Research Letters*, 33(9). _eprint: https://onlinelibrary.wiley.com/doi/pdf/10.1029/2006GL025677.

Kharuk, V. I. and Ponomarev, E. I. (2017). Spatiotemporal characteristics of wildfire frequency and relative area burned in larch-dominated forests of Central Siberia. *Russian Journal of Ecology*, 48(6):507–512.

Kyrö, E.-M., Kerminen, V.-M., Virkkula, A., Dal Maso, M., Parshintsev, J., Ruíz-Jimenez, J., Forsström, L., Manninen, H. E., Riekkola, M.-L., Heinonen, P., and Kulmala, M. (2013). Antarctic new particle formation from continental biogenic precursors. *Atmospheric Chemistry and Physics*, 13(7):3527–3546. Publisher: Copernicus GmbH.

Lynch, P., Reid, J. S., Westphal, D. L., Zhang, J., Hogan, T. F., Hyer, E. J., Curtis, C. A., Hegg, D. A., Shi, Y., Campbell, J. R., Rubin, J. I., Sessions, W. R., Turk, F. J., and Walker, A. L. (2016). An 11-year global gridded aerosol optical thickness reanalysis (v1.0) for atmospheric and climate sciences. *Geoscientific Model Development*, 9(4):1489–1522. Publisher: Copernicus GmbH.

Markowicz, K. M., Pakszys, P., Ritter, C., Zielinski, T., Udisti, R., Cappelletti, D., Mazzola, M., Shiobara, M., Xian, P., Zawadzka, O., Lisok, J., Petelski, T., Makuch, P., and Karasiński, G. (2016). Impact of North American intense fires on aerosol optical properties measured over the European Arctic in July 2015. *Journal of Geophysical Research: Atmospheres*, 121(24):14,487–14,512. _eprint: https://onlinelibrary.wiley.com/doi/pdf/10.1002/2016JD025310.

Mazzola, M., Viola, A. P., Lanconelli, C., and Vitale, V. (2016). Atmospheric observations at the Amundsen-Nobile Climate Change Tower in Ny-Ålesund, Svalbard. *Rendiconti Lincei*, 27(1):7–18.

McCarty, J. L., Smith, T. E. L., and Turetsky, M. R. (2020). Arctic fires re-emerging. *Nature Geoscience*, 13(10):658–660. Number: 10 Publisher: Nature Publishing Group.

O'Dowd, C. D., Smith, M. H., Consterdine, I. E., and Lowe, J. A. (1997). Marine aerosol, sea-salt, and the marine sulphur cycle: a short review. *Atmospheric Environment*, 31:73–80. ADS Bibcode: 1997AtmEn..31...73O.

Ohneiser, K., Ansmann, A., Chudnovsky, A., Engelmann, R., Ritter, C., Veselovskii, I., Baars, H., Gebauer, H., Griesche, H., Radenz, M., Hofer, J., Althausen, D., Dahlke, S., and Maturilli, M. (2021). The unexpected smoke layer in the High Arctic winter stratosphere during MOSAiC 2019–2020. *Atmospheric Chemistry and Physics*, 21(20):15783–15808. Publisher: Copernicus GmbH.

Paatero, P. and Tapper, U. (1994). Positive matrix factorization: A non-negative factor model with optimal utilization of error estimates of data values. *Environmetrics*, 5(2):111–126.

Pandolfi, M., Alados-Arboledas, L., Alastuey, A., Andrade, M., Angelov, C., Artiñano, B., Backman, J., Baltensperger, U., Bonasoni, P., Bukowiecki, N., Collaud Coen, M., Conil, S., Coz, E., Crenn, V., Dudoitis, V., Ealo, M., Eleftheriadis, K., Favez, O., Fetfatzis, P., Fiebig, M., Flentje, H., Ginot, P., Gysel, M., Henzing, B., Hoffer, A., Holubova Smejkalova, A., Kalapov, I., Kalivitis, N., Kouvarakis, G., Kristensson, A., Kulmala, M., Lihavainen, H., Lunder, C., Luoma, K., Lyamani, H., Marinoni, A., Mihalopoulos, N., Moerman, M., Nicolas, J., O'Dowd, C., Petäjä, T., Petit, J.-E., Pichon, J. M., Prokopciuk, N., Putaud, J.-P., Rodríguez, S., Sciare, J., Sellegri, K., Swietlicki, E., Titos, G., Tuch, T., Tunved, P., Ulevicius, V., Vaishya, A., Vana, M., Virkkula, A., Vratolis, S., Weingartner, E., Wiedensohler, A., and Laj, P. (2018). A European aerosol phenomenology – 6: scattering properties of atmospheric aerosol particles from 28 ACTRIS sites. *Atmospheric Chemistry and Physics*, 18(11):7877–7911. Publisher: Copernicus GmbH.

Quinn, P. K., Bates, T. S., Baum, E., Doubleday, N., Fiore, A. M., Flanner, M., Fridlind, A., Garrett, T. J., Koch, D., Menon, S., Shindell, D., Stohl, A., and Warren, S. G. (2008). Short-lived pollutants in the Arctic: their climate impact and possible mitigation strategies. *Atmospheric Chemistry and Physics*, 8(6):1723–1735. Publisher: Copernicus GmbH.

Román, R., González, R., Toledano, C., Barreto, Á., Pérez-Ramírez, D., Benavent-Oltra, J. A., Olmo, F. J., Cachorro, V. E., Alados-Arboledas, L., and de Frutos, á. M. (2020). Correction of a lunar-irradiance model for aerosol optical depth retrieval and comparison with a star photometer. *Atmospheric Measurement Techniques*, 13(11):6293–6310. Publisher: Copernicus GmbH.

Schmeisser, L., Backman, J., Ogren, J. A., Andrews, E., Asmi, E., Starkweather, S., Uttal, T., Fiebig, M., Sharma, S., Eleftheriadis, K., Vratolis, S., Bergin, M., Tunved, P., and Jefferson, A. (2018). Seasonality of aerosol optical properties in the Arctic. *Atmospheric Chemistry and Physics*, 18(16):11599–11622. Publisher: Copernicus GmbH.

Serreze, M. C. and Barry, R. G. (2011). Processes and impacts of Arctic amplification: A research synthesis. *Global and Planetary Change*, 77(1-2):85–96.

Shaw, G. E. (1995). The Arctic Haze Phenomenon. *Bulletin of the American Meteorological Society*, 76(12):2403–2413. Publisher: American Meteorological Society.

Sinyuk, A., Holben, B. N., Eck, T. F., Giles, D. M., Slutsker, I., Korkin, S., Schafer, J. S., Smirnov, A., Sorokin, M., and Lyapustin, A. (2020). The AERONET Version 3 aerosol retrieval algorithm, associated uncertainties and comparisons to Version 2. *Atmospheric Measurement Techniques*, 13(6):3375–3411. Publisher: Copernicus GmbH.

Stockwell, C. E., Veres, P. R., Williams, J., and Yokelson, R. J. (2015). Characterization of biomass burning emissions from cooking fires, peat, crop residue, and other fuels with high-resolution proton-transfer-reaction time-of-flight mass spectrometry. *Atmospheric Chemistry and Physics*, 15(2):845–865. Publisher: Copernicus GmbH.

Stohl, A. (2006). Characteristics of atmospheric transport into the Arctic troposphere. *Journal of Geophysical Research: Atmospheres*, 111(D11). _eprint: https://onlinelibrary.wiley.com/doi/pdf/10.1029/2005JD006888.

Stohl, A., Klimont, Z., Eckhardt, S., Kupiainen, K., Shevchenko, V. P., Kopeikin, V. M., and Novigatsky, A. N. (2013). Black carbon in the Arctic: the underestimated role of gas flaring and residential combustion emissions. *Atmospheric Chemistry and Physics*, 13(17):8833–8855. Publisher: Copernicus GmbH.

Tomasi, C., Fuzzi, S., and Kokhanovsky, A. (2017). *Atmospheric Aerosols: Life Cycles and Effects on Air Quality and Climate*. John Wiley & Sons. Google-Books-ID: 5bCGDQAAQBAJ.

Tomasi, C., Kokhanovsky, A. A., Lupi, A., Ritter, C., Smirnov, A., O'Neill, N. T., Stone, R. S., Holben, B. N., Nyeki, S., Wehrli, C., Stohl, A., Mazzola, M., Lanconelli, C., Vitale, V., Stebel, K., Aaltonen, V., de Leeuw, G., Rodriguez, E., Herber, A. B., Radionov, V. F., Zielinski, T., Petelski, T., Sakerin, S. M., Kabanov, D. M., Xue, Y., Mei, L., Istomina, L., Wagener, R., McArthur, B., Sobolewski, P. S., Kivi, R., Courcoux, Y., Larouche, P., Broccardo, S., and Piketh, S. J. (2015). Aerosol remote sensing in polar regions. *Earth-Science Reviews*, 140:108–157.

Udisti, R., Bazzano, A., Becagli, S., Bolzacchini, E., Caiazzo, L., Cappelletti, D., Ferrero, L., Frosini, D., Giardi, F., Grotti, M., Lupi, A., Malandrino, M., Mazzola, M., Moroni, B., Severi, M., Traversi, R., Viola, A., and Vitale, V. (2016). Sulfate source apportionment in the Ny-Ålesund (Svalbard Islands) Arctic aerosol. *Rendiconti Lincei*, 27.

Veraverbeke, S., Rogers, B. M., Goulden, M. L., Jandt, R. R., Miller, C. E., Wiggins, E. B., and Randerson, J. T. (2017). Lightning as a major driver of recent large fire years in North American boreal forests. *Nature Climate Change*, 7(7):529–534. Number: 7 Publisher: Nature Publishing Group.

Virkkula, A. (2010). Correction of the Calibration of the 3-wavelength Particle Soot Absorption Photometer (3λ PSAP). *Aerosol Science and Technology*, 44(8):706–712. Publisher: Taylor & Francis _eprint: https://doi.org/10.1080/02786826.2010.482110.

Voronova, O., Zima, A., Kladov, V., and Cherepanova, E. (2020). Anomalous Wildfires in Siberia in Summer 2019. *Izvestiya, Atmospheric and Oceanic Physics*, 56:1042–1052.

Witek, M. L., Flatau, P. J., Teixeira, J., and Westphal, D. L. (2007). Coupling an ocean wave model with a global aerosol transport model: A sea salt aerosol parameterization perspective. *Geophysical Research Letters*, 34(14). _eprint: https://agupubs.onlinelibrary.wiley.com/doi/pdf/10.1029/2007GL030106.

Witze, A. (2020). The Arctic is burning like never before — and that's bad news for climate change. *Nature*, 585(7825):336–337. Bandiera_abtest: a Cg_type: News Number: 7825 Publisher: Nature Publishing Group Subject_term: Forestry, Environmental sciences, Atmospheric science, Climate change.

Zangrando, R., Barbaro, E., Vecchiato, M., Kehrwald, N. M., Barbante, C., and Gambaro, A. (2016). Levoglucosan and phenols in Antarctic marine, coastal and plateau aerosols. *Science of The Total Environment*, 544:606–616.

Zielinski, T., Bolzacchini, E., Cataldi, M., Ferrero, L., Graßl, S., Hansen, G., Mateos, D., Mazzola, M., Neuber, R., Pakszys, P., Posyniak, M., Ritter, C., Severi, M., Sobolewski, P., Traversi, R., and Velasco-Merino, C. (2020). Study of Chemical and Optical Properties of Biomass Burning Aerosols during Long-Range Transport Events toward the Arctic in Summer 2017. *Atmosphere*, 11(1):84. Number: 1 Publisher: Multidisciplinary Digital Publishing Institute.

Ångström, A. (1929). On the Atmospheric Transmission of Sun Radiation and on Dust in the Air. *Geografiska Annaler*, 11:156–166. Publisher: [Wiley, Swedish Society for Anthropology and Geography].

Chapter 5

Monitoring Aerosol Optical Depth during the Arctic night: instrument development and first results

In this second research paper, we investigated the robustness and reliability of the lunar photometry technique at high-latitude stations. Monitoring aerosols in the Arctic and Antarctica during the polar night is challenging because standard solar-based instruments cannot operate without sunlight. To address this, we used instruments that measure aerosol optical depth (AOD) using the Moon as a stable light source. Measurements were conducted at Barrow (Alaska) and Ny-Ålesund (Svalbard), and a careful calibration and data-processing procedure was applied to ensure accurate results. The main findings show that lunar photometry provides reliable AOD measurements during the Arctic night, with uncertainties ranging from 0.006 to 0.030 (depending on instrument). AOD values derived from lunar photometry were consistent with those reported for periods just before and after the polar night. At Ny-Ålesund, lunar photometry results also closely matched data from star photometers and the Cimel CE318-T sun–sky–lunar photometer, confirming the validity of using moonlight for aerosol monitoring under polar night conditions.

Published as:

Mazzola M., Stone R.S., Kouremeti N., Vitale V., Gröbner J., Stebel K., Hansen G.H., Stone T.C., Ritter C., PULIMENO S., 2024, *Monitoring aerosol optical depth during the Arctic night: Instrument development and first results*, Atm. Res., 311, https://doi.org/10.1016/j.atmosres.2024.107667.

5.1 Abstract

Moon-photometric measurements were made at two locations in the Arctic during winter nights using two different modified Sun photometers; a Carter Scott SP02 and a Precision Filter Radiometer (PFR) developed at PMOD/WRC. Values of aerosol optical depth (AOD) were derived from spectral irradiance measurements made at four wavelengths for each of the devices. The SP02 was located near Barrow, Alaska and recorded data from November 2012 to March 2013, spanning five lunar cycles, while the PFR was deployed to Ny- Ålesund, Svalbard each winter from February 2014 to February 2019 for a total of 66 measurement periods. A methodology was developed to process the raw data, involving calibration of the instruments and normalizing measured spectral irradiance values in accordance with site- specific determinations of the extraterrestrial atmospheric irradiance (ETI) as Moon phase cycled. Uncertainties of the derived AOD values were also evaluated and found to be in the range, 0.006 - 0.030, depending on wave- length and which device was evaluated.

The magnitudes of AOD determined for the two sites were in general agreement with those reported in the literature for sunlit periods just before and after the dark periods of Arctic night. Those for the PFR were also compared with data obtained using star photometers and a Cimel CE318-T, recently deployed to Ny-Ålesund, showing that Moon photometry is viable as a means to monitor AOD during the Arctic night. Such data are valuable for more complete assessments of the role aerosols play in modulating climate, the validation of AOD derived using various remote sensing techniques, and applications related to climate modeling.

5.2 Introduction

Atmospheric aerosols play an important role in shaping planetary climate. Their interaction with solar and terrestrial radiation, involving both diffusion and absorption, alters the energy radiative balance at various levels of the lower atmosphere. Similarly, their ability to influence cloud characteristics, such as droplet size and liquid water content, and their persistence further enhances their impact on the overall definition of the climatic system (IPCC 2023).

The monitoring of aerosol content in the vertical column is currently conducted using both ground-based and space-borne platforms. Passive techniques utilize the extinction and/or diffusion of solar radiation to retrieve this quantity through the inversion of measured signals (Shaw 1983; Kaufman and Joseph 1982). LIDARs use a laser beam as a radiation source and, therefore, do not require the presence of the Sun. They exhibit superior performance during the night, as the absence of solar radiation reduces the radiation noise entering the detector (Hoffmann et al. 2010). Hence, techniques for aerosol monitoring during the night already exist, including star photometry, where the sources of radiation are the stars (Pérez-Ramírez et al. 2008).

Even though the primary source of energy for the Earth is derived from the Sun, there are compelling reasons to quantify aerosol columnar content during the night. These include studying the indirect effects of aerosols on long-wave radiation (Lubin and Vogelmann 2006), complementing other measurements such as backscatter profiles obtained by LIDARs (both ground and satellite-based, Brunamonti et al. 2021), detecting transport to polar regions during winter (Zhao et al. 2022) and, importantly, filling gaps in AOD climatologies (Stone et al. 2014).

One of the earliest attempts to utilize the Moon as a source of radiation for photometric measurements was undertaken by Esposito et al. 1998. They captured Moon-reflected radiation in the spectral range of 320-640 nm using a system consisting of a scanning monochromator, a focal lens, and a photo-multiplier. Applying the Langley plot method to a night of measurements near Potenza, in the South of Italy, they derived calibration factors and Aerosol Optical Depth (AOD) simultaneously. The same technique was employed for a four-day period in a desert site in Namibia as well (Esposito et al. 2003).

Herber et al. 2002 reported, for the first time, continuous day and night AOD measurements in the Arctic using Sun, Moon, and star photometry across different periods of the year. In terms of lunar measurements, they employed the same technique as Esposito et al. 1998, constructing a Langley plot for each suitable measurement period and applying it to that specific period. This approach helped overcoming challenges related to variations in lunar brightness arising from the Moon's phase.

Berkoff et al. 2011 introduced, for the first time, the approach adopted in the present work, utilizing an empirical model to replicate the lunar exo-atmospheric spectral irradiance (EAI). They employed the highest gain setting of an unmodified Cimel CE318 sun-photometer for measurements and evaluated the existing capabilities while identifying enhancements required for day/night operation.

Barreto et al. 2013a presented a new lunar photometer prototype, the Cimel CE318-U. This prototype featured a built-in lunar tracking system and an improved signal amplification system for channels ranging from 440 to 1640 nm. Additionally, the study introduced three methods for calibrating the new lunar photometer. The same instrument was employed by Barreto et al. 2013b for the retrieval of precipitable water vapor during the night. An advanced version of this instrument, the CE318-T, was introduced in Barreto et al. 2016. The CE318-T demonstrated the capability to conduct both daytime and nighttime photometric measurements using the sun and the moon as light sources (Perrone et al. 2022; Herrero del Barrio et al. 2023). The AErosol RObotic NETwork (AERONET) is adopting this new instrument as the standard for its network (`https://aeronet.gsfc.nasa.gov/cgi-bin/webtool_aod_v3_lunar`, accessed 01/01/2024).

Very recently a modified POM-02 from Prede have been used by Uchiyama et al. 2019 for the estimation of AOD values near Tokyo (Japan), concluding that they have the same reliability between day and night. Attempts of retrieving nighttime AOD from satellite observations of reflected moonlight have been also conducted by Zhou et al. 2021 over the USA, obtaining results with an uncertainty higher to that obatined by model results when compared to AERONET and CALIOP data.

In this paper we report the results from measurements performed with this technique at two sites in the Arctic region, Barrow (Alaska) and Ny-Ålesund, using two different instruments. In Section 5.3 we illustrate the methodology, including calibration and uncertainties assessment, and the adopted instrumentation, while in Section 5.4, we show the results of the measurements we get. Finally, in Section 5.5 we draw conclusion about this emerging technology.

5.3 Methodology and instrumentation

5.3.1 Differences with sun photometry

There are two primary distinctions between Sun and Moon photometry: (i) the fluctuation of reflected irradiance throughout the lunar cycle, attributed to changes in

moon phase and distance from the Earth, and (ii) the exceedingly low magnitude of the irradiance reaching the Earth's surface and needs to be measured.

When dealing with sun photometry technique, the Lambert-Beer law applies:

$$J_\lambda = \frac{J_{0,\lambda}}{R^2} e^{-m\tau_\lambda}. \tag{5.1}$$

The signal measured at the ground at wavelength λ is denoted as J_λ, with $J_{0,\lambda}$ representing the calibration factor at the same wavelength, i.e., the signal hypothetically measured outside the atmosphere or in its absence. Here, R represents the Sun-Earth distance expressed in astronomical units (A.U.), m denotes the relative optical air mass, and τ_λ represents the atmospheric total optical depth. The total optical depth is the sum of contributions from scattering from air and absorption due to minor gases, primarily ozone and nitrogen dioxide, along with the extinction due to aerosols.

When utilizing the Moon as a radiation source, it is crucial to acknowledge that its brightness, unlike the Sun, is not constant. The brightness of the Moon as observed from Earth varies based on the actual geometric configuration between the Sun, the Moon, and the observer, encompassing factors such as the lunar phase and libration (Uchiyama et al. 2019). The amount of reflected radiation reaching the top of the atmosphere is proportional to the Moon albedo, and also the Moon-observer distance d needs to be considered:

$$J_\lambda = \frac{J^*_{0,\lambda}}{(Rd)^2} e^{-m\tau_\lambda} \tag{5.2}$$

with

$$J^*_{0,\lambda} \propto \frac{A_\lambda \Omega E_\lambda}{\pi} \tag{5.3}$$

where A_λ represents the disk-equivalent lunar albedo at the wavelength λ, Ω denotes the solid angle of the Moon, and E_λ is the standard extraterrestrial solar irradiance at the wavelength λ. In brief, the right part of the equation describes the lunar-reflected irradiance at the wavelength λ.

The USGS lunar calibration program has developed the RObotic Lunar Observatory (ROLO), a model of the equivalent reflectance of the lunar disk as a function of geometry, using an empirically derived analytic form based on the primary geometric variables, i.e. absolute phase angle, selenographic latitude and longitude of the observer, and selenographic longitude of the Sun (Kieffer and Stone 2005). The validity of this model extends to the first and third quarters of the Moon phase, encompassing lunar albedo and the Moon-observer distance, both of which exhibit continuous variations throughout the lunar cycle.

By normalizing the measured signals with respect to the reflected irradiance, the resulting formula mirrors that used in sun photometry

$$J^*_\lambda = \frac{J^*_{0,\lambda}}{(Rd)^2} e^{-m\tau_\lambda} \tag{5.4}$$

with

$$J^*_\lambda = \frac{J_\lambda}{(\frac{A_\lambda \Omega E_\lambda}{\pi})} \tag{5.5}$$

Notably, the new signals and calibration constants remain independent of the specific lunar phase. It is worth noting here that the absolute value of the irradiance is not needed here, as the Langley method brings to a relative calibration of the instrument. For this work, the EAI values were provided by the ROLO developers

at USGS for the spectral channels of the adopted instruments. A freely accessible implementation of the original algorithm has been released (Barreto et al. 2017, 2019; Román et al. 2020) by the investigator involved in the POLAR-AOD community (Tomasi et al. 2012).

The radiation signals reflected by the Moon and reaching the Earth have been estimated to be between 5 and 6 orders of magnitude smaller than those directly emitted by the Sun. This discrepancy varies depending on the wavelength and falls within the spectral range typically utilized for aerosol measurements (300-1000 nm). Traditional sun photometers are, therefore, incapable of measuring these extremely low signals. As a result, specific modifications are necessary to adapt them for this purpose.

5.3.2 Instrumentation

In this work we used two different modified sun photometers at two sites: a Carter Scott (now Middleton Solar Inc.) SP02 that has been modified at the NOAA/GMD laboratories in Boulder, CO, in order to increase the amplification, and a Precision Filter Radiometer (PFR) designed by PMOD and then specifically modified with the same aim.

The SP02 is equipped with four spectral channels, each centered at wavelengths 425, 500, 675, and 862 nm. The interior of the instrument, particularly the section housing the filters and sensors, is thermally stabilized to maintain a consistent response during various measurement periods, including calibration. The sole adjustment made involves increasing the electronic amplification of the signals. To assess the dark signal for the four channels of the photometer, measurements were conducted immediately before moon rise and after moon set. Data were logged at one-minute intervals using a Campbell CR10X datalogger.

Regarding the PFR, modifications were implemented by increasing the first and second stage amplifications, resulting in a supplementary gain of up to 10^4. Additionally, the filter apertures' diameter was enlarged from 3 to 6 mm, contributing to another 4x gain. To address the challenges posed by weak signals at shorter wavelengths, the original 368 nm filter in the PFR was replaced with one at 675 nm. The other wavelengths are centered at 412, 500 and 862 nm. This instrument conducts measurements at the top of each minute and is equipped with a shutter system that enables the measurement of dark signals between consecutive measurements. This feature has proven crucial for lunar measurements in polar sites, allowing the detection of extremely low signals at very low temperatures. In 2015, further enhancements were made to improve the signal-to-noise ratio. Notably, the Campbell CR10X datalogger typically used with the PFR system was replaced with a SACRAM OWEL datalogger. After that, the instrument has been fully characterized using the radiometric calibration laboratory facilities of PMOD/WRC. This included filter function, sensors response linearity and absolute irradiance calibration. From here on we will refer to this second version as PFR2015, to distinguish it from the first modified PFR when not implicitly obvious.

Figure 5.1 shows the raw signals (upper panel) and normalized signals (lower panel) obtained using the modified PFR for two measurement periods: one during the first quarter, with a 50% illuminated fraction (left part), and another near the full Moon with a 90% illumination fraction (right part). As observed in the upper panel, transitioning from the first quarter to near full Moon conditions results in raw signals increasing by approximately a factor of 5. Only a small portion of this increase

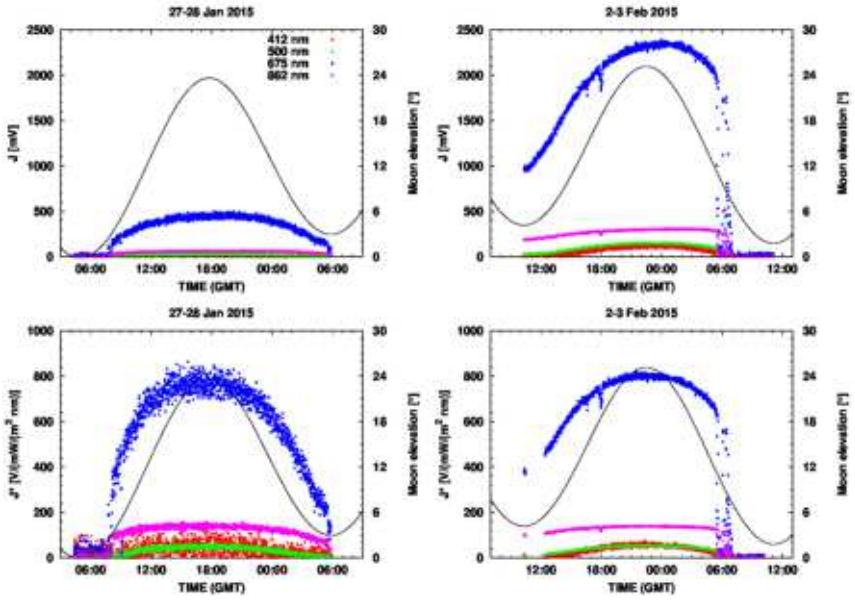

FIGURE 5.1: Raw signals (upper panel) and normalized signals (lower panel) for the four channels of the Moon PFR (first version) obtained at Ny-Ålesund for two measurement periods: one at the first quarter with 50% of illuminated fraction (left part) and another near the full Moon with 90% of illuminated fraction (right part). The Moon's elevation is also shown in each panel by the black line.

can be attributed to the change in Moon elevation, which shifts from 24.7° to 26.1° between the first and second period. In contrast, the signal noise remains similar in both cases, resulting in a higher signal-to-noise (S/N) ratio for the near full Moon scenario (appreciable only for the 675 nm channel in the figure). It's important to note that the peak of the measured signals does not align with the maximum elevation in time, owing to the complex geometry of the system.

After normalization the signals become comparable in strength for the two periods, making it easier to appreciate the lower S/N ratio in the case of 50% Moon illumination. Simultaneously, it is possible to observe the shift of the signals' maxima towards the position of the elevation maxima.

5.3.3 Calibration

As anticipated, the instrument calibration was conducted using the Langley plot method. This method involves extrapolating the logarithm of normalized signals as a function of air mass towards the zero value (Barreto et al. 2013a). Typically, this method yields better results in stable atmospheric conditions with respect to particle content. Consequently, it is commonly employed at high-altitude mountain sites where aerosol extinction and atmospheric pressure changes occurring over a few hours are generally minimal.

The SP02 photometer was calibrated at the Mauna Loa Observatory (MLO, 19° 32' N, 155° 34' W, 3397 m a.s.l.) over four lunar cycles between August and October 2012. The results obtained were then adopted for subsequent measurements taken at Barrow. In contrast, the PFR instruments underwent its initial calibration at the Izaña Atmospheric Observatory (IZO, 28° 18' N, 16° 29' W, 2373m a.s.l.) over four lunar cycles during the summer of 2015 (May-September), and these results were

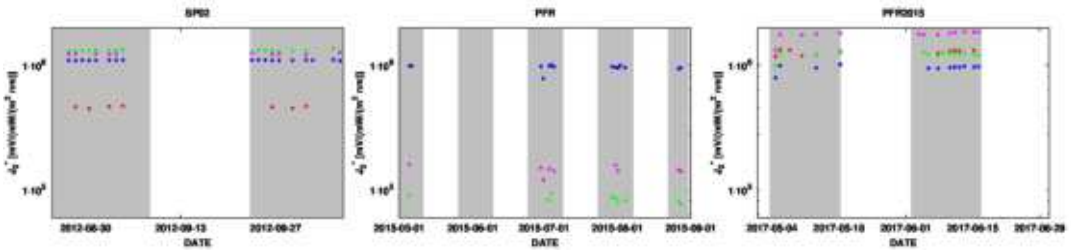

FIGURE 5.2: Time evolution of the calibration factors obtained using the Langley method for the SP02 photometer at Mauna Loa (first panel on the left) and for the PFR photometers at Izaña (PFR in the panel in the middele and PFR2015 in tbe panel on the right). Shaded areas indicate the first-third quarter periods; Wavelengths are represented by the same color scheme shown in Fig.5.1.

		Ch1	Ch2	Ch3	Ch4
SP02	Average	4.651e+05	1.316e+06	1.103e+06	1.240e+06
	St.Dev.	8.732e+03 (1.9%)	2.036e+04 (1.5%)	5.830e+03 (0.5%)	1.441e+04 (1.2%)
	N	7	16	18	10
	$< \sigma_y >$	0.019	0.005	0.003	0.003
PFR	Average	1.508e+05	8.357e+04	9.792e+05	1.454e+05
	St.Dev.	-	2.411e+03 (2.9%)	2.023 (2.1%)	3.726 (2.6%)
	N	2	7	13	6
	$< \sigma_y >$	-	0.014	0.007	0.014
PFR2015	Average	1.305e+06	1.240e+06	9.686e+05	1.820e+06
	St.Dev.	2.802e+04 (2.1%)	2.181e+04 (1.8%)	1.215e+04 (1.3%)	4.099e+04 (2.3%)
	N	5	10	8	8
	$< \sigma_y >$	0.004	0.003	0.002	0.002

TABLE 5.1: Calibration factors statistics for the four spectral channels of both the SP02 and PFR photometers. $< \sigma_y >$ is the RMSD average value for each set of Langley results. The spectral channels for the SP02 include 425, 500, 675, and 862 nm, while those for the PFRs are 412, 500, 675, and 862 nm.

subsequently applied to measurements previously recorded at Ny-Ålesund. After the modifications applied to the instrument during 2015, the instrument was calibrated in 2017 at the same site during the inter-comparison campaign whose results are described in Barreto et al. 2019.

The goodness of a valid Langley plot was evaluated by both an automated method, as described in Mazzola et al. 2010, but also by visual inspection. Due to the higher S/N ratio values it the Moon case, the root mean square difference (RMSD) limit for the fits was set to 0.020 for SP02 and first version of lunar PFR instead of the 0.006 value suggested by Harrison and Michalsky 1994 for the Sun. For PFR2015 we used the original value of Harrison and Michalsky 1994 for this parameter. The values of RMSD will be used to evaluate the contribution of measured signals to AOD uncertainties (see Sec. 5.3.4). Figure 5.2 shows the time series of the calibration factors obtained for the two instruments.

Table 5.1 presents the calibration constants as average values for the two instruments, along with associated standard deviations and the number of valid fits. The RMSD average value for each set of Langley results is also reported ($< \sigma_y >$). For the PFR, the factors obtained both before and after the modifications of 2015 are reported. Additionally, Langley fits were evaluated using measurements from the two polar sites, yielding similar values for the calibration constants.

5.3.4 Uncertainty

The Lambert-Beer law implies that the uncertainty in aerosol optical depth can be represented as the quadratic sum of terms arising from the various parameters involved in the equation (refer to, for example, Mazzola et al. 2010, Eq. 5).

In sun photometry, the term associated with errors in the signal measurement is usually neglected, being much smaller than the other terms. This is not the case when dealing with the Moon and the normalized signals, as is clear looking at Figure 5.1. This term should take into account also the uncertainty due to signal normalization itself, i.e. that associated with the EAI calculation. In that sense it would read as the quadratic sum of the term associated with the raw signals and that associated with the normalization

$$\left(\frac{\Delta J^*_\lambda}{J^*_\lambda}\right)^2 + \left(\frac{\Delta k_\lambda}{k_\lambda}\right)^2 \tag{5.6}$$

where k_λ is the term on the right side of Equation 5.2. The uncertainty on k_λ has been estimated by the ROLO developers to be 3% in the 300-1000 nm spectral range (personal communication). Given the challenging nature of signal evaluation, we opted to estimate the uncertainty associated with the normalized signals. This estimation was accomplished by leveraging measurements obtained under clear sky conditions.

The uncertainty on the normalized signals has been evaluated by considering their ripple around the Langley fit line for the periods selected as good for calibration. In that sense, the $< \sigma_y >$ values reported in Table 5.1 are the average of the square root deviation of the logarithm of the normalized signals. As $d(log(x)) = dx/x$, the term $\Delta J^*_\lambda / J^*_\lambda$ can be taken equal to $< \sigma_y >$. Its values ranged between 0.3% and 1.9% for the SP02 and between 0.7% and 1.4% (first version) and 0.2% and 0.4% (second version) for the PFR.

The uncertainty associated with the calibration constant was assessed using the relative standard deviation linked to its average value. As indicated in Table 5.1, it was observed to vary across different channels, ranging between 0.5% and 1.9% for SP02, between 2.1% and 4.4% for PFR and between 1.8%-2.9% for the PFR2015.

Uncertainties associated with Rayleigh scattering and gas absorption were derived from Mazzola et al. 2010, as the MFRSR instrument shares similar spectral channels as the SP02 and PFR, and having adopted identical algorithms for these minor corrections.

Table 5.2 reports for each considered wavelength the uncertainties evaluated for the normalized signals and calibration coefficients, as well as the total values obtained summing in quadrature the terms, including Rayleigh and gas absorption as stated above. Actually, the first two terms depend on the value of the optical air mass, and the table report the values for $m = 1$. Due to the inclination of the lunar orbital plane with respect to the Earth ecliptic (5°), in the polar circle the Moon reaches a maximum daily elevation of about 52°, that turns in m values always greater than 1.6. Conversely, there are days in which the Moon doesn't rise at all. It is worth noting here that the contributions from Rayleigh and gas absorption are negligible in comparison to the total uncertainties. Overall, these uncertainties vary between 0.006 and 0.027 for SP02, between 0.022 and 0.046 for the PFR and between 0.018 and 0.030 for the PFR2015.

	Channel	$\Delta J^*/J^*$	$\Delta J_0^*/J_0^*$	$\Delta\tau$
SP02	1	0.019	0.019	0.027
	2	0.005	0.015	0.016
	3	0.003	0.005	0.006
	4	0.003	0.012	0.012
PFR	1	-	-	-
	2	0.014	0.044	0.046
	3	0.007	0.021	0.022
	4	0.014	0.026	0.030
PFR2015	1	0.004	0.029	0.030
	2	0.003	0.018	0.018
	3	0.002	0.022	0.022
	4	0.002	0.022	0.022

TABLE 5.2: Uncertainties associated with the normalized signals and calibration coefficients, as well as total uncertainties obtained considering also Rayleigh and absorption contribution to AOD at the considered wavelengths.

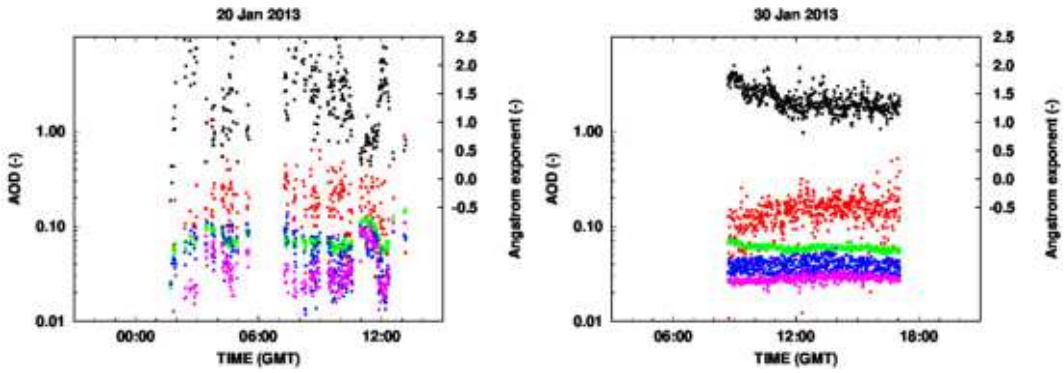

FIGURE 5.3: Spectral AOD obtained using the SP02 at Barrow on January 20, 2013, with 59% of lunar illumination (left), and on January 30, 2013, with 92% illumination (right).

5.4 Measurements and results

5.4.1 Barrow, Alaska

Data from 5 lunar cycles where acquired at the Barrow Atmospheric Baseline Observatory (71° 19' N, 156° 37' W, 11 m a.s.l.), about 8 km northeast of the village of Utqiaġvik (Alaska), from end of November 2012 to end of March 2013. Over these, only the first three cycles gave good data. The photometer was installed on a reprogrammed solar tracker in order to follow the Moon movement. The photometer was also paired with a webcam installed on the same tracker, in order to capture lunar images useful to visually check both the tracking and the presence of clouds along the line of sight. Figure 5.3 shows the AOD obtained from two different days of measurement, one for low Moon illumination (59%, near the first quarter) and one for high illumination (92%, near full Moon).

As expected, the AOD values are noisier at low illumination, as consequence of the lower S/N ratios. Also, AODs at different channels show different noise: about 13% at 500 nm, 31% at 865nm, 39% at 675 nm and 56% at 412 nm near the first

Season	Lunar cycles	Measurement days
2013/2014	1 (Feb)	3
2014/2015	5 (Oct-Feb)	15
2015/2016	1 (Jan)	2
2016/2017	2 (Jan-Feb)	4
2017/2018	5 (Nov-Mar)	5
2018/2019	5 (Oct-Feb)	22

TABLE 5.3: Number of lunar cycles per winter season and total number of measurement days for Ny-Ålesund.

quarter and 4%, 6%, 14% and 34% near full Moon for the same wavelengths. The same behaviour is present in the α values.

Figure 5.3 displays hourly values of AOD at 500 nm and the Angström Exponent, along with their respective standard deviations, across all available measurement periods. The majority of AOD values fell within the range of 0.05 to 0.10, while the α values ranged between 1 and 2, predominantly centered around 1.5.

The recorded AOD values for both parameters aligned well with the minimum values reported by Tomasi et al. 2012 for the non Arctic Haze periods. This may indicate that particle transport had not yet begun during the period examined (December and January.

On November 26, 2012 around noon, a rapid increase of AOD (from 0.05 to 0.20) and a concurrent decrease in α (from 1.5 down to less than 0.5) was detected, probably due to appearance of thin clouds. A similar phenomena happened on the morning of January 20, 2013. Very high values of α (around 2) were measured on December 28, 2012 probably associated with small particles.

5.4.2 Ny-Ålesund, Svalbard

At the Ny-Ålesund Research Station (78° 55' N, 11° 55' E, 16 m a.s.l.), the instrument was installed on a 2AP Kipp & Zonen solar tracker driven via serial port by a Python code based on the original Matlab lunar position calculator by Darin Koblick (http://it.mathworks.com/matlabcentral/fileexchange/22992-lunar-azimuth-and-altitude-estimation-algorithm/). The correct alignment was periodically checked by visual inspection through two holes present in the instrument mounting plates. The instrument was installed during every winter starting from February 2014, even with different time coverages. Data from a total of 19 lunar cycles where acquired, resulting in 51 measurement periods (day and/or night, Table 5.3).

Figure 5.5 shows two measurements days obtained at Ny-Ålesund with different moon illumination values, similarly to Figure 5.3. Again the noise on the AOD values is higher at low illumination and the spectral channels present different values, the highest in the first channel and the lowest in the third one.

Figure 5.6 shows hourly values and associated standard deviations for the years 2014-2015. AOD values were mainly between 0.05 and 0.1, with few exceptions going up to 0.15. Even higher values must be attributed to thin clouds, since the corresponding alpha value collapses to values close to zero. Again, such values are comparable to the daily averages reported in Tomasi et al. 2012 for the beginning of the sun-photometry season, as well as with the star-photometry data for years between 1997 and 2000. The same results can be found in Toledano et al. 2012 in terms of monthly

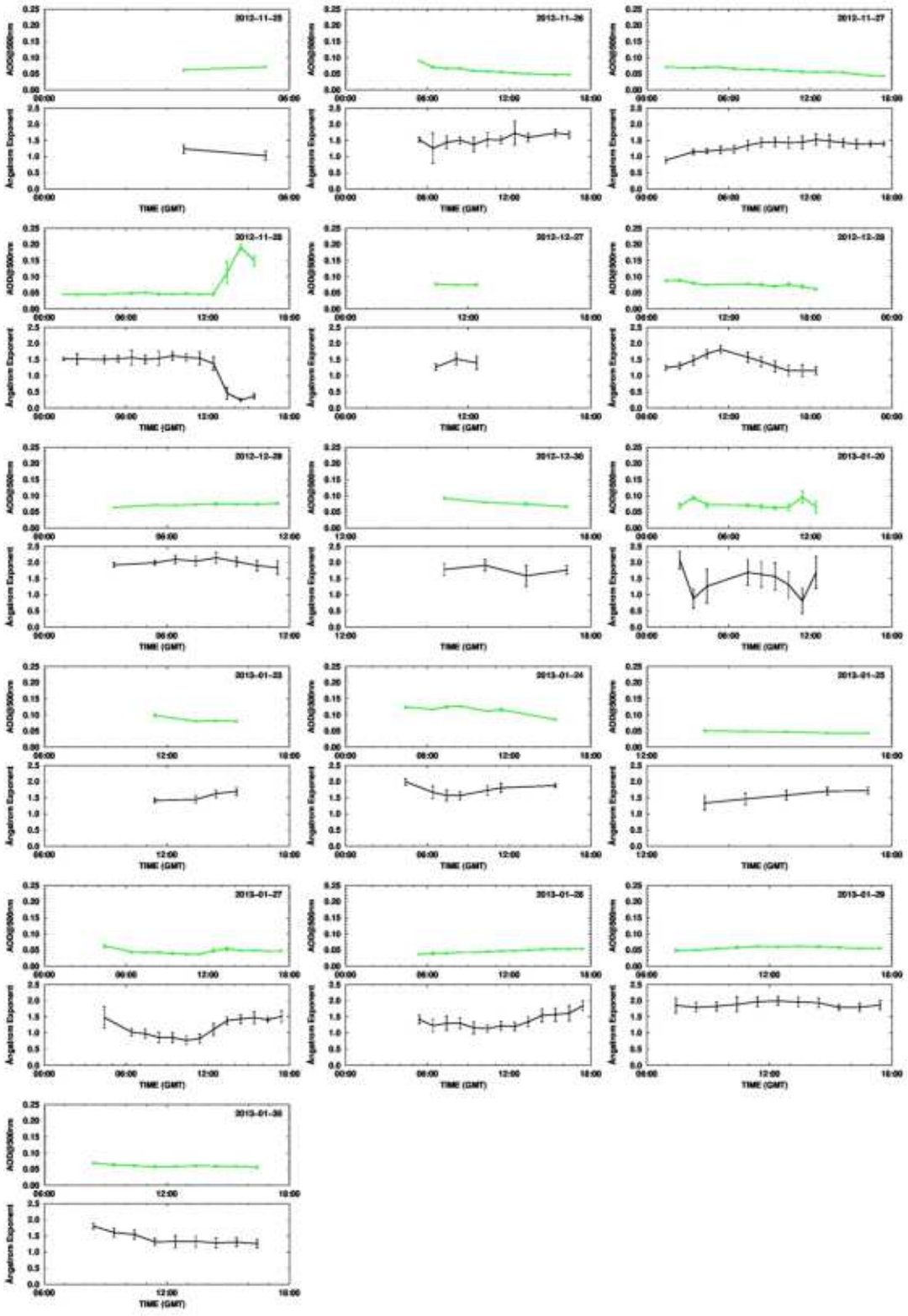

FIGURE 5.4: Hourly averages and standard deviations of AOD at 500 nm and Angström Exponent values obtained during 16 measuring periods at Barrow.

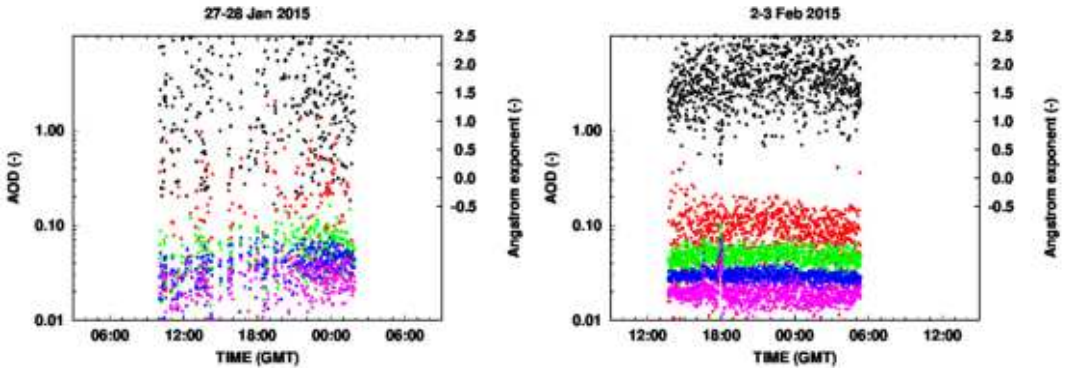

FIGURE 5.5: Spectral AOD obtained using the PFR at Ny-Ålesund on January 27-28, 2015, with 50% of lunar illumination (left), and on February 2-3, 2015, with 96% illumination (right).

values. Values obtained by Sakerin et al. 2018 in Barentsburg in the same years are fully comparable to those found in Ny-Ålesund.

The measurements taken in Ny-Ålesund during January and February 2015 were compared with those performed by AWI using the star photometer, also shown in Figure 5.6. The comparison of both AOD and α is acceptable, being within 0.02 for AOD and 0.5 for α. Only on January 27, 2015 α values were quite different between the two techniques. It is worth noting that this can't be considered a real validation, as the star data are prone to higher uncertainties.

The installation of a sun-sky-lunar Cimel-318T in Ny-Ålesund in 2017 provided the opportunity for a comparative analysis to assess the accuracy of measurements obtained with the modified PFR2015. The lunar AOD data from the Cimel instrument were retrieved from the AERONET webpage, with a 5-minute sampling rate. Unfortunately, the examination of the AOD time series between 2017 and 2020 revealed only a few instances of overlapping periods. In the first months of 2018, the Cimel instrument covered the entire polar night with a good frequency, whereas data for the PFR were only available to a limited extent. During this period, only January 30, 2018 witnessed concurrent measurements from both instruments, occurring between 3:00 am and 8:00 am. During the subsequent polar night, spanning from October 2018 to March 2019, the Cimel instrument covered October and February-March, while the PFR spanned from the end of November to the middle of February. This resulted in a singular overlapping period on February 18, 2019, from 5:00 pm to 10:00 pm. During the polar night of 2020, data collection was limited to measurements obtained solely from the PFR instrument. Unfortunately, no concurrent measurements from the Cimel instrument were available during this period.

Figure 5.7 shows the 5-minute averaged AOD comparison between the PFR and Cimel in Ny-Ålesund for the two measurement periods cited above. Based on these plots, it is evident that on January 30, 2018, both instruments consistently recorded stable behavior with AOD levels hovering around 0.04. There were minor variations between the readings of the two instruments. Conversely, on February 18, 2019, despite an increase in AOD values from 0.06 to 0.15, the measurements from both instruments continued to exhibit good agreement, effectively capturing the emerging trend. Table 5.4 reports detailed statistics for the two periods for AOD at 500 nm for both instruments. The difference between PFR and Cimel median measurements for January 30, 2018 was 0.002, whereas it was higher for February 19, 2019 amounting to 0.005, still an acceptable value when compared to mean values of 0.088 (Table 5.4).

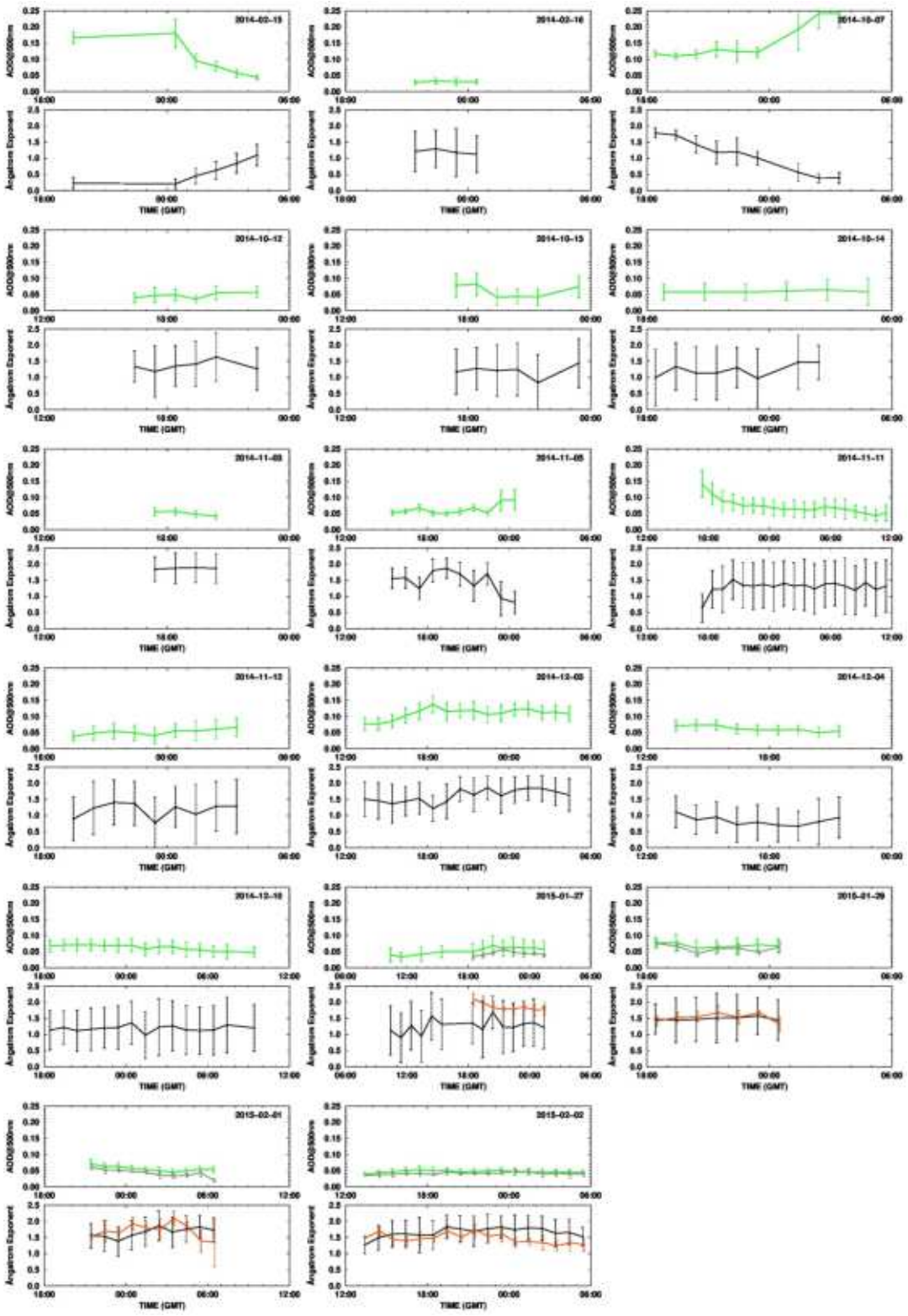

FIGURE 5.6: Hourly averages and standard deviations of AOD at 500 nm and Angström Exponent values obtained during 17 measuring periods at Ny-Ålesund. The grey values for AOD and the orange values for α where measured by the star photometer operated by AWI.

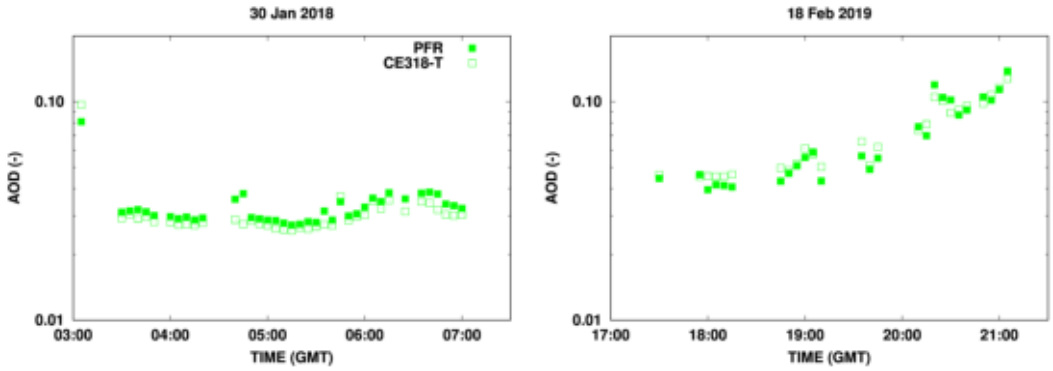

FIGURE 5.7: Comparison of lunar AOD measurements between PFR and Cimel at Ny-Ålesund at the spectral channel 500 nm.

The slight discrepancy observed in second period could potentially be attributed to sub-optimal calibration of the PFR instrument.

	P25	P50	P75	Mean	SD
30 Jan 2018					
PFR	0.038	0.040	0.042	0.042	0.010
Cimel	0.040	0.041	0.044	0.042	0.008
18 Feb 2019					
PFR	0.066	0.079	0.111	0.088	0.025
Cimel	0.064	0.074	0.113	0.088	0.029

TABLE 5.4: AOD 500nm statistics for both PFR and Cimel instruments for the comparison at Ny-Ålesund. P25, P50, and P75 are percentiles; SD = standard deviation.

Correlation analysis was also conducted between the AOD measurements obtained by the two instruments at all the available wavelengths. The Pearson correlation coefficients at 500 nm was 0.97 for both periods. Additionally, at 675 nm, the coefficients were 0.97 on January 30, 2018, and 0.98 on February 18, 2019. Even when the wavelengths slightly differed between the two instruments, i.e., 412 and 862 nm for PFR and 440 and 870 nm for Cimel, the correlation coefficient values remained consistently high (>0.95).

This analysis, although conducted over only few hours of measurement, highlights that the modified PFR has proven to have similar performance of the Cimel.

5.5 Conclusions

Two commercial sun photometers have been modified to be able to detect the very week spectral signals coming from the Moon during the period from first to third quarter. They have been used at two stations in the Artic during different periods, spanning the years from 2012 to 2019. Using the exo-atmospheric model ROLO for the evaluation of the radiation reflected by the Moon, we evaluated the AOD at the 4 wavelengths of the two instruments, together with their uncertainties. These resulted only slightly higher than those obtainable with sun photometry, being in the range 0.006 – 0.030 for the all the channels of two instruments.

As expected the AOD values result noisier at low Moon illumination, while more stable moving toward full Moon.

The AOD and alpha values evaluated at the two sites are in accordance with those reported in the literature for the periods of the year nearby the polar night when sun photometry is possible (e.g. October/March).

The comparison with star photometry data in Ny-Ålesund confirmed the reliability of the AOD values. More, the presence since 2017 of a commercial Cimel-318T allowed a direct comparison of the results, giving average differences of 0.006 at maximum, therefore lower than the evaluated uncertainties.

In this work we therefore demonstrated that lunar photometry is a suitable measurement technique also in polar regions, where AOD is very low and sunlight is not present for a long period during the year.

Bibliography

Barreto, A., Cuevas, E., Damiri, B., Guirado, C., Berkoff, T., Berjón, A. J., HernÁndez, Y., Almansa, F., and Gil, M. (2013a). A new method for nocturnal aerosol measurements with a lunar photometer prototype. *Atmospheric Measurement Techniques*, 6(3):585–598. Publisher: Copernicus GmbH.

Barreto, A., Cuevas, E., Damiri, B., Romero, P. M., and Almansa, F. (2013b). Column water vapor determination in night period with a lunar photometer prototype. *Atmospheric Measurement Techniques*, 6(8):2159–2167. Publisher: Copernicus GmbH.

Barreto, Á., Cuevas, E., Granados-Muñoz, M.-J., Alados-Arboledas, L., Romero, P. M., Gröbner, J., Kouremeti, N., Almansa, A. F., Stone, T., Toledano, C., RomÁn, R., Sorokin, M., Holben, B., Canini, M., and Yela, M. (2016). The new sun-sky-lunar Cimel CE318-T multiband photometer – a comprehensive performance evaluation. *Atmospheric Measurement Techniques*, 9(2):631–654. Publisher: Copernicus GmbH.

Barreto, A., Román, R., Cuevas, E., Berjón, A. J., Almansa, A. F., Toledano, C., González, R., Hernández, Y., Blarel, L., Goloub, P., Guirado, C., and Yela, M. (2017). Assessment of nocturnal aerosol optical depth from lunar photometry at the izaña high mountain observatory. *Atmospheric Measurement Techniques*, 10(8):3007–3019.

Barreto, A., RomÁn, R., Cuevas, E., Pérez-Ramírez, D., Berjón, A. J., Kouremeti, N., Kazadzis, S., Gröbner, J., Mazzola, M., Toledano, C., Benavent-Oltra, J. A., Doppler, L., Juryšek, J., Almansa, A. F., Victori, S., Maupin, F., Guirado-Fuentes, C., GonzÁlez, R., Vitale, V., Goloub, P., Blarel, L., Alados-Arboledas, L., Woolliams, E., Taylor, S., Antuña, J. C., and Yela, M. (2019). Evaluation of nighttime aerosols measurements and lunar irradiance models in the frame of the first multi-instrument nocturnal intercomparison campaign. *Atmospheric Environment*, 202:190–211.

Berkoff, T. A., Sorokin, M., Stone, T., Eck, T. F., Hoff, R., Welton, E., and Holben, B. (2011). Nocturnal Aerosol Optical Depth Measurements with a Small-Aperture Automated Photometer Using the Moon as a Light Source. *Journal of Atmospheric and Oceanic Technology*, 28(10):1297–1306. Publisher: American Meteorological Society Section: Journal of Atmospheric and Oceanic Technology.

Brunamonti, S., Martucci, G., Romanens, G., Poltera, Y., Wienhold, F. G., Hervo, M., Haefele, A., and Navas-Guzmán, F. (2021). Validation of aerosol backscatter profiles from raman lidar and ceilometer using balloon-borne measurements. *Atmospheric Chemistry and Physics*, 21(3):2267–2285.

Esposito, F., Mari, S., Pavese, G., and Serio, C. (2003). Diurnal and Nocturnal Measurements of Aerosol Optical Depth at a Desert Site in Namibia. *Aerosol Science and Technology*, 37(4):392–400. Publisher: Taylor & Francis _eprint: https://doi.org/10.1080/02786820300972.

Esposito, F., Serio, C., Pavese, G., Auriemma, G., and Satriano, C. (1998). Measurements of nighttime atmospheric optical depth preliminary data from a mountain site in southern Italy. *Journal of Aerosol Science*, 29(10):1213–1218.

Harrison, L. and Michalsky, J. (1994). Objective algorithms for the retrieval of optical depths from ground-based measurements. *Applied Optics*, 33(22):5126–5132.

Herber, A., Thomason, L. W., Gernandt, H., Leiterer, U., Nagel, D., Schulz, K.-H., Kaptur, J., Albrecht, T., and Notholt, J. (2002). Continuous day and night aerosol optical depth observations in the Arctic between 1991 and 1999. *Journal of Geophysical Research: Atmospheres*, 107(D10):AAC 6–1–AAC 6–13. _eprint: https://onlinelibrary.wiley.com/doi/pdf/10.1029/2001JD000536.

Herrero del Barrio, C., Mateos, D., RomÁn, R., GonzÁlez, R., Herrero-Anta, S., GonzÁlez-FernÁndez, D., Calle, A., Toledano, C., Cachorro, V. E., and De Frutos Baraja, Á. M. (2023). Analysis of daytime and night-time aerosol optical depth from solar and lunar photometry in valladolid (spain). *Remote Sensing*, 15(22).

Hoffmann, A., Ritter, C., Stock, M., Maturilli, M., Eckhardt, S., Herber, A., and Neuber, R. (2010). Lidar measurements of the Kasatochi aerosol plume in August and September 2008 in Ny-Ålesund, Spitsbergen. *Journal of Geophysical Research: Atmospheres*, 115(D2). _eprint: https://onlinelibrary.wiley.com/doi/pdf/10.1029/2009JD013039.

IPCC (2023). *Climate Change 2023: Synthesis Report. Contribution of Working Groups I, II and III to the Sixth Assessment Report of the Intergovernmental Panel on Climate Change*. IPCC, Geneva, Switzerland.

Kaufman, Y. J. and Joseph, J. H. (1982). Determination of surface albedos and aerosol extinction characteristics from satellite imagery. *Journal of Geophysical Research: Oceans*, 87(C2):1287–1299.

Kieffer, H. H. and Stone, T. C. (2005). The Spectral Irradiance of the Moon. *The Astronomical Journal*, 129(6):2887. Publisher: IOP Publishing.

Lubin, D. and Vogelmann, A. M. (2006). A climatologically significant aerosol longwave indirect effect in the Arctic. *Nature*, 439(7075):453–456. Number: 7075 Publisher: Nature Publishing Group.

Mazzola, M., Lanconelli, C., Lupi, A., Busetto, M., Vitale, V., and Tomasi, C. (2010). Columnar aerosol optical properties in the Po Valley, Italy, from MFRSR data. *Journal of Geophysical Research: Atmospheres*, 115(D17). _eprint: https://onlinelibrary.wiley.com/doi/pdf/10.1029/2009JD013310.

Perrone, M. R., Lorusso, A., and Romano, S. (2022). Diurnal and nocturnal aerosol properties by aeronet sun-sky-lunar photometer measurements along four years. *Atmospheric Research*, 265:105889.

Pérez-Ramírez, D., Aceituno, J., Ruiz, B., Olmo, F. J., and Alados-Arboledas, L. (2008). Development and calibration of a star photometer to measure the aerosol optical depth: Smoke observations at a high mountain site. *Atmospheric Environment*, 42(11):2733–2738.

Román, R., González, R., Toledano, C., Barreto, A., Pérez-Ramírez, D., Benavent-Oltra, J. A., Olmo, F. J., Cachorro, V. E., Alados-Arboledas, L., and de Frutos, A. M. (2020). Correction of a lunar-irradiance model for aerosol optical depth retrieval and comparison with a star photometer. *Atmospheric Measurement Techniques*, 13(11):6293–6310.

Sakerin, S. M., Kabanov, D. M., Radionov, V. F., Chernov, D. G., Turchinovich, Y. S., Lubo-Lesnichenko, K. E., and Prakhov, A. N. (2018). Generalization of results of atmospheric aerosol optical depth measurements on spitsbergen archipelago in 2011–2016. *Atmos Ocean Opt*, 31:163–170.

Shaw, G. E. (1983). Sun photometry. *Bulletin of the American Meteorological Society*, 64(1):4–10.

Stone, R., Sharma, S., Herber, A., Eleftheriadis, K., and Nelson, D. (2014). A characterization of Arctic aerosols on the basis of aerosol optical depth and black carbon measurements. *Elementa: Science of the Anthropocene*, 2.

Toledano, C., Cachorro, V., Gausa, M., Stebel, K., Aaltonen, V., Berjón, A., Ortiz de Galisteo, J., de Frutos, A., Bennouna, Y., Blindheim, S., Myhre, C., Zibordi, G., Wehrli, C., Kratzer, S., Hakansson, B., Carlund, T., de Leeuw, G., Herber, A., and Torres, B. (2012). Overview of sun photometer measurements of aerosol properties in scandinavia and svalbard. *Atmospheric Environment*, 52:18–28. Physical, chemical, optical and radiative properties of polar aerosols – IPY 2007 - 2008.

Tomasi, C., Lupi, A., Mazzola, M., Stone, R. S., Dutton, E. G., Herber, A., Radionov, V. F., Holben, B. N., Sorokin, M. G., Sakerin, S. M., Terpugova, S. A., Sobolewski, P. S., Lanconelli, C., Petkov, B. H., Busetto, M., and Vitale, V. (2012). An update on polar aerosol optical properties using POLAR-AOD and other measurements performed during the International Polar Year. *Atmospheric Environment*, 52:29–47.

Uchiyama, A., Shiobara, M., Kobayashi, H., Matsunaga, T., Yamazaki, A., Inei, K., Kawai, K., and Watanabe, Y. (2019). Nocturnal aerosol optical depth measurements with modified sky radiometer POM-02 using the moon as a light source. *Atmospheric Measurement Techniques*, 12(12):6465–6488. Publisher: Copernicus GmbH.

Zhao, X., Huang, K., Fu, J. S., and Abdullaev, S. F. (2022). Long-range transport of asian dust to the arctic: identification of transport pathways, evolution of aerosol optical properties, and impact assessment on surface albedo changes. *Atmospheric Chemistry and Physics*, 22(15):10389–10407.

Zhou, M., Wang, J., Chen, X., Xu, X., Colarco, P. R., Miller, S. D., Reid, J. S., Kondragunta, S., Giles, D. M., and Holben, B. (2021). Nighttime smoke aerosol

optical depth over u.s. rural areas: First retrieval from viirs moonlight observations. *Remote Sensing of Environment*, 267:112717.

Chapter 6

Recent Advances in Aerosol Optical Depth Measurements in Polar Regions: Insights from the Polar-AOD Program

In this final research paper, we expanded the study to cover the entire Polar regions by collecting the highest-quality solar, lunar, and stellar photometric measurements from permanent research stations, using a variety of instruments (e.g., PFR, CIMEL, PREDE). The paper provides a comprehensive analysis of aerosol optical depth (AOD) and the Ångström exponent (α) at 15 Arctic and 11 Antarctic stations, updating and extending previous multi-year ground-based aerosol climatologies. The analysis examines seasonal variability, long-term trends, and differences between Arctic and Antarctic environments. Results show persistent winter haze in the Arctic, a decreasing AOD trend likely due to reduced anthropogenic emissions, and seasonal aerosol patterns in Antarctica dominated by natural sources. These findings improve understanding of aerosol variability and long-term trends in polar regions and support year-round monitoring and open-access data initiatives.

Published as:

PULIMENO S., Lupi A., Vitale V., Frangipani C., Toledano C., Kazadzis S., Kouremeti N., Ritter C., Graßl S., Stebel K., Fioletov V., Abboud I., Blindheim S., Ma L., O'Neill N., Sobolewski P., Gupta P., Lind E., Eck T.F., Hyvärinen A., Aaltonen V., Kivi R., Csavina J., Kabanov D., Sakerin S.M., Sidorova O.R., Stone R.S., Telg H., Riihimaki L., Cordero R.R., Radenz M., Engelmann R., Van Roozenda M., Chaikovsky A., Goloub P., Hisamitsu J., and Mazzola M., 2024, *Recent Advances in Aerosol Optical Depth Measurements in Polar Regions: Insights from the Polar-AOD Program*

6.1 Abstract

A multi-year analysis of aerosol optical depth (AOD, τ) and Ångström exponent (α) was conducted using ground-based photometer data from 15 Arctic and 11 Antarctic sites. Extending the dataset of Tomasi et al. 2015 through December 2024, the study incorporates stellar and lunar photometric observations to fill data gaps during the polar night. Daily mean values of τ at 0.500 μm and α (0.440–0.870 μm) were used to derive monthly means and seasonal histograms.

In the Arctic, persistent haze events in winter and early spring lead to peak τ values. A decreasing trend in Arctic τ suggests the impact of European emission regulations, while biomass-burning aerosols are becoming more significant. In Antarctica, τ increases from the plateau to the coast. Fine-mode aerosols dominate in summer-autumn, while coarse-mode particles are more prevalent in winter-spring. Shipborne photometer data align well with ground-based measurements, confirming the reliability of mobile observations.

Trend analyses using the Mann-Kendall test and Theil-Sen regression indicate a significant negative trend in τ at Andenes (-2.43% per year), likely driven by reduced anthropogenic emissions. Antarctic stations such as Syowa and South Pole show positive trends ($+3.84\%$ and $+3.54\%$ per year), though these are subject to uncertainties from data limitations and instrument changes.

This work contributes to the Polar-AOD network (`https://polaraod.net/`; last access 15/05/2025), enhancing the understanding of aerosol variability and long-term trends in polar regions while promoting open data access for the scientific community.

6.2 Introduction

Atmospheric aerosols play a crucial role in the Earth's atmosphere and represent some of its most dynamic components. Since the pre-industrial era, anthropogenic activities have significantly increased the concentration of atmospheric aerosols, particularly sulfate and carbonaceous aerosols. This rise has influenced the absorption and scattering of incoming solar radiation, thereby affecting both the microphysical and macrophysical properties of clouds, as well as their radiative properties. Although there is a high degree of uncertainty regarding the role of aerosols in the climate system, they are mostly associated with a negative feedback mechanism, i.e. aerosols interact with solar radiation, resulting in a net cooling effect (Intergovernmental Panel on Climate Change (IPCC) 2023).

The Arctic atmosphere is highly stratified, with frequent inversions near the surface. This stability reduces turbulence and dry deposition at the surface. Surfaces of constant potential temperature form a dome over the Arctic, creating a transport barrier that isolates this environment from the rest of the atmosphere (Klonecki et al. 2003). When addressing pollution levels in the Arctic, it is important to consider the variation in pollution transport due to the North Atlantic Oscillation (NAO). During the positive phases of the NAO, transport patterns from the northern mid-latitude continents (Europe, North America, and Asia) are significantly enhanced (Stohl 2006). The Arctic Haze phenomenon significantly impact the Arctic region. Since the 1950s, pilots have documented a reduction in visibility due to the presence of haze (Raatz et al. 1985). Scientists debated the origin of the haze until the 1970s, when it was proposed that Arctic haze originated not only from natural sources (Warneke et al. 2009) but also from anthropogenic emissions in the northern mid-latitudes. During winter, the expansion of the Polar dome (down to 40° N) facilitates the intrusion and

the transport of pollutants into the Arctic atmosphere over thousands of kilometers. The inefficiency of removal mechanisms during winter and early spring contributes to the seasonality of this phenomenon (Shaw 1995).

Polar aerosols originate from both natural and anthropogenic sources. In the Arctic region, the majority of the aerosol mass fraction consists of oceanic sea-salt, mineral dust, non-sea-salt sulfate, and biomass burning combustion products (Tomasi et al. 2015). Conversely, anthropogenic aerosols have a different composition, characterized by high concentrations of black carbon (BC), sulfates, and nitrates, which are typical signatures of traffic and industrial emissions (Quinn et al. 2007; Sharma et al. 2006).

In the Southern Hemisphere, the atmosphere is stably stratified much like in the Arctic, though katabatic winds carry air from the interior plateau to the coasts. Key transport processes in this region are similar to those in the Arctic and include: (i) lifting at the Antarctic front, (ii) lifting at lower latitudes, and (iii) descent due to radiative cooling of upper-tropospheric air masses (Tomasi et al. 2007). In Antarctica, aerosols at coastal sites are almost totally from natural processes, with high percentages of sea-salt mass content, non-sea-salt sulphate, and mineral dust (Tomasi et al. 2012). In this region, only a small fraction of the total aerosol mass is of anthropogenic origin, such as nitrates and BC (Cordero et al. 2022). Significant aerosol sources in both the Arctic and Antarctic regions include commercial ships, primarily operating in the Northern Hemisphere along the Northern Sea Route and the Transpolar Sea Route, and cruise ships mainly in Antarctica. Additionally, diesel generators used for energy production, aircraft emissions, and access to strategic resources (such as ore and oil) can also be considered as important sources of pollution at both poles.

The aim of this paper is to update the aerosol climatologies at both poles, developing the work published by Tomasi et al. 2015. This study was limited by the technology available at the time, relying solely on the solar photometry technique. This posed a significant limitation for scientists working in polar regions, where the Sun is absent for several months during the polar night. For example, at the Arctic station of Ny-Ålesund (Svalbard, Norway), the Sun remains below 5° of elevation from October 10th to March 4th, severely restricting the period available for conventional photometric measurements. To overcome this challenge, Lidar instruments can be used, as they provide aerosol extinction profiles even at night, which can then be converted to optical depth for comparison with photometric data. However, there are too few Lidar systems in polar regions to provide a comprehensive image of these environments. The lunar photometry technique, which has developed over the last decade, has proven to be a suitable technique in polar areas, where τ values are often below 0.05 (Mazzola et al. 2024). To address this issue and fill historical gaps in τ climatology, it has been proposed to use solar and lunar photometry techniques in synergy. AERONET stations at both poles with measurements up to December 2024, have been selected for this work (AERONET: `https://aeronet.gsfc.nasa.gov/`; last access 15/05/2025).

The paper is organized as follows. In the next section, a description of the main characteristics of both solar and lunar photometry techniques is provided. Section 6.4 presents the main optical characteristics of polar aerosols in the Arctic region, while Section 6.5 focuses on measurements in Antarctica.

6.3 Ground-based remote sensing measurements

Remote sensing ground-based techniques are commonly used to study the characteristics of the atmospheric column. Specifically, photometry has proven to be effective

also in polar areas, where background values are smaller compared to continental areas due to a cleaner atmosphere (Mazzola et al. 2012).

A sun-photometer is an instrument that is kept oriented towards the Sun to detect solar radiation attenuated by particles in the atmospheric column along the slant path from the top of the atmosphere (TOA) to the ground. The more particles present in the atmospheric column, the more attenuated the direct solar radiation detected by the photometer will be. This attenuation depends on the aerosol optical depth (AOD), represented by the symbol $\tau_{(\lambda)}$, which is the integral of the volume aerosol extinction coefficient along the vertical path of the atmosphere (Tomasi et al. 2015).

In recent decades, several sun-photometer models have been developed and implemented in major photometry networks worldwide. The most important of these networks are: (i) AERONET (AErosol RObotic NETwork), established by NASA, which has provided long-term measurements for over 25 years with standardized calibration, processing, and distribution processes (Holben et al. 1998); (ii) SKYNET, initiated under the WCRP/GAME, which evaluates long-term variations in aerosol concentrations and is mainly distributed in Asia (Nakajima et al. 2020); (iii) GAW-PFR, an international network that measures AOD at GAW stations (Kazadzis et al. 2018).

We focused primarily on AERONET sites in both the Arctic and Antarctica, as this network provides highly accurate AOD measurements (accuracy of 0.01 for the visible and NIR wavelengths at optical airmass of 1) and has the widest coverage at the poles. The high latitudes of these sites result in large airmass values, typically in the range of 2 to 7. This leads to a reduction in AOD calibration uncertainty by a factor of $1/m$, where m is the airmass (Eck et al. 1999). In 2018, the latest AERONET Version 3 (V3) algorithm was published, featuring a fully automatic cloud screening procedure and instrument anomaly controls (Giles et al. 2019). AERONET includes a component dedicated to ship-borne AOD measurements using the manual sun photometer Microtops II. Since 2004, this instrument has been routinely deployed on research vessels to monitor aerosol properties over the oceans. The Maritime Aerosol Network (MAN) enables the study and evaluation of aerosol properties across various oceanic regions, including polar sectors.

In addition to CIMEL CE318 data from AERONET, other international research groups provided AOD measurements obtained using various photometer models, including the SPM multiwavelength sun photometer and its simplified version the SP-9 (Sakerin et al. 2013); the Carter-Scott Design Middleton SP02 sun photometer (McArthur 2005); the SP1A developed by Dr. Schults and Partner GmbH (Stock et al. 2014); the Precision Filter Radiometer (PFR) (Wehrli 2000); and the MS110 sun photometer (Kim et al. 2005).

6.3.1 Solar photometry

The fundamental equation used in sun-photometry to retrieve AOD is the Lambert-Beer law (Shaw 1976). Specifically, this equation is applied to the raw signal at a given wavelength λ ($V_{(\lambda)}$) measured by the instrument at ground level, and to the signal the photometer would detect at the TOA ($V_{0(\lambda)}$):

$$V_\lambda = \frac{V_{0,\lambda}}{R^2} e^{-\tau_{TOD,\lambda} m} \tag{6.1}$$

where R represents the Earth-Sun distance in AU, m is the optical air mass that indicates the relation between extinction in the vertical column and that in the measurements slant path (which is related to the zenith angle of the target) and $\tau_{TOD,\lambda}$ is the total optical depth (TOD).

In order to obtain reliable values of $V_{0,\lambda}$ at a given wavelength, the Langley plot method can be applied (Shaw 1983). This method involves applying a linear regression between the logarithm of the signals measured by the instrument ($\ln V_\lambda$) and the calculated values of air masses (m). The intercept of this line represents the value of $V_{0,\lambda}$ at the TOA, and the slope represents the $\tau_{TOD,\lambda}$. Only the signals measured at different spectral channels within an air mass range usually between 2 and 5 are considered. Values of $m<2$ are not used because the rate of change of air mass is very small, with a higher likelihood that changing weather conditions will influence the regression. Conversely, values of $m>5$ are discarded due to greater uncertainty in the value of m itself caused by corrections due to the phenomenon of refraction. To avoid errors in corrections at high solar zenith angles, the range normally used in the Langley plot method is m between 2 and 5 (Alexandrov et al. 2004; Mazzola et al. 2010).

In the term $\tau_{TOD,\lambda}$, the contribution due to scattering and absorption by gases is included, so that Eq.(6.1) can be rewritten in logarithmic form as:

$$\ln V_\lambda = \ln(V_{0,\lambda} R^{-2}) - (\tau_{a,\lambda} m_a + \tau_{R,\lambda} m_R + \tau_{g,\lambda} m_g) \tag{6.2}$$

The subscript 'a' stands for aerosol, 'R' for Rayleigh scattering by molecules, and 'g' for absorption gases. At this point, the AOD can de directly derived by Eq.(6.2) as:

$$\tau_{a,\lambda} = -\frac{1}{m_a}\left[\ln\left(\frac{V_\lambda}{V_{0,\lambda} R^2}\right) - \tau_{R,\lambda} m_R - \tau_{g,\lambda} m_g\right] \tag{6.3}$$

Since the vertical distribution is different for any gas, several air mass factors are taken into account; for example, ozone is mainly stratospheric, while carbon dioxide is uniformly mixed (González et al. 2020). The gaseous species considered in the term $\tau_{g,\lambda} m_g$ of Eq.(6.3) are ozone O_3, nitrogen dioxide NO_2, water H_2O, carbon dioxide CO_2, and methane CH_4.

Another important parameter that can be estimated from τ_λ measurements is the Ångström exponent (α) calculated as follows:

$$\alpha = -\frac{log\left(\frac{\tau_{\lambda_1}}{\tau_{\lambda_2}}\right)}{log\left(\frac{\lambda_1}{\lambda_2}\right)} \tag{6.4}$$

where τ_{λ_1} and τ_{λ_2} are the AOD values at the wavelengths λ_1 and λ_2, usually 0.440 and 0.870 μm. This parameter quantifies the wavelength dependence of AOD, providing insight into the size distribution of atmospheric particles (Kaskaoutis et al. 2007).

While τ_λ provides information about the extinction caused by the presence of aerosol particles along the vertical atmospheric path, α reflects the contributions of different particle sizes to this extinction. Values of α greater than 1.3 are typically associated with a predominance of very fine particles, whereas values of α less than 1.0 indicate the presence of particles in accumulation and coarse mode, which produce a larger extinction effect (Iqbal 1983). Additionally, the α value in the 0.440-0.870 μm range is dominated by the coarse mode (Eck et al. 2010).

6.3.2 Lunar photometry

In the last decades, many attempts have been made to use the Moon as a light source to retrieve aerosol properties. The stability of the lunar surface reflectance makes the Moon a nearly perfect calibration source. However, there are significant challenges due to the non-uniformity of the lunar surface albedo resulting from the presence of lunar maria and highlands, the brightness variation arising from lunar phase and libration, the strong dependence of surface reflectivity on phase angle, and the fact that cloud cover can block or reduce the Moon's irradiance. The complexity of these dependencies effectively mandates the use of a lunar radiometric model to compare against spacecraft observations of the Moon. The USGS in Flagstaff (Arizona, US) has acquired the observational data and proposed the RObotic Lunar Observatory (ROLO) model (Kieffer and Stone 2005). This model can provide the exoatmospheric lunar irradiance for any given location and time. The model is based on fitting thousands of lunar measurements acquired over more than 8 years with the ground-based ROLO telescopes in 32 wavelength bands from 0.350 to 2.450 μm. The ROLO model uses an empirically derived analytic equation to predict the lunar disk-equivalent reflectance (A_k) in the spectral band k using only geometric variables (Kieffer and Stone 2005):

$$lnA_k = \sum_{i=0}^{3} a_{ik} g^i + \sum_{j=1}^{3} b_{jk} \Phi^{2j-1} + c_1\phi + c_2\theta + c_3\Phi\phi + c_4\Phi\theta + \tag{6.5}$$

$$d_{1k} e^{-g/p_1} + d_{2k} e^{-g/p_2} + d_{3k} cos((g - p_3)/p_4) \tag{6.6}$$

Where g is the absolute phase angle, θ and ϕ are the selenographic latitude and longitude of the observer, and Φ is the selenographic longitude of the Sun. The ROLO model provides exo-atmospheric lunar irradiance with relatively high precision. The band-average absolute residuals are about 1%, based on comparisons between ROLO empirical irradiances and hundreds of ROLO observations. This high precision makes the ROLO model a valuable tool for calibrating measurements and interpreting data for aerosol property retrievals. As always, for the retrieve of AOD during nighttime, the Beer-Lambert law can be used:

$$V_\lambda = V_{0,\lambda} e^{-m(\theta)\tau_\lambda} \tag{6.7}$$

Where V_λ is the output voltage, $V_{0,\lambda}$ the extraterrestrial voltage which include lunar phase variations as well as Earth-Moon and Moon-Sun distances, m is the relative optical air mass (and function of the moon zenith angle θ), and τ_λ the spectral optical depth. To account for the change in lunar illumination during the course of the night, and for the distant effect on lunar irradiance, the V_0 term of Eq.(6.7) can be modified as:

$$V_{0,j} = I_{0,j} k_j \tag{6.8}$$

Where $I_{0,j}$ is the extraterrestrial irradiance in a certain channel with a central wavelength at j, and k_j is a constant that depends on the instrument features such as the calibration coefficient and the instrument's solid angle-of-view. $I_{0,j}$ is calculated using the ROLO lunar disk-equivalent reflectances (A_k) in Eq.(6.5). The exact formula can be found in Barreto et al. 2013. In the same paper, authots proposed the Lunar-Langley Method for the calibration of the instrument. Basically, the logarithmic form of Eq.(6.7) and Eq.(6.8), together with a least square fitting procedure are used to obtain the instrument's calibration constant (k_j) as the intercept of the fitting line.

Once these constants are known, it is possible to retrieve AOD from an individual measurement:

$$\tau_{a,j} = \frac{\ln k_j - \ln\left(\frac{V_j}{I_{0,j}}\right) - m_{atm}(\theta)\tau_{atm,j}}{m_{a(\theta)}} \tag{6.9}$$

The subscript 'atm' accounts for air mass and optical depth of each atmospheric attenuator with the exception of aerosols. Román et al. 2020, proposed the use of the RIMO (ROLO Implementation for Moon's Observation) model to retrieve AOD during night-time, based on the assumption that the calibration constants for solar channels can be transferred to the Moon. Because authors found an underestimation of AODs retrieved by using this model (dependent on the optical air mass), they proposed a correction factor that, multiplied by the RIMO value, gives a more accurate extraterrestrial lunar irradiance that can be used for a more accurate retrieval of AODs during night.

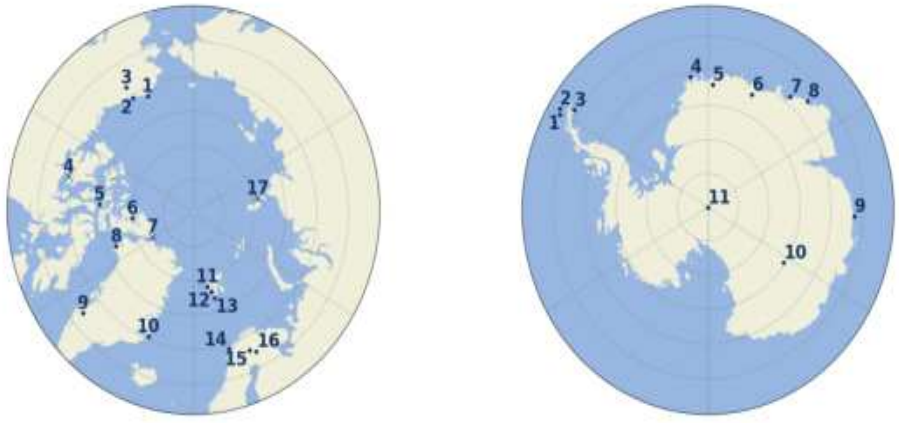

(A) (B)

FIGURE 6.1: Part (A) map of the Arctic showing the geographical position of the stations labeled as follows: (1) Barrow, (2) Oliktok, (3) Toolik Lake, (4) Cambridge Bay, (5) Resolute Bay, (6) Eureka (OPAL), (7) Alert, (8) Thule, (9) Kangerlussuaq, (10) Ittoqqortoormiit, (11) Ny-Ålesund, (12) Barentsburg, (13) Hornsund, (14) Andenes, (15) Matorova, (16) Sodankylä, and (17) Cape Baranova. Part (B) presents a map for the Antarctic stations, with the locations marked as: (1) Juan Carlos I, (2) Escudero, (3) Marambio, (4) Neumayer, (5) Troll/Trollhaugen, (6) Utsteinen, (7) Syowa, (8) Vechernaya Hill, (9) Mirny, (10) DomeC and (11) South Pole. Stations marked with 'X' have been studied but not shown in this paper.

Stations - ID	Managing Institutions	Instrument model	Coordinates and Altitude	Measurement Period	Lunar Data started
Arctic sites					

Continued on next page

Arctic sites (continued)

Stations - ID	Managing Institutions	Instrument model	Coordinates and Altitude	Measurement Period	Lunar Data started
Alert (Canada) - 7	Environment and Climate Change Canada, Canada	CE318	82.4501 N, 62.5074 W, 210 m a.m.s.l.	March 2024 - November 2024 [11,641]	October 2024 - November 2024 [811]
Andenes (Norway) - 14	Andøya Rocket Range, Norway - University of Valladolid, Spain	CE318	69.2783 N, 16.0086 E, 379 m a.m.s.l.	February 2002 - December 2023 [55,719]	December 2016 [8,046]
Barentsburg (Norway) - 12	Arctic and Antarctic Research Institute - Zuev Institute of Atmospheric Optics, Russia	SPM and SP-9	78.0590 N, 14.2192 E, 7 m a.m.s.l.	March 2011 - August 2023 [605]	no
Barrow (US) - 1	Atmospheric Radiation Measurements (ARM), US	CE318	71.3226 N, 156.6151 W, 8 m a.m.s.l.	July 1997 - December 2023 [41,003]	October 2018 [2,011]
Barrow (US) - 1	NOAA, US	SP02	71.1926 N, 156.3615 W, 8 m a.m.s.l.	March 2001 - October 2016 [1,764]	no
Cambridge Bay (Canada) - 4	Environment and Climate Change Canada, Canada - University of Sherbrook, Canada	CE318	69.1213 N, 105.0394 W, 5 m a.m.s.l.	September 2024 - October 2024 [110]	September 2024 [16]
Cape Baranova (Russia) - 17	Zuev Institute of Atmospheric Optics, Russia	SPM	79.1682 N, 101.3705 E, 20 m a.m.s.l.	April 2018 - August 2021 [59]	no
Eureka OPAL (Canada) - 6	Environment and Climate Change Canada, Canada	CE318	79.9902 N, 85.9391 W, 5 m a.m.s.l.	April 2007 - December 2024 [95,421]	April 2016 [6,044]
Hornsund (Norway) - 13	Polish Academy of Sciences, Poland	CE318	77.0014 N, 15.5402 E, 12 m a.m.s.l.	May 2004 - December 2023 [30,382]	October 2021 [113]
Ittoqqortoormiit (Green-land) - 10	NASA Goddard Space Flight Center, US	CE318	70.4848 N, 21.9512 W, 68 m a.m.s.l.	October 2009 - November 2022 [38,943]	September 2020 [667]

Continued on next page

Arctic sites (continued)

Stations - ID	Managing Institutions	Instrument model	Coordinates and Altitude	Measurement Period	Lunar Data started
Kangerlussuaq (Greenland) - 9	NASA Goddard Space Flight Center, US	CE318	66.9958 N, 50.6214 W, 320 m a.m.s.l.	April 2008 - December 2023 [68,634]	March 2017 [6,826]
Matorova (Finland) - 15	Finnish Meteorological Institute, Finland	CE318	67.9999 N, 24.2400 E, 340 m a.m.s.l.	September 2020 - September 2024 [32,116]	October 2020 [6,354]
Ny-Ålesund (Norway) - 11	Alfred Wegener Institute, Germany - University of Valladolid, Spain	CE318	78.9232 N, 11.9230 E, 7 m a.m.s.l.	June 2017 - December 2023 [26,426]	October 2017 [2,144]
Ny-Ålesund (Norway) - 11	Alfred Wegener Institute, Germany	SP1A	78.9233 N, 11.9292 E, 17 m a.m.s.l.	March 2012 - September 2023 [407,945]	no
Ny-Ålesund (Norway) - 11	Physical Meteorological Observatory Davos, Switzerland - NILU, Norway	PFR	78.9232 N, 11.9293 E, 15 m a.m.s.l.	May 2005 - September 2023 [588,041]	no
Oliktok (US) - 2	Atmospheric Radiation Measurement (ARM), US	CE318	70.4995 N, 149.8800 W, 2 m a.m.s.l.	September 2013 - June 2021 [20,193]	September 2018 [1,279]
Resolute Bay (Canada) - 5	Environment and Climate Change Canada, Canada - AEROCAN, Canada	CE318	74.7051 N, 94.9694 W, 35 m a.m.s.l.	July 2004 - December 2024 [28,391]	no
Sodankylä (Finland) - 16	Finnish Meteorological Institute, Finland	CE318	67.3666 N, 26.6295 E, 184 m a.m.s.l.	March 2013 - December 2023 [21,500]	November 2017 [4,062]
Thule (Greenland) - 8	NASA Goddard Space Flight Center, US	CE318	76.5145 N, 68.7431 W, 225 m a.m.s.l.	March 2007 - December 2023 [73,819]	May 2017 [3,744]
Toolik Lake (US) - 3	National Ecological Observatory Network, US	CE318	68.6610 N, 149.3704 W, 843 m a.m.s.l.	February 2017 - December 2023 [14,902]	no

TABLE 6.1: List of Arctic stations using different models of photometer. For each station, the coordinates and altitude are specified, along with the measurement period for solar photometry and the installation period for the lunar model. The number of measurements for both the solar and lunar periods is provided in parentheses.

Continued on next page

Arctic sites (continued)

Stations - ID	Managing Institutions	Instrument model	Coordinates and Altitude	Measurement Period	Lunar Data started

6.4 Measurements in the Arctic

To conduct an in-depth analysis of polar aerosol optical characteristics, sun- and moon-photometer measurements of τ across various spectral channels in the visible and near-infrared can be examined to evaluate the Ångström exponent α, as described by Eq. (6.4).

Table 6.1 presents information on the 15 Arctic sites analyzed in this paper, where direct radiation measurements were conducted under partly cloudy sky conditions over the past decades. The geographical locations of these sites are shown in Fig. 6.1a for the Arctic region.

Several international institutions provided high-quality measurements of τ and α using different photometer models. The specific wavelengths used by these photometers, along with details about calibration and cloud-screening procedures, are described singularly. For what concerns AERONET stations, level 2 data for solar photometry and level 1.5 data for lunar photometry have been used (as level 2 data for lunar photometry are not yet available on AERONET). Both datasets are of high quality, with a slight distinction: near-real-time level 1.5 data have been corrected for the presence of clouds during measurements, whereas level 2 data have undergone additional quality controls with pre- and post-calibration procedures applied (Giles et al. 2019). Furthermore, the cloud screening at night does not include lunar aureole data due to insufficient measurement signals and therefore the aureole radiance curvature test for this cirrus clouds could not be applied at night (Giles et al. 2019).

Since not only AERONET data but also measurements from several other photometers were used, the initial datasets were characterized by different time intervals. To account for these differences, individual measurements of τ_λ recorded under cloud-free sky conditions at each station were first averaged on an hourly basis. These hourly averaged values were then used to calculate multi-year monthly mean values of $\tau(0.500\mu\text{m})$ and α. When analyzing these parameters, it is important to remember that AOD data are not normally distributed, especially when episodic or extreme events occur. In such cases, the mean value can be heavily influenced by these episodes, as well as by the overall data availability for a specific day or month. For example, a month with two episodic high-AOD events will show a higher monthly mean if there are many cloudy days (resulting in fewer AOD measurements) compared to a month with more frequent clear-sky observations and the same number of episodic events. Additionally, since AOD measurements depend strongly on weather conditions, the data series are often discontinuous, with large gaps during periods of persistent cloud cover, polar night, or instrument downtime. These discontinuities must be carefully considered when interpreting long-term trends or variability.

We also defined relative frequency histograms for both parameters during the following seasons: winter (December to February), when intrusions of polluted particles into the Arctic atmosphere are more frequent; spring (March to May); summer (June to August), to characterize background aerosols; and autumn (September to November).

6.4.1 Northern America

Several multi-year sets of sun-photometer measurements have been collected from coastal stations on the Arctic Ocean, as well as from a more continental sites in Northern America.

At Barrow, the Atmospheric Radiation Measurement (ARM) program conducted observations using a CIMEL sun photometer from July 1997 to December 2024. In 2018, this instrument was replaced with a sun-sky-lunar CIMEL photometer, which also began providing lunar data starting in October 2018. Additionally, the National Oceanic and Atmospheric Administration (NOAA) studied aerosol extinction properties at the same site using a Carter Scott SP02 sun photometer from March 2001 to October 2016. The SP02 measured solar radiation at four spectral channels, centered at wavelengths of 0.412, 0.500, 0.675, and 0.862 μm. Consistent with AERONET stations, τ was analyzed at 0.500 μm, while the α was studied over the spectral range of 0.412–0.862 μm. At Barrow (Fig.6.2), the monthly mean values of $\tau(0.500\mu m)$ measured by the CIMEL increased from approximately 0.07 in February to 0.10 in July, before decreasing to 0.04 in October. The standard deviation (σ) of these measurements exceeded 0.17 in June and July but remained below 0.04 in other months. Regarding the α, Barrow exhibited typical Arctic site behavior. Specifically, α was lower during the winter and early spring, coinciding with the period of most intense Arctic haze and elevated atmospheric pollution; low α values can also result from the presence of wind-blown sea salt (O'Neill et al. 2016), or thin cirrus clouds. During the polar spring, coarse-mode Asian dust could be mistaken for Arctic haze (AboEl-Fetouh et al. 2020) in the absence of lidar measurements. Conversely, α was higher during the summer and autumn, when the atmosphere is generally cleaner, and the aerosol population is dominated by smaller particles. The mean α values recorded by the two instruments were similar. For winter-spring, α was 1.00 and 1.09, as measured by the CIMEL and SP02, respectively. For summer-autumn, α values were 1.45 for the CIMEL and 1.25 for the SP02. However, differences were observed in $\tau(0.500\mu m)$ during the summer months. The CIMEL (Fig.6.2a) showed higher mean values with greater variability compared to the SP02(Fig.6.2b). These differences can be attributed to the distinct time periods covered by the two instruments (see Table 6.1) and the occurrence of extreme wildfire events in North America and Siberia between 2019 and 2020 (Pulimeno et al. 2024, Engelmann et al. 2021, Ohneiser et al. 2021), which were only captured by AERONET with the CIMEL. Further evidence for the impact of wildfire smoke on the arctic aerosol composition was found at the Toolik Lake station by Welch et al. 2025.

At Oliktok, measurements spanned from September 2013 to June 2021, with lunar data measurements started in September 2018. Observations from Toolik Lake, taken from February 2017 to December 2024, do not include lunar data (see Table 6.1). Spectral $\tau(0.50\mu m)$ and α measurements for these stations are shown in Figure 6.3. Similar results from Barrow were observed at Oliktok station, where the monthly mean values of $\tau(0.50\mu m)$ increase from 0.05 in February to around 0.09 in July, then decrease until reaching 0.04 in November, with σ exceeding 0.08 in March, July, and August, and below 0.05 in other months. For the α, Barrow and Oliktok exhibit similar behavior; the monthly mean values of α at Oliktok varying from 0.90 in February to 1.60 in July, with σ equal to 0.35 on average.

At Toolik Lake station the monthly mean values of $\tau(0.50\mu m)$ exhibit a similar pattern to those observed at the other two stations, ranging from approximately 0.04 in February to 0.14 in July. The standard deviation σ was greater than 0.40 in July and less than 0.04 in the other months. In contrast, the α values were relatively

stable throughout the seasons with minor oscillations, ranging from 1.28 in winter to 1.66 in summer, with σ consistently below 0.40. Figure 6.3 also presents the Relative Frequency Histograms (RFH) of the daily mean values of $\tau(0.500\mu m)$ and α measured across all seasons. The RFHs for these stations were similar, although there were noticeable discrepancies between the means and percentiles. During winter, the seasonal mean values of $\tau(0.500\mu m)$ were 0.07 for Barrow and Oliktok, and 0.04 for Toolik Lake. In contrast, during the summer season, the mean values were 0.18, 0.13, and 0.18 for the same stations. Consistent with the findings of Tomasi et al. 2015, the RFHs exhibited long tails towards higher τ values in all seasons, with particularly pronounced tails in winter and summer. This feature observed during winter may be attributed to higher AOD values in March and April, a consequence of the Arctic Haze phenomenon. The summer long-tail feature can be explained by the positive trend in total AOD during June, July, and August (JJA), quantified as +0.007 AOD per decade by Xian et al. 2022. Their study demonstrated that during JJA, the smoke AOD contribution to the total AOD turns positive, with a +22% contribution per decade. This trend is visually evident in the multi-year monthly boxplots for June, July, and August shown in Figure 6.2 and 6.3 for all the North-American stations.

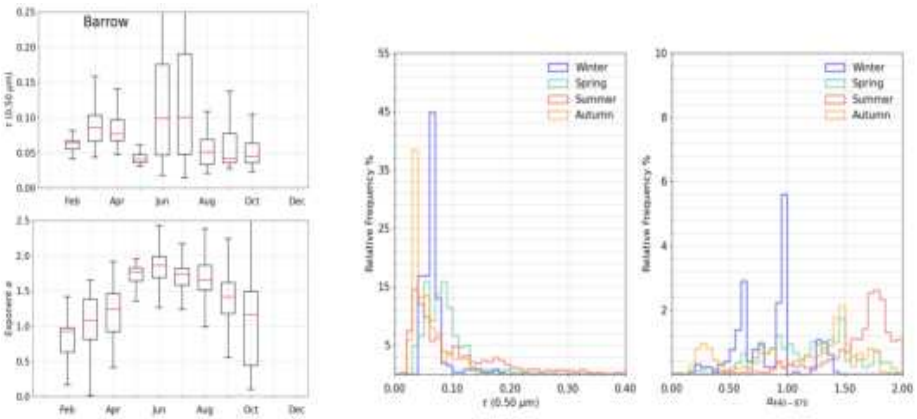

(A)

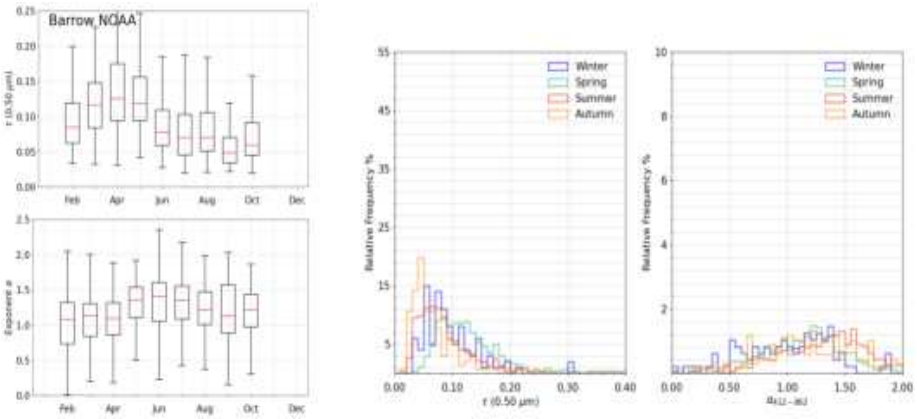

(B)

FIGURE 6.2: Left-hand side: Time-patterns of the monthly mean values and the first and third quartiles of aerosol optical thickness $\tau(0.500\mu m)$ and the Ångström exponent α. The whiskers extend from the box to the farthest data point within 1.5 times the interquartile range (IQR) from the box. Right-hand side: relative frequency histograms for $\tau(0.500\mu m)$ and α separately for winter (arctic haze, DJF), spring (MAM), summer (background, JJA), and autumn (SON). These statistics were obtained from multi-year sun-photometer measurements conducted at Barrow by (a) Atmospheric Radiation Measurements, and by (b) National Oceanic and Atmospheric Administration.

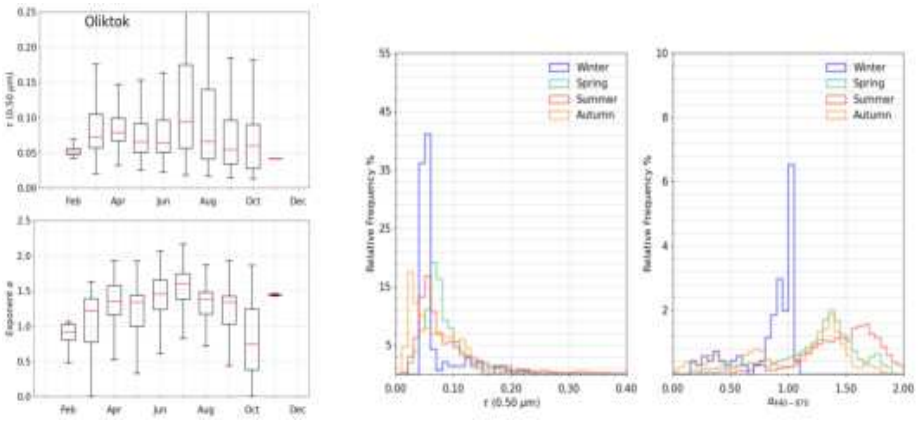

(A)

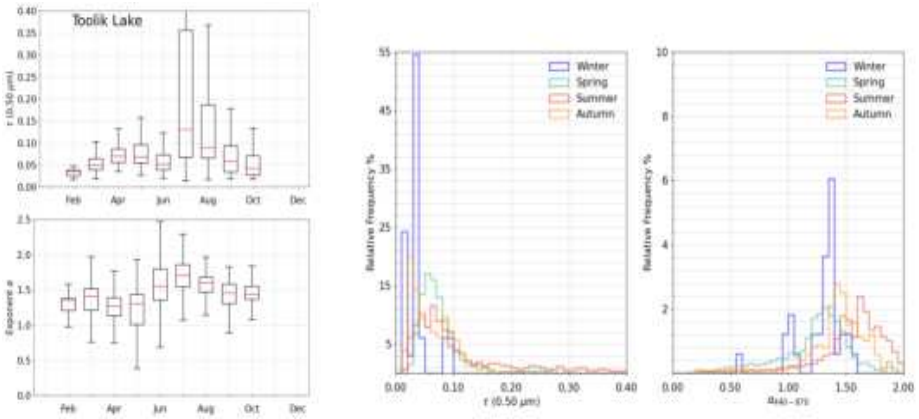

(B)

FIGURE 6.3: As in Fig.6.2, for the multi-year sun-photometer measurements of aerosol optical depth $\tau(0.500\mu m)$ and exponent α conducted at: (a) Oliktok by Atmospheric Radiation Measurements, and (b) Toolik Lake by National Ecological Observatory Network. To show the monthly boxplot of $\tau(0.50\mu m)$, the y-axis scale for the Toolik Lake station has been adjusted to range from 0 to 0.40.

6.4.2 Canada

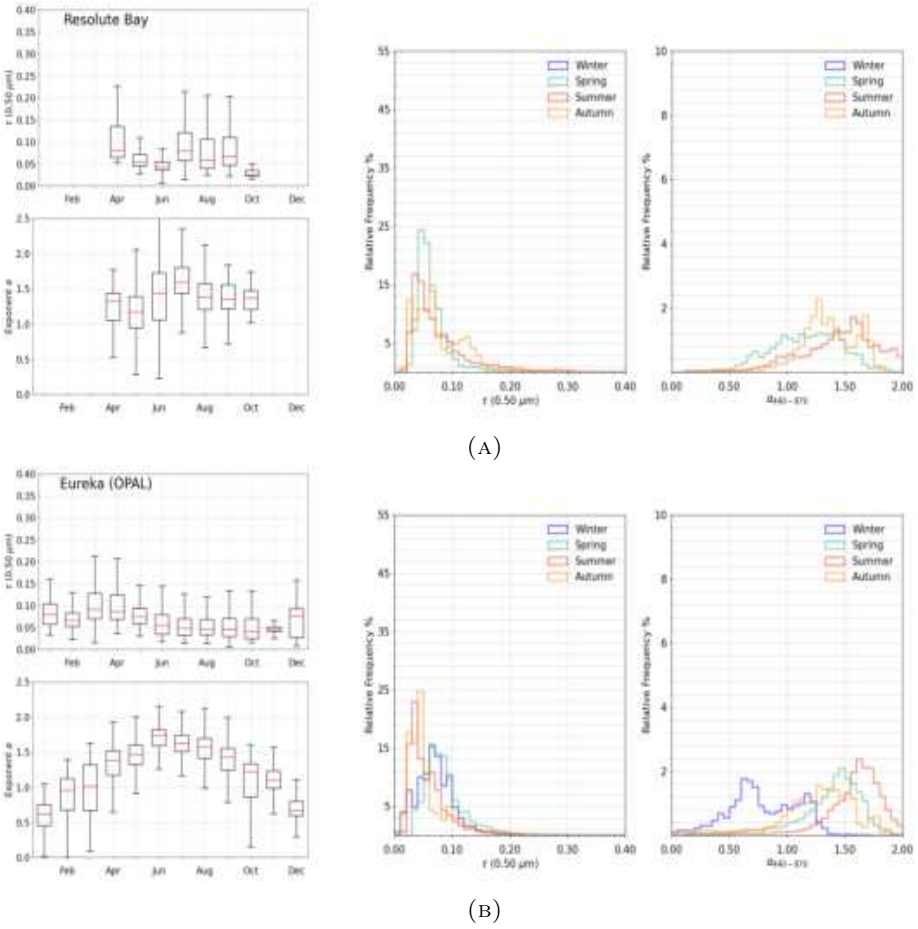

(A)

(B)

FIGURE 6.4: As in Fig.6.2, for the multi-year sun-photometer measurements of aerosol optical depth $\tau(0.500\mu m)$ and exponent α conducted at: (a) Resolute Bay by AEROCAN; (b) Eureka (OPAL).

The results from AERONET measurements conducted in the Canadian Arctic at Resolute Bay (July 2004 to December 2023) and Eureka (OPAL) (April 2007 to December 2023) are shown in Fig.6.4. At Resolute Bay, a CIMEL CE318 sun-sky photometer measured aerosol optical thickness during the spring-summer period, when the solar airmass was above the acceptance threshold. At Eureka, a sun-sky-lunar photometer (model CE318-T) was installed in April 2016, allowing for additional measurements of τ and exponent α during the polar night.

At Resolute Bay, the monthly mean values of $\tau(0.500\mu m)$ are higher and more variable during the spring, ranging between 0.06 and 0.08, and show a decreasing trend in the following months. This decline should continue until reaching a minimum mean value of approximately 0.03 in October, as observed by Tomasi et al. 2015. Since air masses at this site primarily carry aerosol particles from the North American continent (Hirdman et al. 2010), the relatively elevated monthly mean τ values observed in July, August, and September may be attributed to an increased frequency of wildfire events affecting forested regions of Canada during the summer months (Jain et al. 2024).

The Eureka (OPAL) station, being more remote, seems to be less impacted by local sources compared to Resolute Bay. This is reflected in the monthly mean values of the exponent α. During the summer, α values at Eureka range between 1.30 and 1.50,

indicating an atmosphere dominated by the presence of smaller particles. The values steadily decrease to around 0.50 in the other months, reaching their lowest during December and January, when the Arctic haze is most intense and dominated by larger particles. There may also be increased cirrus cloud contamination in the polar night data during winter at the Eureka site, due to the less robust cloud-screening procedures that can be applied in the absence of aureole data at night. At Resolute Bay, the monthly mean values of α show smaller variations, staying around 1.40, suggesting the dominance of a relatively uniform background aerosol population, rather than indicating a complex mixture of aerosols; the lack of moon-photometer data during the polar winter forestalls any characterization of α variations. Fig.6.4 also indicates that the RFHs of α are asymmetrical. At Eureka, the winter seasons exhibit a bimodal distribution of values, with peaks at 0.60 and 1.15. In contrast, the other seasons display wider left-hand tails, with higher values during summer, ranging from 1.48 (Resolute Bay) to 1.60 (Eureka).

In the Canadian Arctic, two additional stations, Alert and Cambridge Bay, were studied but not included in the main body of this paper. Both stations are managed by Environment and Climate Change Canada - AEROCAN, and use the sun-sky-lunar CIMEL CE318-T instrument to acquire aerosol extinction properties data. However, $\tau(0.500\mu m)$ and α are not presented in this paper for two main reasons: (i) the solar data at both stations were only available at level 1.5, whereas level 2 AERONET data were used for the other stations in this study. (ii) There were insufficient measurements available, particularly between March and September 2024 at Alert, and between September and October 2024 at Cambridge Bay. As a result, it was not possible to retrieve statistically representative multi-annual monthly mean values for these parameters at these stations.

6.4.3 Greenland

Fig.6.5 shows the results from multi-year sun-photometer measurements conducted at three locations in Greenland: (i) Thule in central-west coast of Greenland, (ii) Kangerlussuaq on the southwest coast, and (iii) Ittoqqortoormiit on the east coast. All sites are managed by NASA Goddard Space Flight Center (see Table 6.1 for more details).

At Thule, the monthly mean $\tau(0.500\mu m)$ values slowly decreased from around 0.07 in March-April-May to about 0.03 in October-November. The exponent α remained stable between March and September, with values between 1.30 and 1.60, before dropping sharply to around 0.60 in November-December due to the arrival of polluted air masses. The winter RFH for $\tau(0.500\mu m)$ had a mean value of 0.04, with an almost-symmetrical shape and a long right-hand tail, influenced by Arctic haze episodes. The RFH at Thule for α shows an almost symmetrical distribution of data during spring, summer, and autumn. During winter, however, the measurements were concentrated within a smaller range of values. The mean α dropped from between 1.32 and 1.55 in spring and summer to 0.66 in winter. This suggests that there were no significant changes in aerosol composition, except in winter. However, the winter α value appears too low for pollution aerosols, which are typically dominated by fine-mode particles. Therefore, it is more likely that the reduction in α is due to contamination from cirrus clouds in the nighttime data.

The same pattern for α can be observed at Ittoqqortoormiit, with an almost symmetrical distribution of α during spring and autumn, having mean values of 1.24

and 1.17, respectively. winter values seem less influenced by coarse particles, with a mean of 0.73, which is slightly higher than at Thule.

On the other hand, the Kangerlussuaq station appeared less impacted by Arctic haze. The mean value of α during winter was 1.08, and it increased to 1.52 in the summer season. These features differ slightly from those reported by Tomasi et al. 2015, mainly due to the larger dataset analyzed in this study. More importantly, the current dataset benefits from the ability to close data gaps during the polar night, which was previously not possible.

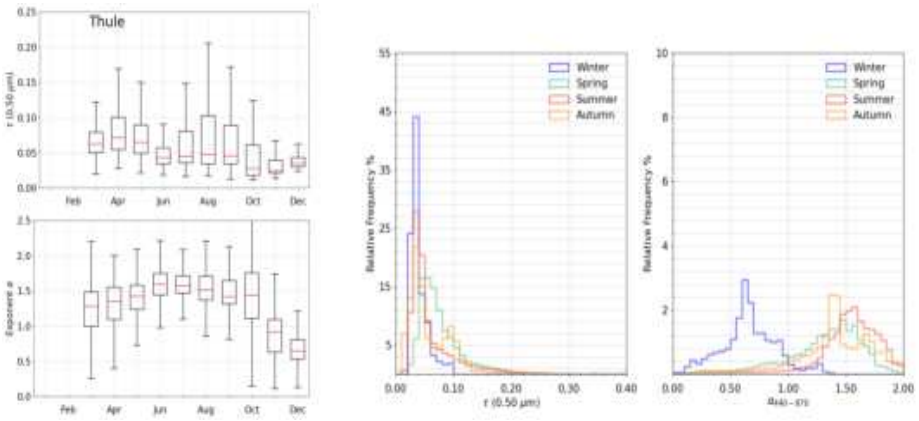

(A)

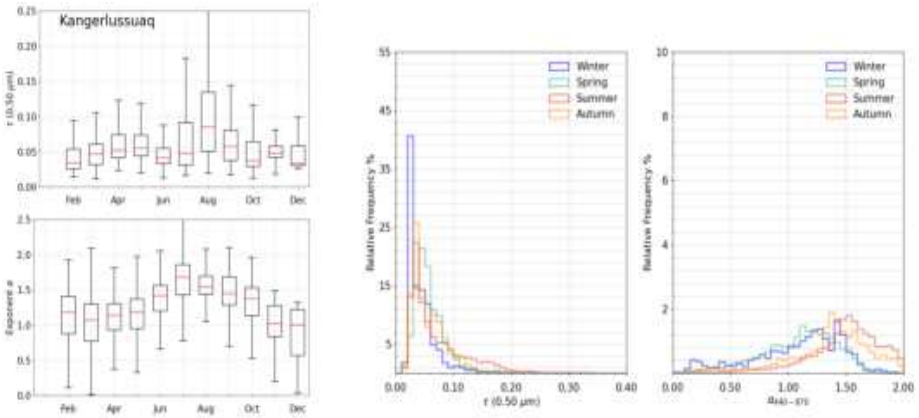

(B)

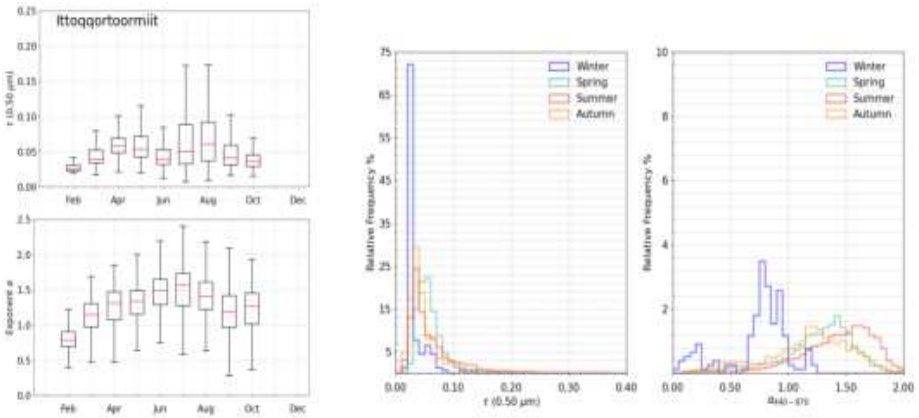

(C)

FIGURE 6.5: As in Fig.6.2, for the multi-year sun-photometer measurements of aerosol optical depth $\tau(0.500\mu m)$ and exponent α conducted at: (a) Thule, (b) Kangerlussuaq and (c) Ittoqqortoormiit by NASA Goddard Space Flight Center. To show clearly the RFH of $\tau(0.50\mu m)$, the y-axis scale for the Ittoqqortoormiit station has been adjusted to range from 0 to 75.

6.4.4 Svalbard Archipelago

The Ny-Ålesund station can be described as a 'super-station' due to the collaboration of several institutions conducting photometric studies using various types of photometers. Measurements taken at Ny-Ålesund by the AWI and the University of Valladolid using a CIMEL CE318-T, by the AWI with an SP1A, and by PMOD with a PFR are presented in Fig.6.6.

In 2017, the AWI, in partnership with the University of Valladolid, installed a sun-sky-lunar photometer. Data were collected from June 2017 to December 2023 (excluding December), providing valuable insights even during the polar night. The monthly mean values of $\tau(0.500\mu m)$ at Ny-Ålesund ranged from 0.06 to 0.07 during March and April, gradually decreasing to about 0.04 in June and October. The RFHs of $\tau(0.500\mu m)$ exhibited a typical asymmetrical shape with long right-hand tails. The distribution was narrower during the winter and became wider in the spring and summer seasons. The monthly mean values of α increased from around 1.30 in March to 1.70, remaining relatively stable until September. However, following the polar dome's expansion toward mid-latitudes and the intrusion of polluted air masses, α values dropped from 1.00 in October to around 0.90 in February. In line with the findings of Tomasi et al. 2015, the RFHs of α showed more dispersed features during winter, with a bimodal distribution shifted towards smaller values. This reflects greater variability in the aerosol mix during Arctic haze events, which bring fine particles from long-range transport and coarse particles from local sources or sea spray. During summer and autumn, α values ranged between 1.40 and 1.70, largely due to the increased variability of fine-mode particles, primarily driven by wildfire emissions with respect to coarse mode particles.

AOD was routinely measured at Ny-Ålesund also by AWI between 2012 and 2023 using an SP1A sun photometer (Fig. 6.6b). The measurements covered the period from March to October and were taken at 10 wavelengths ranging from 0.369 to 1.023 μm with a high temporal resolution of 1 minute. AWI reported that the instrument was regularly calibrated at Izaña (Spain) using the Langley method. To make the observations comparable to those from AERONET, hourly averaged data for $\tau(0.500\mu m)$ were used. The α was calculated using Equation 6.4 in the spectral range of 0.412–0.860 μm. The AWI monthly mean values of $\tau(0.500\mu m)$ ranged from 0.06 to 0.07 in spring and decreased to 0.04 during summer. A comparison of the AWI and AERONET results showed good agreement, despite differences in time periods (2012–2023 for AWI and 2017–2023 for AERONET) and coverage (AERONET also measured aerosol extinction properties during nighttime). The AWI monthly mean values of α were similar to those measured by AERONET, increasing from 1.30 in March to 1.50 in July and then gradually decreasing to 1.30 in September. Comparable seasonal mean values of $\tau(0.500\mu m)$ and α were observed between AWI and AERONET, with a maximum difference of 0.01 in spring for $\tau(0.500\mu m)$ and 0.06 in summer for α.

The PMOD measured aerosol extinction properties at Ny-Ålesund using a PFR from May 2002 to September 2023 (Fig. 6.6c), with measurements recorded every minute using four narrow-band interference filters centered at 0.368, 0.412, 0.500, and 0.862 μm. The α exponent was calculated within the spectral range of 0.412–0.862 μm. The parameters were averaged hourly. The PFR was calibrated annually at PMOD/WRC in Davos, Switzerland, during the polar winter. The monthly mean values of $\tau(0.50\mu)$m and their seasonal variations align with results from other instruments. Specifically, $\tau(0.50\mu)$m averaged around 0.08 between March and May, coinciding with the final episodes of Arctic Haze. During the summer, the monthly

mean decreased to a minimum of about 0.04 in September, when the Arctic atmosphere is typically cleaner.

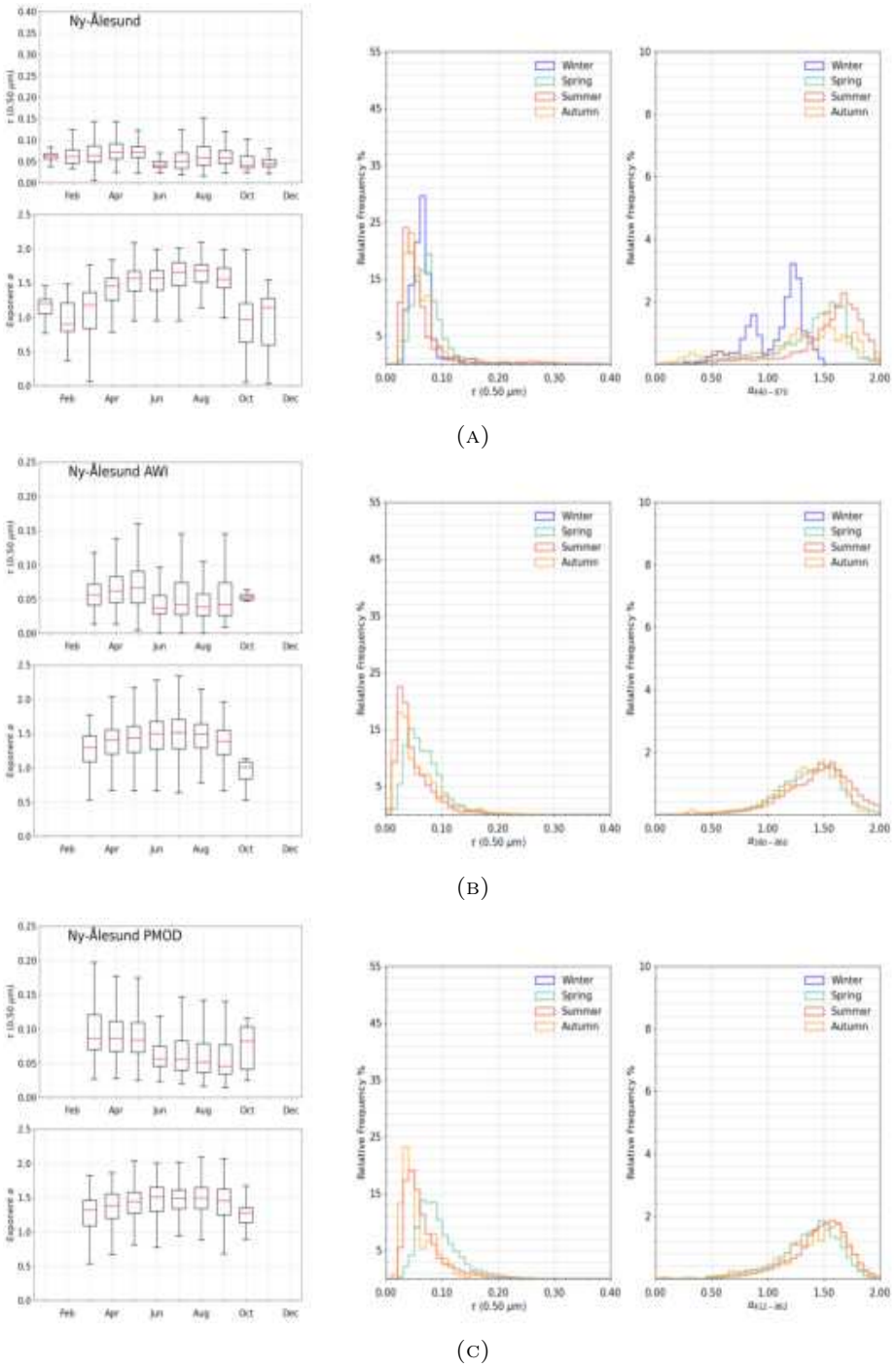

(A)

(B)

(C)

FIGURE 6.6: As in Fig.6.2, for the multi-year sun-photometer measurements of aerosol optical depth $\tau(0.500\mu m)$ and exponent α conducted at Ny-Ålesund: (a) by AWI and University of Valladolid using a CIMEL CE318-T, (b) by AWI using a SP1A, and (c) by PMOD and Norwegian Polar Institute using a PFR.

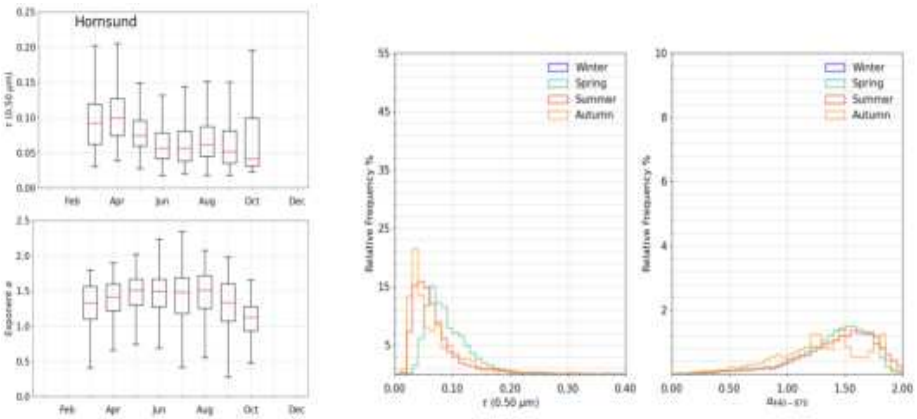

(A)

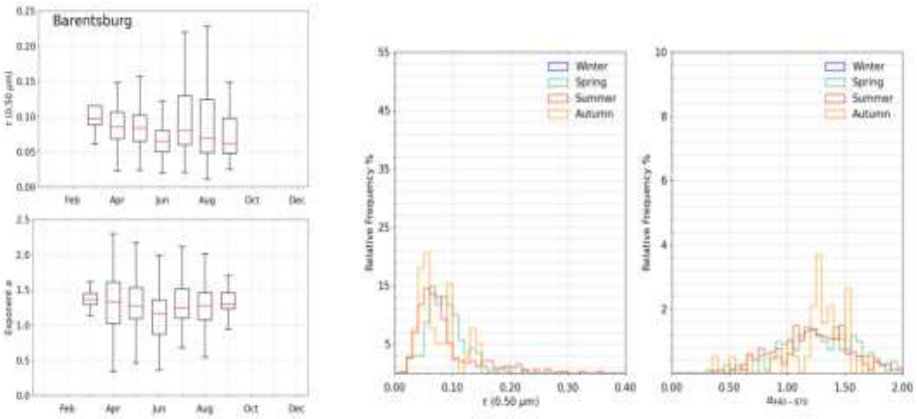

(B)

FIGURE 6.7: As in Fig.6.2, for the multi-year sun-photometer measurements of aerosol optical depth $\tau(0.500\mu m)$ and exponent α conducted at: (a) Hornsund by Polish Academy of Sciences and (b) Barentsburg by Russian Academy of Sciences.

A subsequent increase was observed in October and towards the winter season. Unfortunately, the PFR only provided sun-photometer data. The monthly mean values of α were also highly consistent, ranging between 1.30 and 1.50 from March to October. The RFHs of $\tau(0.50\mu)$m showed an asymmetrical distribution with a right-skewed tail, with a mean value of 0.07 in summer and 0.09 in spring. Similarly, the RFHs of α displayed an asymmetrical distribution, with a left-skewed tail toward smaller values, and had a consistent shape and mean value of about 1.40 across all seasons.

The results observed at Ny-Ålesund closely matched those observed at Hornsund, even though the two sites are 200 kilometers apart. The Hornsund station collected a longer data series, covering the period from May 2004 to December 2023, with measurements taken between March and October. As shown in Fig.6.7a, Hornsund displayed maximum monthly mean values of $\tau(0.500\mu m)$, ranging from 0.09 in March to 0.10 in April, followed by a decline through the summer and autumn, reaching about 0.04 in October. The monthly mean values of α at Hornsund remained stable between March and August, ranging from 1.30 to 1.50, with only small differences compared to Ny-Ålesund. The Hornsund RFHs of $\tau(0.500\mu m)$ show that the spring mean values were higher than those obtained during summer and autumn by more than 0.03. Even in this case, the shape of the distributions were in good agreement

with those reported at Ny-Ålesund. Unfortunately, no data are available for this site during winter.

At Barentsburg, the Arctic and Antarctic Institute, jointly with the Institute of Atmospheric Optics, carried out daily data collection from 2011 to 2023 (see Table 6.1) using a solar portable photometer SPM and its analogue with a sun tracker system (SP-9). These devices were developed to monitor the spectral transparency of air in the range 0.340–2.140 μm. In line with other stations, aerosol optical depth was investigated at 0.500 μm, while the Ångström exponent was calculated in the spectral range 0.440–0.870 μm. The measurements are shown in Fig.6.7b. The monthly mean values of $\tau(0.500\mu m)$ decreased from approximately 0.10 in March to 0.07 in September, reflecting the typical behavior of an Arctic site. During the same period, α varied between 1.20 and 1.40. The RFHs of daily mean $\tau(0.500\mu m)$ showed similar mean values across all seasons, with 0.09 in spring and summer and 0.07 in autumn. However, these RFHs exhibited elongated right tails, indicating occasionally high $\tau(0.500\mu m)$ values. In contrast, the RFHs of α followed a Gaussian distribution, with mean values smaller than those reported by other stations in the Svalbard Archipelago. Specifically, the mean α was 1.32 during spring, 1.23 during summer, and 1.28 during autumn. The spread of $\tau(0.500\mu m)$ values observed during July and August highlights the significant influence of smoke aerosols from boreal wildfires, as previously reported by Kabanov et al. 2023. The phenomenon of summer forest fires was most pronounced during the period 2010–2020. As a result, it is more evident at Barentsburg than at the other stations in Svalbard, although it can still be observed elsewhere.

6.4.5 Scandinavia

Fig.6.8 presents the time patterns of monthly mean values for $\tau(0.500\mu m)$ and α, as well as the seasonal RFHs for both parameters, derived from the Scandinavian stations at Andenes, Sodankylä, and Matorova (see Table 6.1 for details). The behavior of these parameters differed from those observed at other Arctic sites, as shown in Figs. 6.2 to 6.7.

At Andenes, the monthly mean values of $\tau(0.500\mu m)$ increased from 0.03 in February to 0.06 in April, remaining relatively stable during the summer and autumn before slowly decreasing to 0.04 by October. The seasonal variation from winter-spring to summer-autumn was less pronounced. The monthly mean values of α, consistent with the findings of Tomasi et al. 2015, increased from 0.70 in January to 1.60 in July, followed by a decline until December.

At Sodankylä, the monthly mean values of $\tau(0.500\mu m)$ stayed relatively stable between February and September, around 0.06, before decreasing to about 0.04 in October-November and rising again to 0.08 in December-January. The trend for α exhibited a bell-shaped pattern, similar to Andenes, increasing from 0.90 in February to 1.80 in July. At Matorova, data were available for the whole year, covering the period from September 2020 to September 2024. The monthly mean values trend of $\tau(0.500\mu m)$ showed a bell shape, with minimum values around 0.03 in February and November, and maximum values of about 0.07 during late spring and summer. The α trend followed a similar pattern to the other Scandinavian stations, peaking at 1.70 in summer and reaching a minimum of around 0.80 in January, in the middle of the winter season. Despite the different measurement periods at these stations—February 2002 to December 2023 for Andenes, March 2013 to December 2023 for Sodankylä, and September 2020 to September 2024 for Matorova—the RFHs for both $\tau(0.500\mu m)$

and α displayed similar characteristics. The RFHs for $\tau(0.500\mu m)$ exhibited an asymmetrical shape with a wider distribution compared to those of other Arctic stations. Meanwhile, the RFHs for α showed a broader distribution of values across all seasons, with winter values displaying a bimodal shape and a distribution over smaller values. Due to the proximity of these Arctic stations to the Euro-Asian continent and the alternation of polluted air masses with sea-salt particles from ocean regions, the monthly mean values of $\tau(0.500\mu m)$ remained stable throughout the year, without exhibiting the typical seasonal trend expected for Arctic stations. When comparing Andenes and Sodankylä, it is found that the overall AOD values are generally similar, mainly because both sites are affected by similar regional air mass transport, despite their different local aerosol types. Sodankylä, as a clean continental site, typically shows higher α and lower coarse mode concentrations, while Andenes, being a coastal site, is influenced by marine aerosols and sea salt, which maintain a higher coarse-mode contribution throughout the year (Rodríguez et al. 2012; Toledano et al. 2012).

In the Russian Federation, only the Cape Baranova station has been studied but not shown, consistent with the approach taken for the Arctic sites of Alert and Cambridge Bay. At Cape Baranova, the Russian Academy of Sciences investigated aerosol extinction properties using an SP-9 instrument, the same model employed at Barentsburg. The measurements were recorded from April 2018 to August 2021, with a total of 59 daily observations. The mean values of $\tau(0.500\mu$m) and α were 0.081±0.045 and 1.67±0.34, respectively. Due to the limited number of measurements and the lack of data for 2020, it was not possible to assess the aerosol climatology at this station.

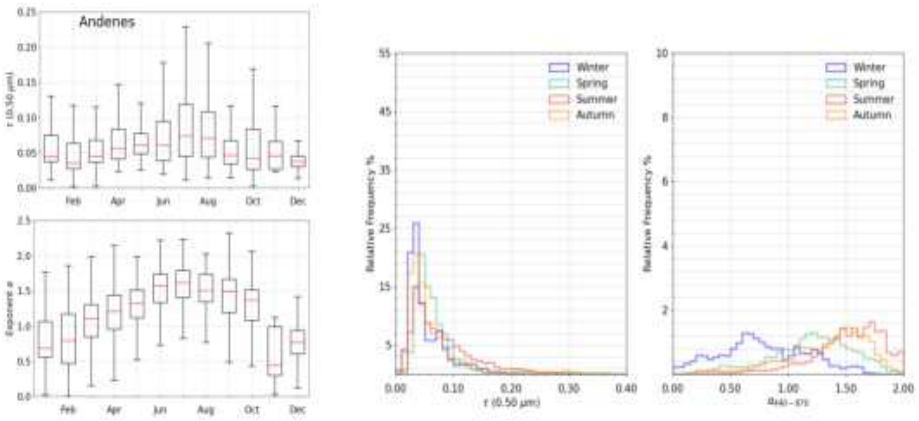

(A)

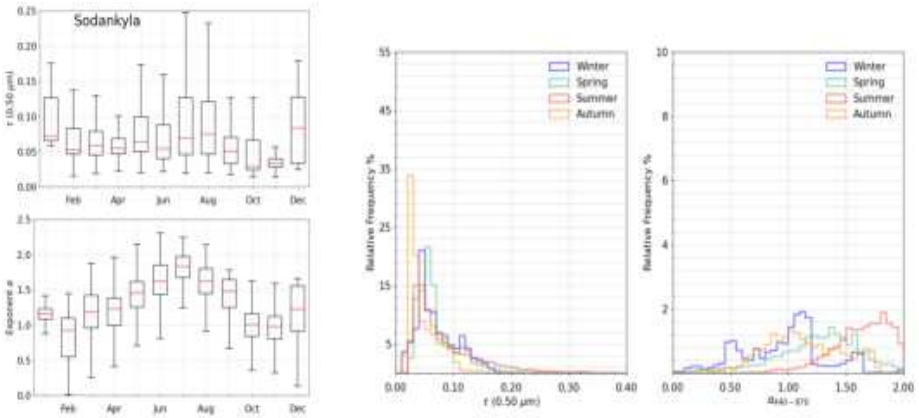

(B)

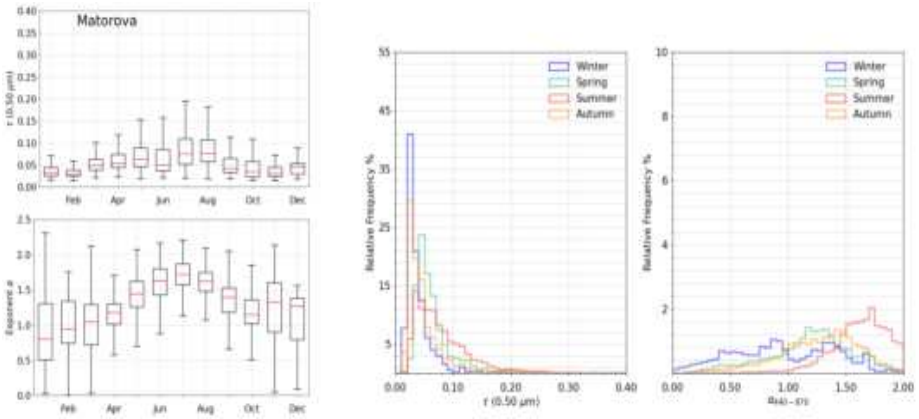

(C)

FIGURE 6.8: As in Fig.6.2, for the multi-year sun-photometer measurements of aerosol optical depth $\tau(0.500\mu m)$ and exponent α conducted at: (a) Andenes by Andøya and University of Valladolid, (b) Sodankylä and (c) Matorova by the Finnish Meteorological Institute.

6.5 Measurements in Antarctica

Table 6.2 presents information about the eleven Antarctic sites discussed in this paper. The geographical locations of these stations are shown in Fig. 6.1b. As for the Arctic, we use level 2 data for solar photometry and level 1.5 data for lunar photometry, both

from AERONET. For the Antarctic sites, where the seasons are reversed, the austral summer was defined as December to February; autumn (March to May); winter (June to August); spring(September to November).

The main difference between the Arctic and Antarctica is the distribution of stations across the poles. Since Antarctica is more isolated from other continents, there are very few stations for photometry observations. Most of the sites are located on the Antarctic Peninsula because it's closer to South America, allowing for interesting measurements due to favorable atmospheric conditions. Six other stations are in the Atlantic sector of Antarctica, and two are located on the Antarctic Plateau (Fig. 6.1b). Due to the scattered and uneven distribution of sites in Antarctica, it is difficult to get a complete picture of aerosol evolution and behavior on the continent.

6.5.1 Antarctic Peninsula

The results from sun-photometer measurements taken at the Antarctic Peninsula, specifically at Escudero, Juan Carlos I, and Marambio stations, are shown in Fig.6.9 and 6.10.

Stations - ID	Managing Institutions	Instrument model	Coordinates and Altitude	Measurement Period	Lunar Data started
Antarctic sites					
Dome C - 10	National Research Council, Italy - NOAA, US	SP02 and CMDL	75.1800 S, 123.3800 E, 3233 m a.m.s.l.	November 2010 - February 2020 [3,735]	no
Escudero - 2	University of Santiago, Chile - Chilean Antarctic Institute, Chile	CE318	62.2015 S, 58.9657 W, 33 m a.m.s.l.	December 2019 - December 2023 [2,616]	February 2020 [356]
Juan Carlos I - 1	University of Valladolid, Spain	CE318	62.6630 S, 60.3894 W, 5 m a.m.s.l.	December 2022 - December 2023 [487]	March 2023 [25]
Marambio - 3	University of Valladolid, Spain	CE318	64.2400 S, 56.6252 W, 200 m a.m.s.l.	February 2008 - December 2023 [15,204]	January 2018 [2,344]
Marambio - 3	Finnish Meteorological Institute, Finland - Physical Meteorological Observatory Davos, Switzerland	PFR	64.2400 S, 56.6252 W, 200 m a.m.s.l.	February 2005 - May 2016 [2,748]	no
Mirny - 9	Arctic and Antarctic Research Institute - Zuev Institute of Atmospheric Optics, Russia	SPM	66.3300 S , 93.0100 E, 40 m a.m.s.l.	January 2013 - May 2023 [939]	no

Continued on next page

Antarctic sites (continued)

Stations - ID	Managing Institutions	Instrument model	Coordinates and Altitude	Measurement Period	Lunar Data started
Neumayer 3 - 4	Leibniz Institute for Tropospheric Research, Germany - Alfred Wegener Institute, Germany	CE318	70.6652 S, 8.2836 W, 65 m a.m.s.l.	January 2023 - December 2023 [5,494]	March 2023 [818]
Syowa - 7	Japan Meteorological Agency, Japan	MS110 and PFR	69.0053 S, 39.5811 E, 29 m a.m.s.l.	January 1996 - December 2020 [6,098]	no
South Pole - 11	NASA Goddard Space Flight Center, US	CE318	90.0000 S, 70.3000 E, 2835 m a.m.s.l.	November 2007 - December 2023 [19,595]	no
South Pole - 11	NOAA, US	SP02	90.0000 S, 70.3000 E, 2835 m a.m.s.l.	November 2001 - March 2014 [1,894]	no
Troll - 5	NILU, Norway - Physical Meteorological Observatory Davos, Switzerland	PFR	72.0167 S, 2.5333 E, 1309 m a.m.s.l.	January 2007 - December 2023 [898,339]	no
Trollhaugen - 5	NILU, Norway - Physical Meteorological Observatory Davos, Switzerland	PFR	72.0117 S, 2.5351 E, 1553 m a.m.s.l.	January 2007 - December 2023 [898,339]	no
Utsteinen - 6	Royal Belgian Institute for Space Aeronomy, Belgium	CE318	71.9500 S, 23.3333 E, 1396 m a.m.s.l.	February 2009 - December 2023 [12,992]	no
Vechernaya Hill - 8	National Academy of Sciences of Belarus, Belarus - University of Lille, France	CE318	67.6600 S, 46.1580 E, 80 m a.m.s.l.	December 2008 - December 2023 [7,846]	no

TABLE 6.2: List of Antarctic stations using different models of photometer. For each station, the coordinates and altitude are specified, along with the measurement period for solar photometry and the installation period of the lunar model. The number of measurements for both the solar and lunar periods is provided in parentheses.

At Escudero station, data was collected from December 2019 to December 2023, showing greater variability in monthly mean values of $\tau(0.500\mu m)$. The AOD ranges from around 0.04 in December to 0.11 in September. The RFHs are similar to those at Marambio, with an asymmetrical right-hand shape for $\tau(0.500\mu m)$ and a more

symmetrical distribution for α. These findings are consistent with those reported by Tomasi et al. 2015, where the authors attributed this pattern to the presence of sea salt particles, which dominate the extinction process.

Juan Carlos I station provided data from December 2022 to December 2023, representing the shortest timeseries of this sector. Since this station operates only during the austral summer, measurements were taken only from December to March. The monthly mean values of $\tau(0.500\mu m)$ ranged from 0.06 in January to 0.09 in March. There was a decreasing trend in the first two months, followed by an increase in the last two months of the series. The monthly mean values of α were very low, ranging from about 0.30 in March to 0.60 in February, likely due to the particles being of sea salt origin. In general, since data is only available for the summer months, it is difficult to draw consistent conclusions about aerosol behavior. Due to the limited number of measurements, the RFH of $\tau(0.500\mu m)$ shows an asymmetrical distribution in summer and unclear dispersion in autumn.. The mean value during summer was 0.08, with the 25th and 75th percentiles at 0.05 and 0.08, respectively. The RFH of α was also quite symmetrical in the 0.10–1.00 range, with a mean value of 0.48, and the 25th and 75th percentiles differed by less than 0.20 from each other.

The measurements at Marambio have been conducted by the University of Valladolid since February 2008 by using a CIMEL sun-sky-lunar photometer, representing the longest time series in this sector of the continent. The monthly mean values of $\tau(0.500\mu m)$ range from about 0.03 in October to 0.07 in July, while the exponent α varies from 0.60 in June to 1.40 in February. A seasonal trend is observed for α, with higher values during the austral summer and lower values in winter.

The FMI also collaborates with Physical Meteorological Observatory Davos (PMOD) at the same station, measuring aerosol extinction parameters using a PFR sun-photometer. Quality assured aerosol optical depth and Ångström exponent for Marambio GAW/PFR station, from February 2005 to May 2016, were provided by PMOD. Measurements were taken with a high temporal resolution of 1 minute at four wavelengths, namely 0.368, 0.412, 0.500, and 0.862 μm. The α was calculated for the spectral range of 0.412–0.862 μm. Processing and quality checks were performed according to the protocols of the World Optical Depth Research and Calibration Center (WORCC). The PFR sun-photometer collected data even during the winter-spring season, despite being a sun-based instrument. This was possible because of the station's location at 64°S, where some light is still present during winter. The monthly mean values of $\tau(0.500\mu m)$ ranged from around 0.05 in August to about 0.03 in May, while α ranged from 0.75 in August to 1.50 in December. The AOD monthly time series at Marambio showed slight differences between the CIMEL and PFR instruments, although the overall patterns were similar, with maximum AOD values during late autumn and winter, and minimum values during summer. However, the monthly trends of α showed significant differences, particularly in the data distribution. These differences may be due to the use of different quality assurance methods applied by AERONET for the CIMEL and by PMOD for the PFR. By analyzing the monthly mean values of α measured by both photometers at Marambio, as shown in Fig. 6.10, it is evident that coarse-mode particles likely dominate the atmosphere during the austral winter. In contrast, fine-mode particles are more prevalent in summer, possibly due to increased human activities and cruises in the peninsula. This seasonal shift is supported by previous studies reporting higher aerosol scattering coefficients in winter due to enhanced sea salt emissions and dominance of coarse-mode particles (Asmi et al. 2018). A similar trend is observed at the other two stations on the Antarctic Peninsula, though with slightly different magnitudes.

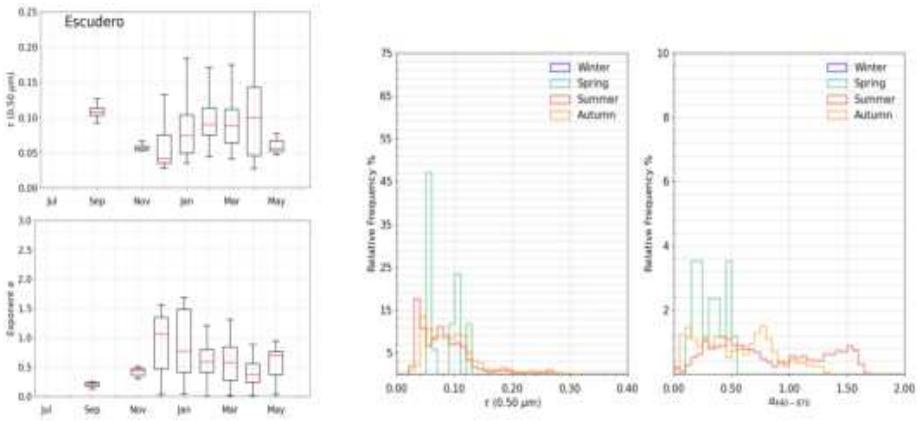

(A)

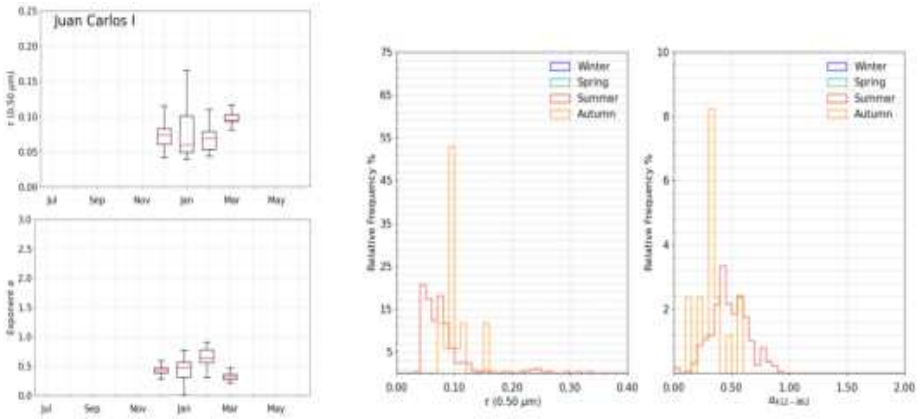

(B)

FIGURE 6.9: As in Fig.6.2, for the multi-year sun-photometer measurements of aerosol optical depth $\tau(0.500\mu m)$ and exponent α conducted at: (a) Escudero by University of Santiago and Chilean Antarctic Institute, and (b) Juan Carlos I by University of Valladolid.

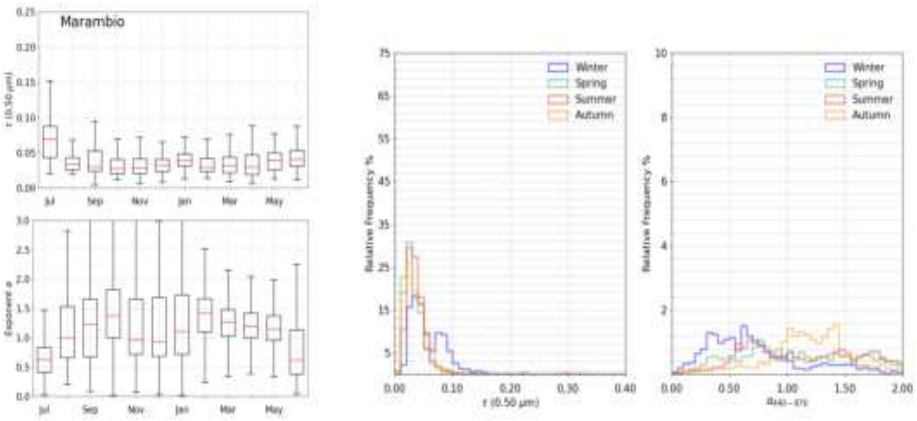

(A)

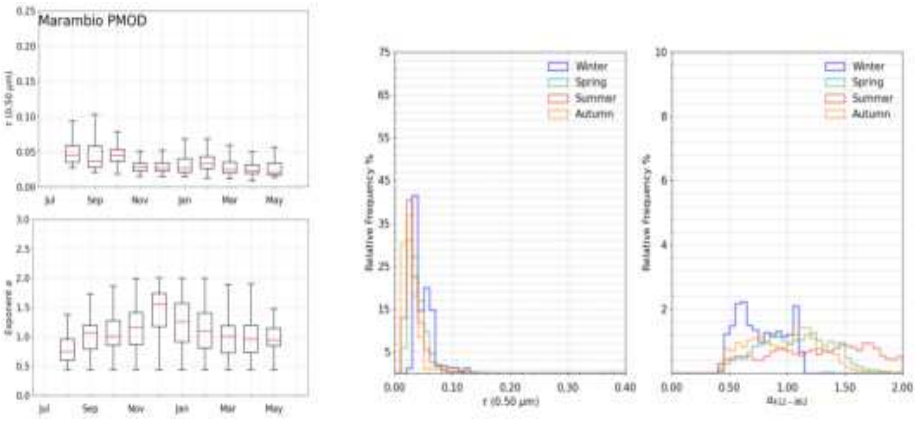

(B)

FIGURE 6.10: As in Fig.6.2, for the multi-year sun-photometer measurements of aerosol optical depth $\tau(0.500\mu m)$ and exponent α conducted at: (a) Marambio by the University of Valladolid using a CIMEL, and (b) Marambio by the Finnish Meteorological Institute and PMOD/WRC using a PFR.

6.5.2 Atlantic Sector

Fig. 6.11 and 6.12 show the results obtained from the measurements conducted at six other coastal sites in the Atlantic sector. The Neumayer measurements, conducted by the Leibniz Institute for Tropospheric Research in collaboration with the Alfred Wegener Institute, were conducted over the period November - April, showing rather stable time-patterns of the monthly mean values of $\tau(0.500\mu m)$, ranging from 0.03 to 0.05, and associated with stable values of α varying from 0.80 to 1.20. The RFH of $\tau(0.500\mu m)$ during summer showed a mean value of 0.04 and 25th and 75th percentiles of 0.03 and 0.04, respectively. The RFH for α appear symmetrical with little dispersion for all moths, with a mean value around 1.00 for all seasons.

The NILU, in collaboration with PMOD, operates a PFR sun-photometer at Troll/Trollhaugen, collecting data from January 2007 to December 2023. In February 2014, the instrument was relocated from Troll to the new Trollhaugen observatory due to local contamination. The monthly mean values of $\tau(0.500\mu m)$ show a steady trend throughout the year, with mean values ranging between 0.02 and 0.03. Similar to other stations in Queen Maud Land, located in the Atlantic sector of Antarctica, the monthly mean values of α were lower in winter and spring and higher in

summer. In general, the Antarctic baseline atmosphere is a mixture of descending free-tropospheric and lower-stratospheric air. The particle size distribution is dominated by Aitken-mode particles in summer and accumulation-mode particles in winter (Fiebig et al. 2009; Fiebig et al. 2014). These features are illustrated in Fig. 6.11 and Fig. 6.12. The RFHs of $\tau(0.500\mu m)$ show an asymmetrical distribution skewed toward smaller values across all seasons. For α, the RFHs display a Gaussian distribution in spring and autumn, with mean values of 1.29 and 1.35, respectively. In winter, the distribution is asymmetrical with a right-hand skew and a mean of 0.96. In summer, the distribution is asymmetrical with a left-hand skew and a mean of 1.47.

The data from Utsteinen and Vechernaya Hill stations were even more limited, covering the periods from November to February and November to March, respectively (see Table 6.2 for additional info). In both cases, the monthly mean values of $\tau(0.500\mu m)$ remained very stable, around 0.02 at Utsteinen and 0.03 at Vechernaya Hill. The RFHs showed the typical pattern found at other Antarctic stations, with a symmetrical distribution leaning toward lower values and a right-hand skew. At Utsteinen, during summer season, the mean value of $\tau(0.500\mu m)$ was 0.02, with the 25th and 75th percentiles at 0.01 and 0.02, respectively. At Vechernaya Hill, the mean value was 0.03, with 25th and 75th percentiles at 0.02 and 0.03. The monthly boxplot of α at Utsteinen displayed quite stable values throughout the time series, and the related RFH had a symmetrical and even distribution across all values, indicating that the stable extinction features were mainly due to sea salt particles. Some differences were observed at Vechernaya Hill, where monthly mean values of α decreased from November to March. The monthly boxplot panel of α at this station showed high values, between 2.20 in November and 1.30 in March, showing that the aerosol extinction features are in part produced by fine mode particles (e.g. non-sea-salt sulphate aerosols).

The longest time series in the Atlantic sector was provided by the Japan Meteorological Agency at Syowa Station. The first Japanese permanent research base was established in 1957. Measurements were recorded using an MS110 sun-photometer from January 1996 to February 2011, and a PFR sun-photometer from February 2011 to December 2020. Although no lunar data were recorded at the station by either instrument, the winter period appeared to be present in the RFHs due to observations during the transition from night to day. To make the measurements comparable with those from AERONET, we averaged the data hourly and then calculated monthly statistics for atmospheric turbidity parameters. Specifically, we used τ measurements at 0.500 μm and α in the spectral range of 0.412-0.862 μm. The monthly mean $\tau(0.500\mu m)$ values show no seasonality, remaining within the range of 0.02-0.03 during the period from August to April. The monthly boxplots for α clearly show the a predominance of fine aerosol particles in summer, with an average value of 1.43 during this season. In contrast, coarse particles, likely influenced by sea salt due to the station's location on an island 4 km from the coast, dominate in winter, with a seasonal mean value of 0.84.

Figure 6.12c presents the results of measurements conducted at Mirny using an SPM handheld sun photometer between January 2013 and May 2023, covering the period from August to May each year. This Russian device, developed by the Institute of Atmospheric Optics, records incoming solar radiation at 10 different wavelengths ranging from 0.339 to 2.139 μm. To ensure comparability between stations, the 0.500 μm wavelength was selected for AOD measurements, while the α was calculated using the wavelength range of 0.443–0.871 μm. The monthly mean values of $\tau(0.500\mu m)$ ranged from 0.02 to 0.03, while the mean values of α varied from approximately 1.30

during the summer months to 0.80 in late winter and early spring. The RFHs of $\tau(0.500\mu m)$ showed nearly symmetrical peaks across all seasons, with mean values of 0.02 during all the season, with little differences. In contrast, the RFH of α exhibited a wider dispersion over the measured range. The seasonal mean and median values of α were consistently within the interval of 0.80–1.30. These findings indicate that aerosol extinction features at Mirny were predominantly influenced by sea-salt particles, likely generated by wind activity over the Antarctic Ocean. This is a common feature observed at all Antarctic stations in the Atlantic region.

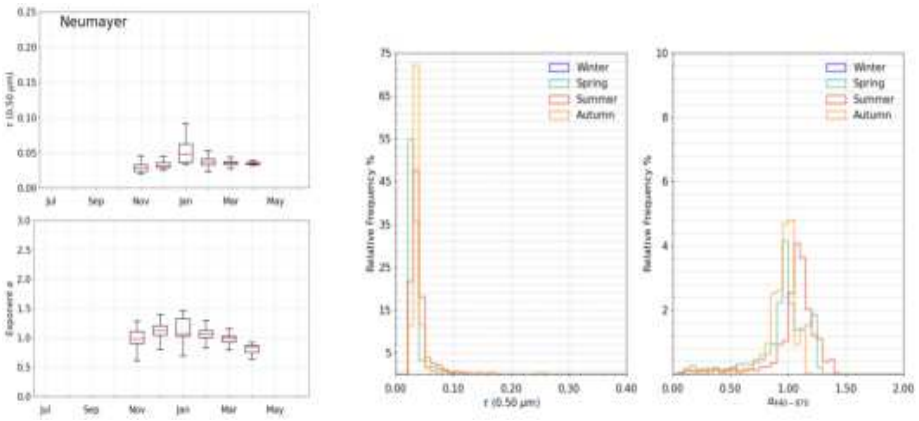

(A)

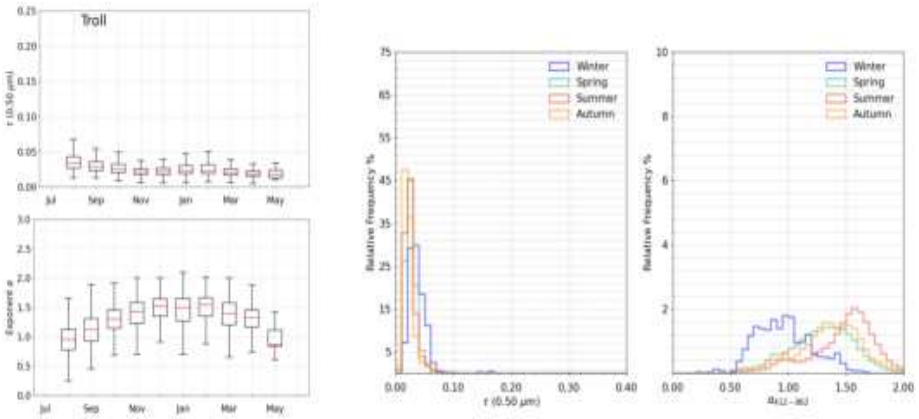

(B)

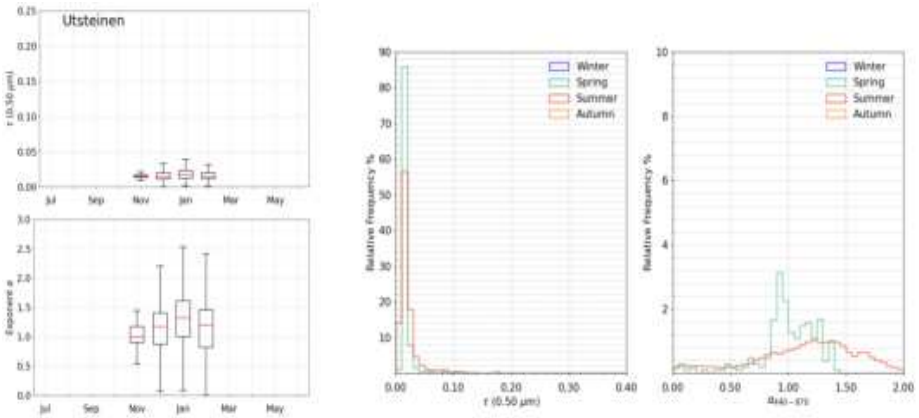

(C)

FIGURE 6.11: As in Fig.6.2, for the multi-year sun-photometer measurements of aerosol optical depth $\tau(0.500\mu m)$ and exponent α conducted at: (a) Neumayer by Leibniz Institute for Tropospheric Research and Alfred Wegener Institute, (b) Troll/Trollhaugen by NILU and Physical Meteorological Observatory Davos, and (c) Utsteinen by Royal Belgian Institute for Space Aeronomy.

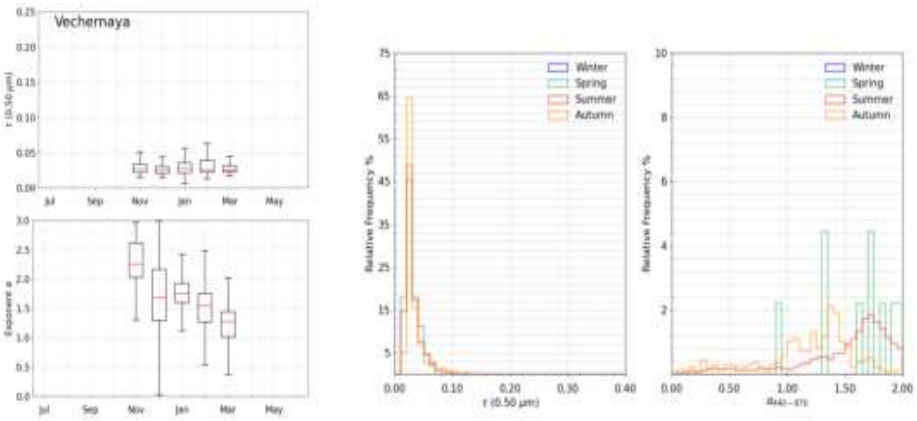

(A)

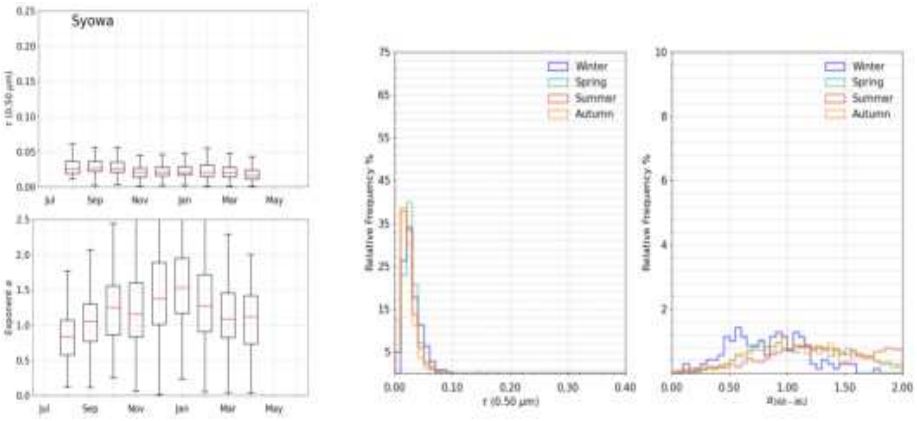

(B)

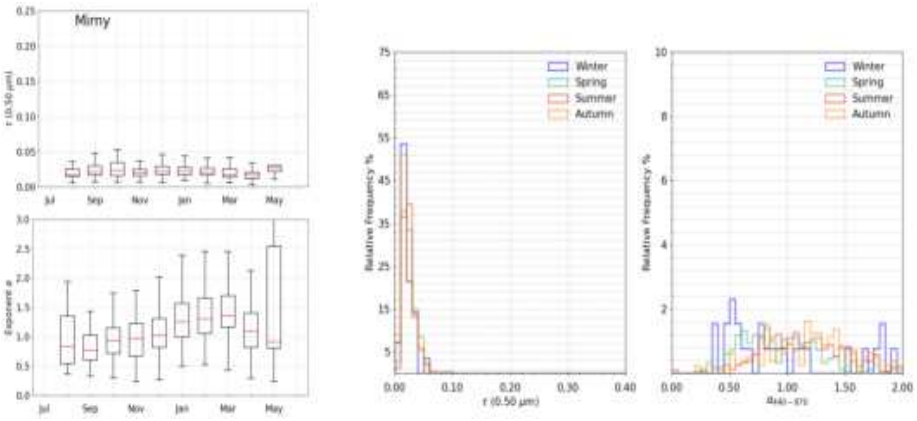

(C)

FIGURE 6.12: As in Fig.6.2, for the multi-year sun-photometer measurements of aerosol optical depth $\tau(0.500\mu m)$ and exponent α conducted at: (a) Vechernaya Hill by National Academy of Sciences of Belarus and University of Lille (b) Syowa by the Japan Meteorological Agency, and (c) Mirny by the Arctic and Antarctic Research Institute.

6.5.3 Antarctic Plateau

The results obtained at Dome C from sun-photometer measurements conducted since 2010 are shown in Fig. 6.13a. From 2010 to 2012, the NOAA contributed data using a CMDL sun-photometer, a device capable of acquiring measurements at several

spectral wavelengths: 0.368, 0.412, 0.500, 0.610, 0.675, 0.778, and 0.862 μm, with a reported accuracy of 0.02 (Kim et al. 2005). Subsequently, from 2015 to 2020, the National Research Council of Italy and the NOAA carried out measurements of aerosol extinction properties at the same site using a Carter Scott SP02 sun-photometer. Since both instruments operated at the same wavelengths and at the same location, the data are presented together in this paper rather than separately, as done for other cases. The monthly mean values of $\tau(0.500\mu m)$ obtained from these sun-photometers remained stable throughout the investigation period, with a mean value of 0.02 in November, increasing to 0.04 in February. These low values, close to the detection limit of the instruments, can be attributed to the extremely clean air at Dome C, located on the Antarctic plateau at an altitude of over 3000 m, and to the predominant role of subsidence processes in influencing aerosol loads. The monthly mean values of the α during the same period ranged from approximately 1.50 to 1.80. The RFH of $\tau(0.500\mu m)$ exhibited an asymmetrical distribution, with a right-skewed tail toward higher values. The mean $\tau(0.500\mu m)$ was 0.03 during summer and spring. The RFH of α showed a dispersed distribution in the range of 0.00–2.00, with a mean of 1.60 during summer. The 25th and 75th percentiles of α were 1.35 and 1.91, respectively.

Fig.6.13b and Fig.6.13c show the measurements of $\tau(0.500\mu m)$ and α at Amundsen-Scott station, registered as South Pole on AERONET; the station is located at the geographical South Pole and managed by NOAA (see Table 6.2). Photometric measurements were taken by NASA at this site since November 2007 by using a CIMEL instrument, covering a good period of time, but data were available only during the Austral summer between November and February. Since this station is located in the center of the continent, far away from the coast, a cleaner atmosphere was aspected. This feature was confirmed by the monthly mean values of $\tau(0.500\mu m)$, showing steady behaviour, between 0.02 in November and 0.04 in February. The RFH of this parameter showed a symmetrical shape for both seasons available (spring and summer), with mean value of around 0.02 and 25th and 75th percentiles of 0.02 and 0.03 respectively. The monthly mean values of α showed a minimum of around 0.50 in November, followed by a relatively steady behavior in the subsequent months with values around 1.0, indicating the presence of fine-mode particles even at this remote site. It is important to note that there are very few data points for October and November at the South Pole NOAA station. Therefore, the data sample for these months is not robust, and the results may be affected by even small amounts of cloud contamination. The high number of personnel and scientific activities make this station one of the most active in the continent, and local pollution sources can explain these numbers, mainly aircraft flights and fuel usage for electricity generation (Sheridan 2015). At the same site, NOAA monitored aerosol extinction features using a Carter Scott SP02 sun-photometer from November 2001 to March 2014. This instrument measured incoming solar radiation at four wavelengths: 0.412, 0.500, 0.675, and 0.862 μm. However, for this study, only the wavelength at 0.500 μm was considered. The α was analyzed across the spectral range of 0.412–0.862 μm. Figure 6.13c illustrates the monthly mean values of $\tau(0.500\mu m)$, extending the coverage from September to March. The highest values occurred in early spring (September), with a mean of approximately 0.09, while the lowest values were observed during the austral summer (December), with a mean of 0.02. The behavior of the α followed a similar trend, showing an increase from spring to summer, followed by a decrease towards autumn. Due to differences in the observation periods and the number of measurements available (see Table 6.2), the RFH of $\tau(0.500\mu m)$ displayed additional features compared

to NASA's dataset. The distribution was asymmetrical, with a right-skewed tail towards higher values. The mean value of $\tau(0.500\mu m)$ was 0.07 during summer and 0.09 during spring. Similarly, the RFH of α also showed differences. While NASA's data exhibited a bimodal distribution for both summer and spring, NOAA's measurements of α were randomly distributed across the interval, showing no dominant distribution pattern. It would be extremely interesting to understand how aerosol extinction properties evolve during the winter season at these Antarctic Plateau stations. However, due to the extremely low temperatures (as low as -70°C), designing a heating system that ensures the photometer's proper functionality is challenging.

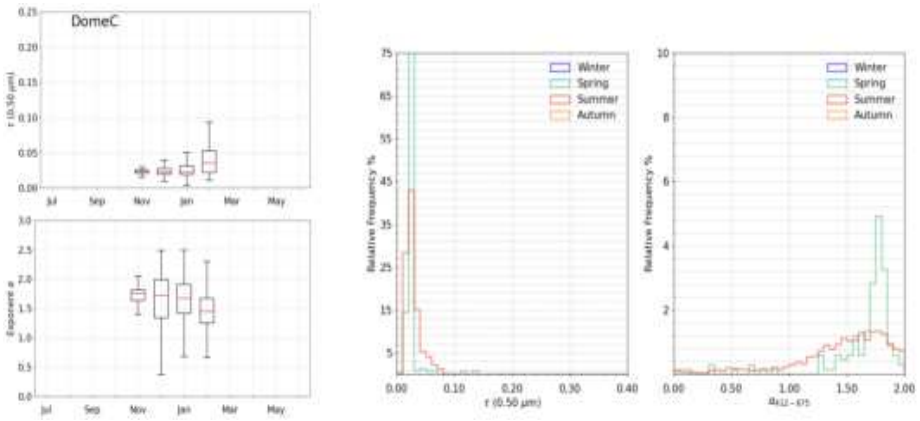

(A)

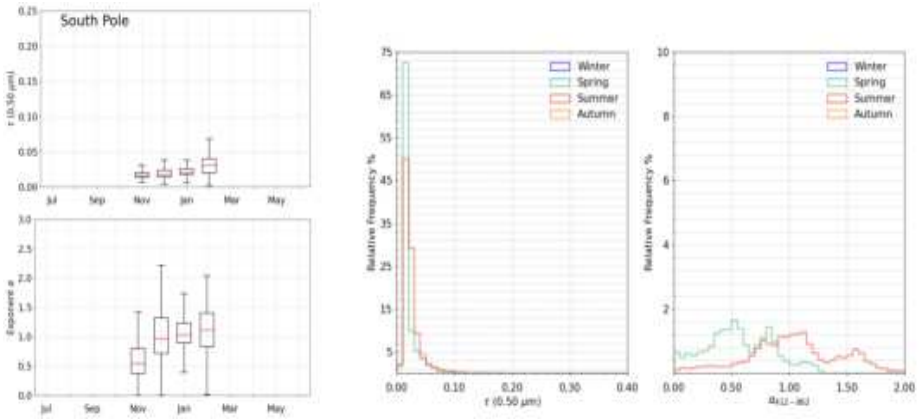

(B)

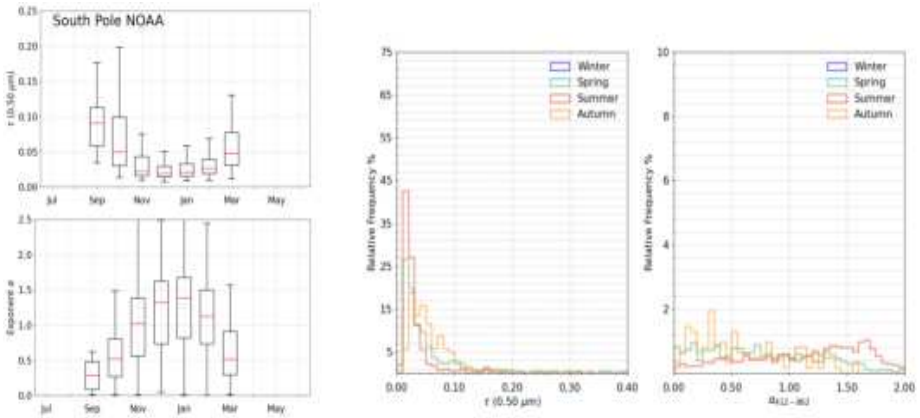

(C)

FIGURE 6.13: As in Fig.6.2, for the multi-year sun-photometer measurements of aerosol optical depth $\tau(0.500\mu m)$ and exponent α conducted at: (a) Dome C by National Research Council of Italy and National Oceanic and Atmospheric Administration (NOAA), (b) South Pole by NASA/GSFC, and (c) South Pole by NOAA.

6.6 AOD trend analysis

Calculating trends is one of the most important and common tasks in climatological studies. The $\tau(0.500\mu$m) trends have been calculated for several stations at both

poles to gain a general understanding of how this parameter has changed over time. The analysis of α trends were not included in this study, because this parameter can be influenced by variations in both aerosol type and size distribution, making it challenging to derive robust conclusions from limited datasets, and because in polar regions τ values are very low leading to higher uncertainty in α retrievals.

In the Arctic, five stations were selected: Barrow representing North America; Eureka (OPAL) representing Canada; Thule for Greenland; Ny-Ålesund for the Svalbard Archipelago; and Andenes for the Scandinavian countries. In Antarctica, four stations were analyzed: Marambio representing the Antarctic Peninsula; Troll/Trollhaugen and Syowa for the Atlantic sector; and South Pole for the Antarctic Plateau.

For the trend analysis, two different approaches have been used: (i) the non-parametric Mann-Kendall test (Mann 1945, Kendall 1955), in which the null hypothesis states that the data are identically distributed, while the alternative hypothesis suggests that the data follow a monotonic trend. (ii) the Theil-Sen method (Theil 1992, Sen 1968), which, given a set of n x, y pairs, calculates the slopes between all pairs of points. The Theil-Sen estimate of the overall slope is the median of these slopes. Both approaches provide confidence intervals even with non-normal data and are resistant to outliers. To compute the trend analysis, monthly mean values of $\tau(0.500\mu\text{m})$ have been used. Deseasonalization techniques, such as Seasonal Trend decomposition using LOESS (STL), were not applied in this analysis due to the lack of data for several months of the year. Although the lunar photometry technique helps to fill historical τ gaps in polar datasets, it has been in use for less than a decade, remains sparsely distributed across the poles, and operates under optimal meteorological conditions for only about ten days per month.

Moreover, since the last work published by Tomasi et al. 2015, only three volcanic eruptions have occurred that could potentially affect the atmosphere at such high-latitude sites. These eruptions are: (i) the Raikoke volcanic island eruption in June 2019 (Russia), (ii) the Bezymianny stratovolcano eruption in May 2022 (Russia), and (iii) the Sheveluch volcano eruption in April 2023 (Russia). The Raikoke eruption is particularly relevant for the Arctic atmosphere, as it resulted in a mean stratospheric aerosol optical depth of 0.025 (Vernier et al. 2024, Sofieva et al. 2024). In-depth studies on the other two eruptions in 2022 and 2023 have not been published yet. Since there is no information available on the tropospheric impacts of these events in the Arctic, making difficult for aerosol models to simulate the lifecycle of the particles, and since Antarctica did not appear to be influenced by the volcanic eruptions, the data has not been cleaned to account for these events.

Table 6.3 summarizes the key statistics from the trend analysis of all selected stations, as determined by the Mann-Kendall test. In this analysis, Kendall's tau serves as a non-parametric measure to evaluate the strength and direction of the trend, ranging from -1 (perfect negative correlation) to 1 (perfect positive correlation). The p-value indicates the significance level of the trend, with lower values signifying a trend that is statistically significant. Fig.6.14 shows the dominant trends identified by Theil-Sen regression for the Arctic station of Andenes, and the Antarctic stations of Syowa and South Pole. The trends for the other stations showed no significant results.

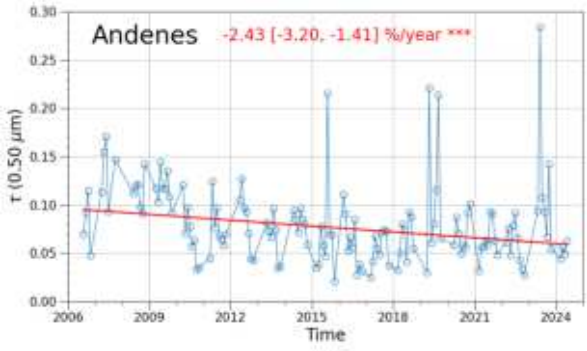

(A)

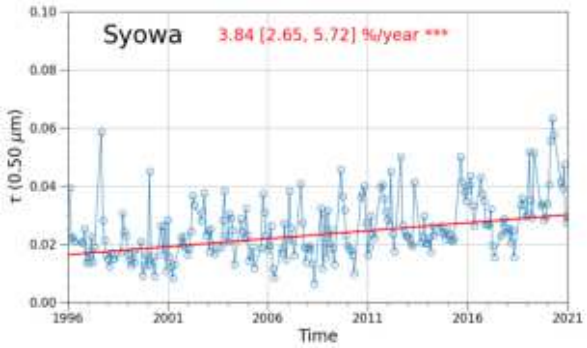

(B)

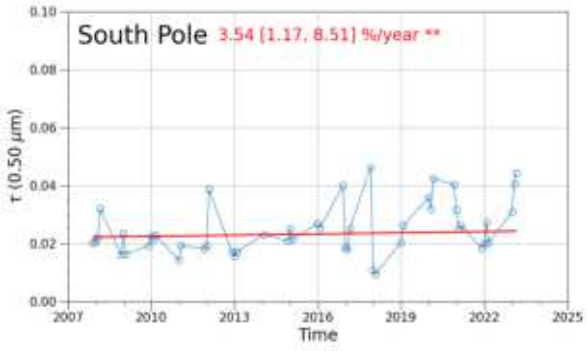

(C)

FIGURE 6.14: Theil-Sen slopes for mothly median $\tau(0.500\mu m)$ at (a) Andenes, (b) Syowa, and (c) South Pole. The solid red line shows the trend estimate; the overall trend in shown at the top as % per year, together with the 95% confidence intervals. The *** show that the trend is significant to the 0.001 level, the ** to the 0.01 level

Andenes shows a negative trend of -2.43% per year, with a Kendall's tau of -2.33e-01 and a p-value of 4.74e-05, indicating a high level of statistical significance. This negative trend can be attributed to the strict regulations on industrial emissions adopted by EU countries. Surprisingly, the Antarctic sites of Syowa and South Pole exhibit overall positive trends, with increases of $+3.84\%$ per year and $+3.54\%$ per year, respectively. Syowa has a Kendall's tau of 0.327 and a highly statistically significant of 3.02e-13, while South Pole has a Kendall's tau of 0.278 and a p-value of 5.40e-03. South Pole has relatively few monthly measurements each year, as shown in Fig.6.14, and Syowa used an MS110 photometer from 1996 to February 2011, which was replaced by a PFR instrument until 2020. Although fewer months are available for analysis

in Antarctica, these trends remain meaningful. Two possible explanations for these trends are: (i) increased activity at the South Pole station over the years, which may have led to higher aerosol loads at low levels, affecting both the local environment and the field of view of the instruments; and (ii) the influence of minor volcanic eruptions, particularly during the 2000s, when several eruptions were known to have increased stratospheric aerosol optical depth on a global scale (Vernier et al. 2011).

Station	**Kendall's** τ	**p-value**	**AOD change per year (%)**
Arctic			
Barrow	-3.27e-04	9.96e-01	-1.00e-02
Eureka (OPAL)	4.51e-02	5.65e-01	6.10e-01
Thule	-3.39e-02	6.02e-01	-4.50e-01
Ny-Ålesund	-9.40e-02	9.85e-02	-7.90e-01
Andenes	-2.33e-01	4.74e-05	-2.43
Antarctica			
Marambio	9.58e-02	3.15e-01	1.30
Troll/Trollhaugen	5.34e-02	3.38e-01	0.47
Syowa	3.27e-01	3.02e-13	3.84
South Pole	2.78e-01	5.40e-03	3.54

TABLE 6.3: Trend analysis for 9 polar stations, presenting Kendall's τ values as a measure of rank correlation, along with p-values to assess the statistical significance of the observed trends.

6.7 Ship-borne measurements

Ship-borne campaign	
Oceanic Sectors	**Measurement Period**
Eastern Chuckci Sea, Beaufort Sea and Amundsen Gulf (NAA)	March 2008 - July 2023 [85]
Northern Greenland - Norwegian Sea (GNS)	July 2007 - August 2024 [168]
Barents Sea and East Siberian Sea (BES)	April 2008 - July 2024 [27]
Southern Pacific Ocean (PAC)	January 2008 - December 2020 [60]
Antarctic Peninsula (APE)	February 2009 - February 2014 [8]
Southern Atlantic Ocean (ATL)	December 2007 - December 2020 [376]
Southern Indian Ocean (IND)	December 2007 - December 2019 [141]

TABLE 6.4: List of the seven oceanic sectors defined for the ship-borne level 2.0 sun-photometer measurements conducted from 2004 to 2024. The total number of measurements is provided in parentheses.

Since 2004, several research cruises have been conducted in the Arctic and Antarctic Ocean regions, using the Microtops instrument. The instrument was calibrated at the NASA Goddard Space Flight Center (GSFC) calibration facility, following a transfer calibration procedure from a master CIMEL instrument (Smirnov et al. 2009). Measurements focused on level 2.0 columnar aerosol radiative parameters, specifically the aerosol optical depth $\tau(0.500\mu m)$ and the Angström exponent α. These parameters were directly downloaded from the AERONET website, considering only cruises conducted within latitudes 66°N to 90°N for the Arctic and 66°S to 90°S for Antarctica. The measurements were part of the Maritime Aerosol Network (MAN), which provides validation points for satellite observations and aerosol transport models. Details about these measurements, including the measuring points considered for this study, are available on the AERONET website (AERONET Aerosol Maritime Network: https://aeronet.gsfc.nasa.gov/new_web/maritime_aerosol_network_v3.html; last access 15/05/2025).

The Microtops II sun photometer operates in two configurations: (i) with filters centered at 0.340, 0.440, 0.675, 0.870, and 0.936 μm; or (ii) with filters centered at 0.440, 0.500, 0.675, 0.870, and 0.936 μm (Smirnov et al. 2011). To ensure comparability with measurements from CIMEL instruments, only $\tau(0.500\mu m)$ and α values calculated for the wavelength range 0.440 to 0.870 μm were considered.

The Arctic cruises have been divided in three main oceanic sectors following Tomasi et al. 2015: (i) Eastern Chuckci Sea, Beaufort Sea and Amundsen Gulf (NAA) between 170°W and 110°W, (ii) Northern Greenland-Norwegian Sea (GNS) between 20°W and 30°E, and (iii) Barents Sea and East Siberian Sea (BES) between 30°E and 130°E. In Antarctica, four different sectors have been defined: (i) Southern Pacific Ocean (PAC) between 150°E and 75°W, (ii) Antarctic Peninsula (APE) between

75°W and 50°W, (iii) Southern Atlantic Ocean (ATL) between 50°W and 20°E, and (iv) Southern Indian Ocean (IND) between 20°E and 150°E. Tables S1 and S2 in the supplementary material list the scientific cruises considered for each sector and used in this study.

The ship-borne measurements were analyzed using the same criteria as those applied to the ground-based sun-photometers. As shown in Figures 6.15, 6.16, and 6.17 the daily mean values of $\tau(0.500\mu m)$ and α were grouped into monthly subsets. These subsets were used to calculate the monthly mean values for both parameters and to define their RFHs for all seasons.

6.7.1 Arctic Ocean

Figure 6.15a shows the monthly mean values of $\tau(0.500\mu m)$ and α derived from Microtops measurements conducted during ten cruises in the Eastern Chukchi Sea, Beaufort Sea, and Amundsen Gulf (NAA). Although the dataset spans from March 2008 to July 2023, only 85 observations were available between March and October. The findings align with those reported by Tomasi et al. 2015, confirming a typical seasonal trend. The monthly mean $\tau(0.500\mu m)$ was 0.10 in March, peaked at 0.15 in April and 0.17 in May, and gradually declined to 0.05 in September and approximately 0.04 in October. The α parameter remained relatively stable from March to October, ranging between 0.90 in June and 1.50 in July. The RFH of $\tau(0.500\mu m)$ exhibited a more dispersed distribution curve, spanning 0.02–0.30, compared to the GNS and BES sectors, particularly in spring and summer. During summer, the mean $\tau(0.500\mu m)$, representative of background conditions, was 0.12. This value was twice as high as that measured in the others Arctic oceanic sectors, highlighting the NAA sector as the most affected by polluted aerosols.

A total of 168 measurements from twenty-seven scientific expeditions were used to derive the same parameters for the Greenland Sea and Norwegian Sea (GNS) sector. Figure 6.15b shows that $\tau(0.500\mu m)$ values decreased from below 0.10 in April to 0.04 in September, consistent with the behavior observed by Tomasi et al. 2015 in this region. Similar to the NAA sector, the monthly mean α values in the GNS sector remained relatively stable, ranging from 1.25 in April to 1.40 in May. The average summer values for $\tau(0.500\mu m)$ and α in the GNS sector, at 0.07 and 1.30 respectively, align well with those observed at Ittoqqortoormiit (0.07 and 1.42, Fig. 6.5c) and Hornsund (0.06 and 1.44, Fig. 6.7a). These similarities occur during the summer when polar air masses are transported toward the Svalbard Archipelago. The larger number of observations for the GNS sector provided a clearer characterization of aerosol extinction features and challenged the reported similarity between these stations during spring, as noted by Tomasi et al. 2015.

In the Barents Sea and East Siberian Sea (BES) sector ten cruises were conducted spanning the period from April 2008 to July 2024, for an overall number of 27 observations. The monthly mean $\tau(0.500\mu m)$ values included a single measurement in April and June, and values ranging from 0.03 in July to 0.06 in August. Similar to other oceanic sectors, α values showed no significant variations, remaining between 1.20 and 1.40. The limited number of observations for this sector prevents any meaningful statistical or climatological analysis of aerosol extinction features.

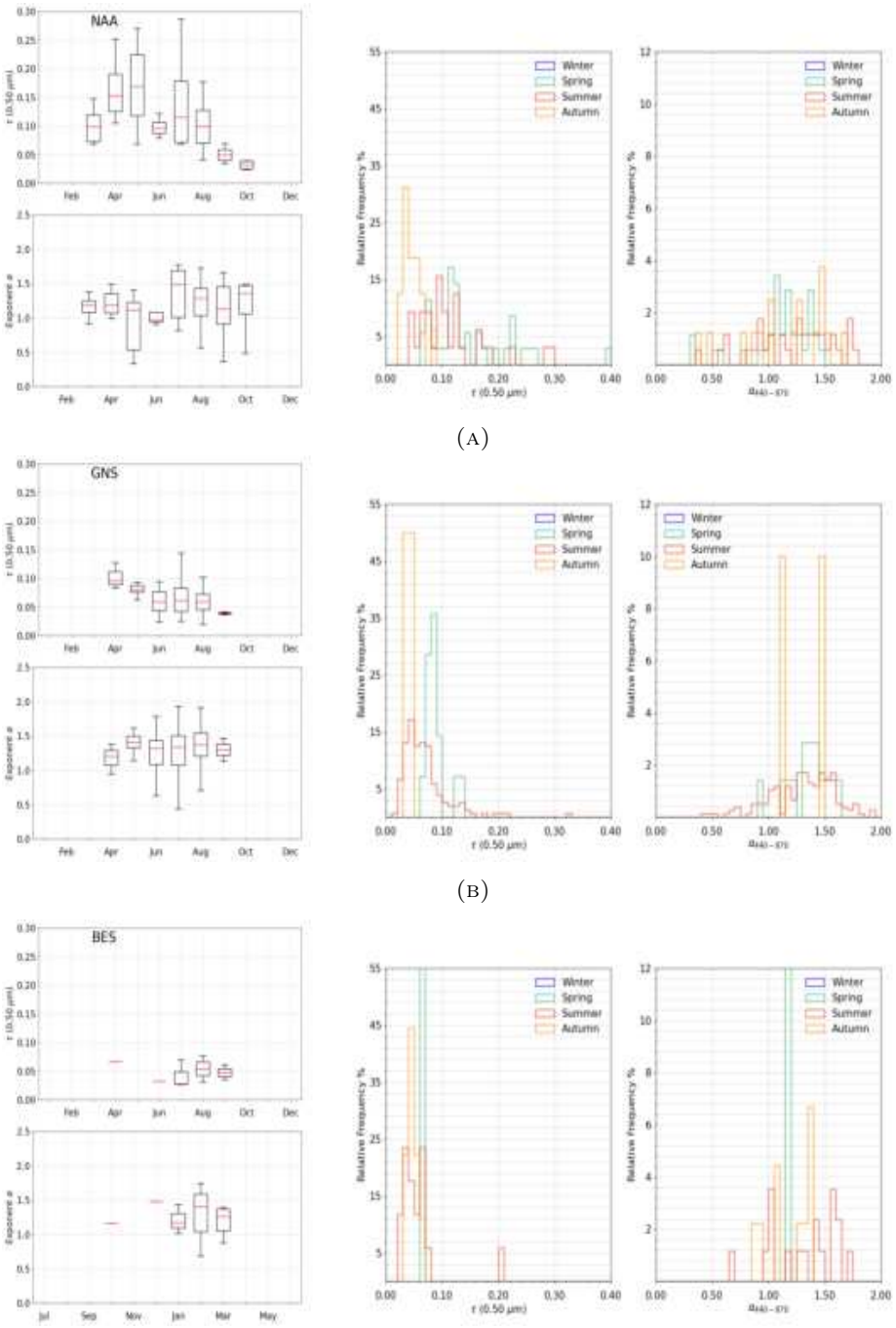

(A)

(B)

(C)

FIGURE 6.15: Multi-year sun-photometer measurements of aerosol optical depth $\tau(0.500\mu m)$ and exponent α conducted by several research institution during scientific cruises in the Arctic ocean between 2004 and 2024.

6.7.2 Antarctic Ocean

For Antarctica, the daily mean values of $\tau(0.500\mu m)$ and α, measured using the Microtops II sun-photometer aboard scientific vessels, were categorized into four sub-sectors (Table S2): (i) Southern Pacific Ocean (PAC), (ii) Antarctic Peninsula (APE), (iii) Southern Atlantic Ocean (ATL), and (iv) Southern Indian Ocean (IND). The number

of observations varied significantly between sectors, ranging from just 8 measurements in the APE sector to 376 measurements in the ATL sector. These differences should be considered when discussing the aerosol extinction features.

As shown in Table S2, thirty-nine cruises were conducted in the ATL sector from December 2007 to December 2020, collecting 376 measurements in total. The monthly mean values of $\tau(0.500\mu m)$ and α are presented in Fig. 6.16a. The AOD values remained stable from December to April, ranging between 0.02 and 0.03, which is close to the instrument's detection limit, with an average standard deviation of $\sigma = 0.01$. The monthly mean α values ranged from 1.20 in December to approximately 1.40 in February, with data dispersion decreasing from summer ($\sigma = 0.40$) to autumn ($\sigma = 0.33$). The RFH of $\tau(0.500\mu m)$ indicated AOD values between 0.01 and 0.10 across both seasons, while the α values showed a broader dispersion, ranging from 0.02 to 2.00.

Monthly mean values of $\tau(0.500\mu m)$ and α derived from 141 daily measurements performed during nineteen cruises made in the Southern Indian Ocean are shown in Fig. 6.16b. The monthly mean values of $\tau(0.500\mu m)$ exhibit a decreasing trend, from approximately 0.03 in December and January to 0.01 in April. The monthly mean α values follow a similar pattern to those in the ATL sector, ranging from about 1.40 in February to 1.00 in March. The RFH of $\tau(0.500\mu m)$ is also comparable to that of the ATL sector but with slightly less dispersion. However, the RFH of α shows a greater influence of larger particles, likely due to increased production of sea-salt particles.

As shown in Table 6.4, nine AERONET/MAN cruises were conducted in the Southern Pacific Ocean between January 2008 and December 2020, resulting in a total of 60 observations. The monthly mean values of $\tau(0.500\mu m)$ ranged from 0.04 in December to 0.09 in March, while the monthly mean α values decreased from approximately 1.40 in January to 1.00 in March. The RFHs indicate that almost all measurements were conducted during the summer season, with only a few taken in autumn. No observations were available for winter or spring.

Limited aerosol optical data were collected in the oceanic sector around the Antarctic Peninsula during three scientific cruises conducted between February 2009 and February 2014. As shown in Fig. 6.17b, only 8 measurements were recorded in this sector, all in February. The mean monthly values of $\tau(0.500\mu m)$ and α were 0.03 and 0.60, respectively, likely linked to the presence of sea-salt coarse particles transported from offshore areas of the Drake Passage (Posyniak and Markowicz 2009).

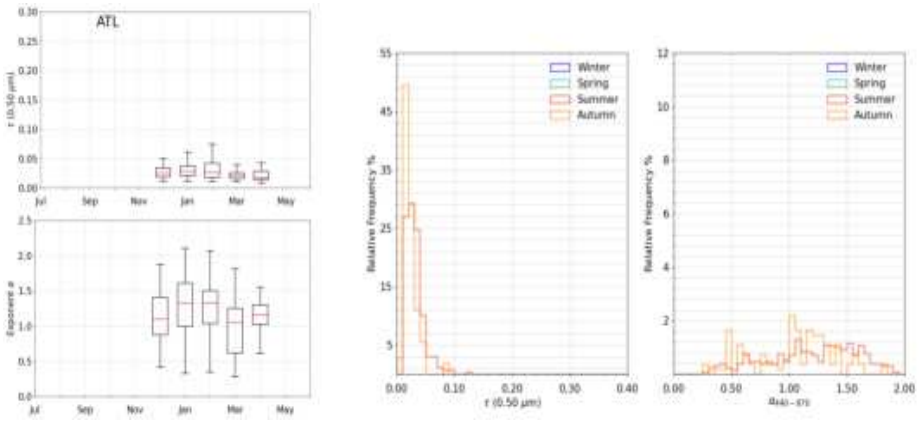

(A)

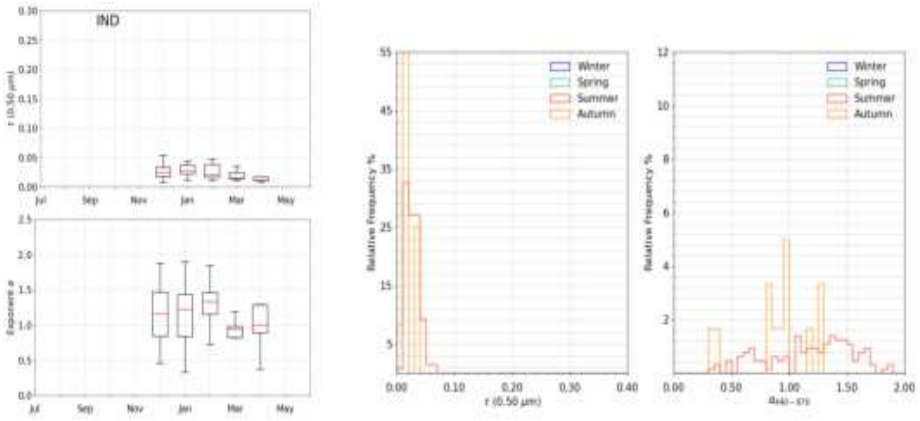

(B)

FIGURE 6.16: Multi-year sun-photometer measurements of aerosol optical depth $\tau(0.500\mu m)$ and exponent α conducted by several research institution during scientific cruises in the Antarctic ocean between 2004 and 2024.

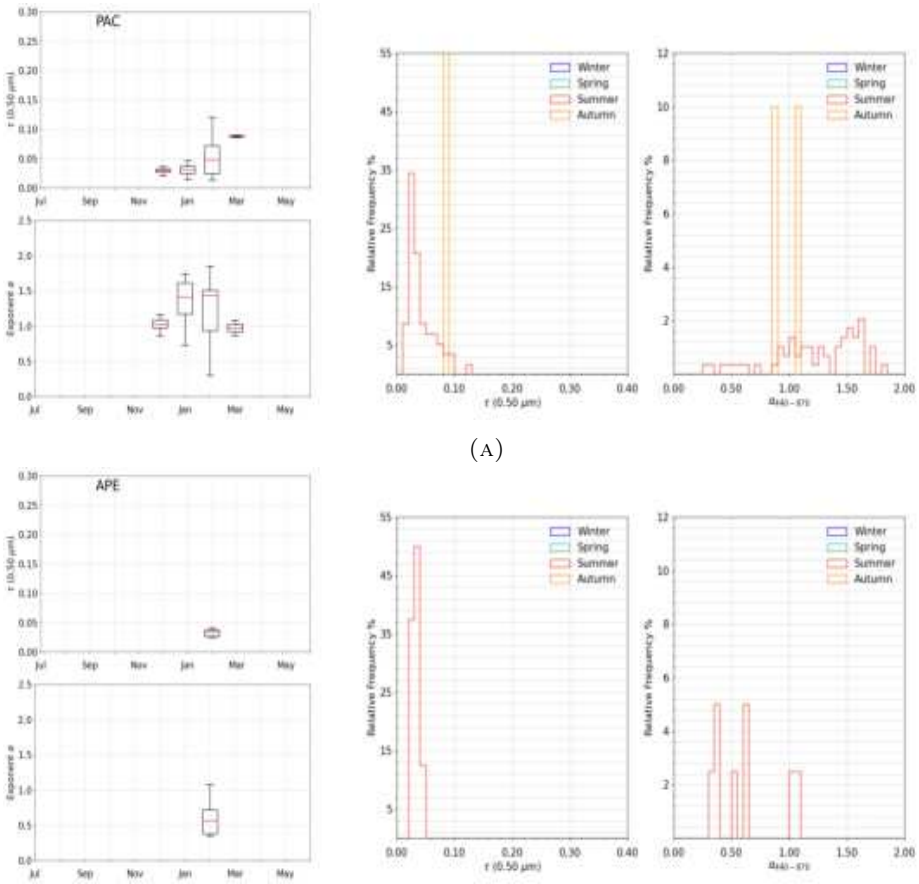

(A)

(B)

FIGURE 6.17: Multi-year sun-photometer measurements of aerosol optical depth $\tau(0.500\mu m)$ and exponent α conducted by several research institution during scientific cruises in the Antarctic ocean between 2004 and 2024.

6.8 Conclusions

Monthly mean values of $\tau(0.500\mu m)$ and the Ångström exponent α were determined from ground-based photometer measurements at 25 polar sites using either a sun-sky CE318 photometer or a sun-sky-lunar CE318-T photometer, both from CIMEL Electronique. Solar level 2 data and lunar level 1.5 data were downloaded directly from the AERONET website, merged into single files, and then processed. Other photometer models were also used in this study, with their characteristics described in previous sections. The results, presented by season, helped to better understand the seasonality of columnar aerosol extinction parameters and to study the evolution of these parameters over time, expanding on the work published by Tomasi et al. 2015.

A key feature of this study is the use of lunar photometry data alongside solar data. This innovative development allowed scientists to study atmospheric aerosols in polar regions even during the winter season, when there is no sunlight. This normally occurs from November to March in the Arctic and from May to October in Antarctica.

The panels in the upper part of Fig. 6.18 show observations conducted in the Arctic region, specifically in Alaska, Northern Canada, Greenland, Svalbard, and Northern Scandinavia. Unfortunately, due to the current global political situation, data from

stations in the Russian Arctic are missing. This is a major limitation for scientists studying aerosol evolution in this region, as Russia makes up nearly 40% of the Arctic.

The analysis of measurements from the 14 Arctic sites listed in Table 6.1 highlights the seasonality of columnar aerosol extinction parameters. The values of $\tau(0.500\mu m)$ were generally lower during the summer, ranging between 0.04 and 0.07, and higher during the winter, between 0.05 and 0.08. The exponent α also showed seasonal variation, with values ranging from 1.30 to 1.70 during summer-autumn and from 1.10 to 1.50 during winter-spring. These results align with the findings of Tomasi et al. 2015, but show slightly smaller values, indicating a cleaner atmosphere year-round, likely due to European and American regulations on anthropogenic emissions. Despite this decline, the typical seasonal aerosol behavior in the Arctic persists, with higher τ values during winter (accompanied by lower α coefficients) and lower τ values in summer (with higher α). This is due to the Arctic Haze phenomenon, caused by the transport of polluted air masses from industrialized and densely populated mid-latitude regions in Europe, Asia, and North America (Stock et al. 2014). Between April and May, the polar dome shrinks and move to higher latitudes, isolating the North Pole's atmosphere and making it cleaner, though wildfires are becoming more frequent and intense (Dall'Osto et al. 2019; Pulimeno et al. 2024; Zielinski et al. 2020). These effects are evident especially at sites in North America, Canada, and Greenland (see Fig. 6.3, 6.4, and 6.5), where the monthly mean values of $\tau(0.500\mu m)$ show significant variability, in particular during the summer season.

In Antarctica, sun- and lunar-photometer measurements were collected at 11 stations. Of these sites, 3 are coastal sites located on the Antarctic Peninsula, 6 are located a few kilometers inland in the Atlantic sector of Antarctica, and 2 are located on the ice sheet, at almost 3000 meters of altitude.

The lower panels of Figure 6.18 show that median $\tau(0.500\mu m)$ values ranged from less than 0.02 on the Antarctic Plateau to no more than 0.04 at the coastal stations. Escudero, located on King George Island which hosts 11 research stations (with approximately 700 beds), represents an exception for both seasons, with median $\tau(0.500\mu m)$ values around 0.08, while Juan Carlos I had data only for the summer of 2023. The exponent α decreased to around 1.00–1.50 during the austral summer and autumn, indicating aerosols mainly made up of fine-mode particles. However, at Escudero and Juan Carlos I, sea-salt coarse particles dominated the aerosol composition even in summer, probably due to the islands' large ice-free areas. During the winter-spring season, α values dropped to around 0.50-1.00, indicating aerosols dominated by coarse-mode particles. Notably, Vechernaya Hill station had unusually high α values during this period, with a median of 2.30. Compared to the findings of Tomasi et al. 2015, $\tau(0.500\mu m)$ values remained in the same range, except at the stations on the Antarctic Peninsula. However, α showed a negative trend, indicating an increase in coarse-mode particles influence in the atmosphere during both seasons. In addition to the measurements analyzed in this paper from Antarctica, there are also scattered observations from other stations, such as for example Bharati and Maitri, both managed by the National Centre for Polar and Ocean Research, India (Kannemadugu et al. 2023).

Ship-borne sun-photometer measurements using the Microtops II instrument were conducted onboard research vessels by various international institutions between 2004 and 2024 in different sectors of the Arctic and Antarctic Oceans.

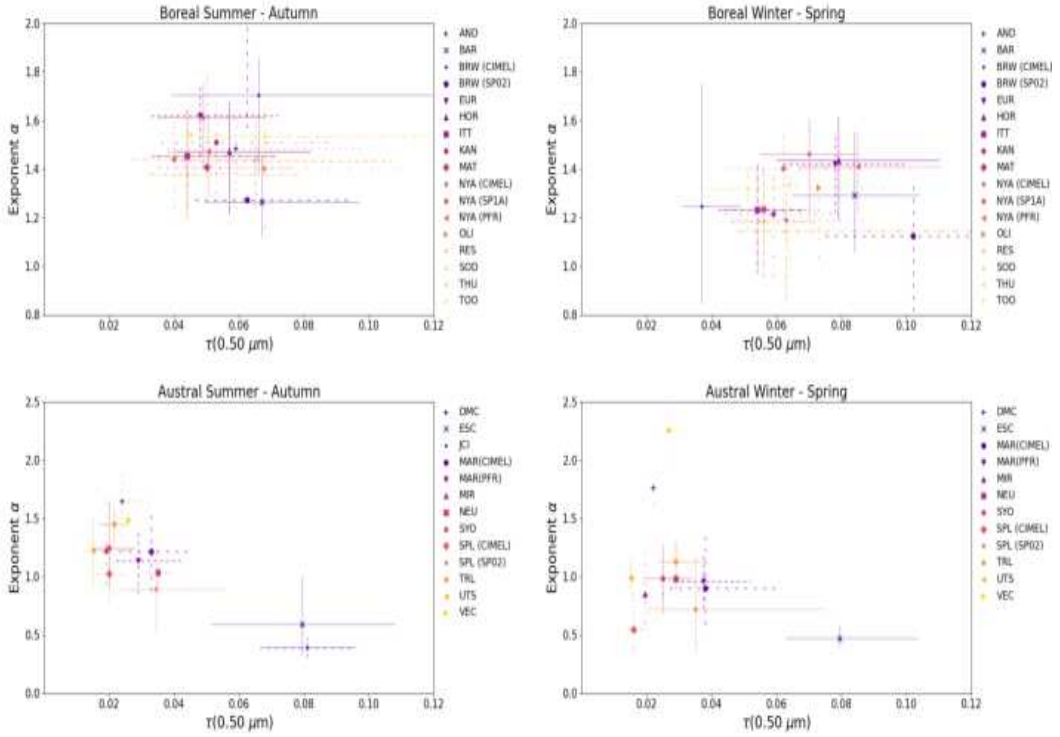

(A)

FIGURE 6.18: Upper part: Scatter plot shows the seasonal median values of the Ångström exponent α versus the corresponding seasonal median values of aerosol optical thickness $\tau(0.500\mu m)$, derived from sun- and lunar-photometer measurements at the polar sites listed in Table 6.1. The plot displays data for the Boreal summer-autumn and winter-spring seasons. The sites include Andenes (AND), Barentsburg (BAR), Barrow (BRW), Eureka OPAL (EUR), Hornsund (HOR), Ittoqqortoormiit (ITT), Kangerlussuaq (KAN), Matorova (MAT), Ny-Ålesund (NYA), Oliktok (OLI), Resolute Bay (RES), Sodankylå (SOD), Thule (THU), and Toolik Lake (TOO). In the upper-left panel, colored symbols represent summer–autumn results, while the upper-right panel shows winter–spring results. Vertical and horizontal dashed bars indicate the 25th and 75th percentiles. Lower part: Similar scatter plots are shown for sun- and lunar-photometer measurements at Antarctic sites listed in Table 6.2 during the Austral summer-autumn and winter-spring seasons. The sites include DomeC (DMC), Escudero (ESC), Juan Carlos I (JCI), Marambio (MAR), Mirny (MIR), Neumayer (NEU), Syowa (SYO), South Pole (SPL), Troll/Trollhaugen (TRL), Utsteinen (UTS), and Vechernaya Hill (VEC). The lower-left panel shows the summer–autumn results, while the lower-right panel displays the winter–spring results.

Analysis of data from forty-seven AERONET-MAN cruises in three Arctic oceanic sectors revealed that the monthly mean values of $\tau(0.50\mu m)$ ranged from 0.04 to 0.17 between March and October, as measurements were only available during periods of daylight. The higher AOD levels observed during the spring season, particularly in the NAA sector, were attributed to the intrusion of polluted air masses into the Arctic atmosphere. As expected, the typical seasonal AOD pattern observed at ground station, consisting in higher values in winter-spring and lower values in summer-autumn, is also evident in these oceanic sectors. Installing CIMEL sun-sky-lunar instruments

on research vessels in the future would enable observations during the polar night, addressing the current gaps in data coverage.

In the four Antarctic oceanic sectors, aerosol extinction parameter analysis from seventy AERONET-MAN cruises conducted between 2004 and 2024 showed that monthly mean values of $\tau(0.50\mu m)$ ranged from 0.01 to 0.09. These values are approximately half the magnitude recorded in the Arctic Ocean and fall within the Microtops II instrumental uncertainty of 0.02. Due to the manual nature of these measurements and the extreme environmental conditions in Antarctica, observations were further restricted to the austral summer and autumn (December to April), when daylight permitted.

In addition to characterizing the seasonal variability of aerosol extinction parameters, this study also investigated long-term trends in $\tau(0.500\mu m)$ at selected Arctic and Antarctic AERONET sites. The trend analysis revealed a statistically significant decrease at Andenes, where aerosol optical depth declined by 2.43% per year, likely due to stricter emission regulations in Europe. In contrast, Syowa and South Pole exhibited increasing trends, with aerosol optical depth rising by 3.84% and 3.54% per year, respectively. However, the robustness of these results is limited by data availability and changes in instrumentation over time. These findings highlight the importance of continuous and standardized long-term observations to improve the understanding of aerosol trends in polar regions.

This paper aimed to understand and describe aerosol trends at both poles through a multi-year time series analysis at several stations. Although we focused mainly on AERONET sites, as CIMEL procedures are considered the most comprehensive for sun-sky-lunar measurements, other photometer models are also capable of capturing aerosol behavior in these challenging polar environments (Mazzola et al. 2024).

This work investigates the AOD variability across polar observational networks, and in order to understand the atmospheric processes linked with aerosol distributions in the Arctic and Antarctic regions. In the Arctic, pronounced maximum seasonal AOD during winter and early spring is consistent with the well-documented Arctic haze phenomenon, attributable to enhanced transport of mid-latitude anthropogenic emissions. Stations including Barrow, Eureka, and Ny-Ålesund demonstrated these characteristic patterns, further accentuated in recent years by high AOD, low α cases, indicating biomass-burning aerosols associated with intensified boreal wildfire activity. In addition, Greenland stations, notably Thule and Kangerlussuaq, reported spring and summer AOD enhancements, showing the significance of Arctic haze intrusions and episodic high AOD events. Measuring sites in Scandinavia (Andenes and Sodankylä), exhibited lower seasonal variability, possibly due to the proximity to continental emissions and maritime aerosol sources. Antarctic observations revealed summer conditions dominated by smaller, fine-mode aerosols, whereas winter and spring seasons exhibited a shift toward coarse-mode particles, likely resulting from sea-spray aerosols. Positive AOD trends at Antarctic stations such as Syowa and the South Pole have been reported that further indicates potential shifts in aerosol source regions and transport pathways.

These findings show the crucial role of sustained, high-precision aerosol monitoring in polar environments, essential for our understanding of aerosol–effects in the context of the increased anthropogenic pressures to the Earths climate. Future works could expand this study by including more stations, field campaigns, and ship-borne campaigns using different photometer models at both poles. Currently, the biggest limitation is the uneven distribution of stations and measurements. In the Arctic, the Russian sector remains a black box. Since it makes up almost 40% of the Arctic,

studying this area is crucial for a better understanding of aerosol climatology. In Antarctica, most stations are located in the Antarctic Peninsula and Atlantic sector. A wider distribution of photometric instruments across other regions would help improve coverage of the entire continent.

Bibliography

AboEl-Fetouh, Y., O'Neill, N. T., Ranjbar, K., Hesaraki, S., Abboud, I., and Sobolewski, P. S. (2020). Climatological-Scale Analysis of Intensive and Semi-intensive Aerosol Parameters Derived From AERONET Retrievals Over the Arctic. *Journal of Geophysical Research: Atmospheres*, 125(10):e2019JD031569. _eprint: https://onlinelibrary.wiley.com/doi/pdf/10.1029/2019JD031569.

Alexandrov, M. D., Marshak, A., Cairns, B., Lacis, A. A., and Carlson, B. E. (2004). Automated cloud screening algorithm for MFRSR data. *Geophysical Research Letters*, 31(4). _eprint: https://onlinelibrary.wiley.com/doi/pdf/10.1029/2003GL019105.

Asmi, E., , Kimmo, N., , Kimmo, T., , Edith, R., , Aki, V., , John, B., , Matthew, B., , Jesse, J., , Heikki, L., , Gerrit, d. L., , Jussi, P., , Veijo, A., , Miguel, M., , Gonzalo, G., , Gustavo, C., , Marco, A., , Germán Pérez, F., , Jonathan, F., , María Elena, B., , and Sánchez, R. (2018). Primary sources control the variability of aerosol optical properties in the Antarctic Peninsula. *Tellus B: Chemical and Physical Meteorology*, 70(1):1–16. Publisher: Taylor & Francis.

Barreto, A., Cuevas, E., Damiri, B., Guirado, C., Berkoff, T., Berjón, A. J., Hernández, Y., Almansa, F., and Gil, M. (2013). A new method for nocturnal aerosol measurements with a lunar photometer prototype. *Atmospheric Measurement Techniques*, 6(3):585–598. Publisher: Copernicus GmbH.

Cordero, R. R., Sepúlveda, E., Feron, S., Damiani, A., Fernandoy, F., Neshyba, S., Rowe, P. M., Asencio, V., Carrasco, J., Alfonso, J. A., Llanillo, P., Wachter, P., Seckmeyer, G., Stepanova, M., Carrera, J. M., Jorquera, J., Wang, C., Malhotra, A., Dana, J., Khan, A. L., and Casassa, G. (2022). Black carbon footprint of human presence in Antarctica. *Nature Communications*, 13(1):984. Publisher: Nature Publishing Group.

Dall'Osto, M., Beddows, D. C. S., Tunved, P., Harrison, R. M., Lupi, A., Vitale, V., Becagli, S., Traversi, R., Park, K.-T., Yoon, Y. J., Massling, A., Skov, H., Lange, R., Strom, J., and Krejci, R. (2019). Simultaneous measurements of aerosol size distributions at three sites in the European high Arctic. *Atmospheric Chemistry and Physics*, 19(11):7377–7395. Publisher: Copernicus GmbH.

Eck, T. F., Holben, B. N., Reid, J. S., Dubovik, O., Smirnov, A., O'Neill, N. T., Slutsker, I., and Kinne, S. (1999). Wavelength dependence of the optical depth of biomass burning, urban, and desert dust aerosols. *Journal of Geophysical Research*, 104:31,333–31,349. ADS Bibcode: 1999JGR...10431333E.

Eck, T. F., Holben, B. N., Sinyuk, A., Pinker, R. T., Goloub, P., Chen, H., Chatenet, B., Li, Z., Singh, R. P., Tripathi, S. N., Reid, J. S., Giles, D. M.,

Dubovik, O., O'Neill, N. T., Smirnov, A., Wang, P., and Xia, X. (2010). Climatological aspects of the optical properties of fine/coarse mode aerosol mixtures. *Journal of Geophysical Research: Atmospheres*, 115(D19). _eprint: https://onlinelibrary.wiley.com/doi/pdf/10.1029/2010JD014002.

Engelmann, R., Ansmann, A., Ohneiser, K., Griesche, H., Radenz, M., Hofer, J., Althausen, D., Dahlke, S., Maturilli, M., Veselovskii, I., Jimenez, C., Wiesen, R., Baars, H., Bühl, J., Gebauer, H., Haarig, M., Seifert, P., Wandinger, U., and Macke, A. (2021). Wildfire smoke, Arctic haze, and aerosol effects on mixed-phase and cirrus clouds over the North Pole region during MOSAiC: an introduction. *Atmospheric Chemistry and Physics*, 21(17):13397–13423. Publisher: Copernicus GmbH.

Fiebig, M., Hirdman, D., Lunder, C. R., Ogren, J. A., Solberg, S., Stohl, A., and Thompson, R. L. (2014). Annual cycle of Antarctic baseline aerosol: controlled by photooxidation-limited aerosol formation. *Atmospheric Chemistry and Physics*, 14(6):3083–3093. Publisher: Copernicus GmbH.

Fiebig, M., Lunder, C. R., and Stohl, A. (2009). Tracing biomass burning aerosol from South America to Troll Research Station, Antarctica. *Geophysical Research Letters*, 36:L14815. ADS Bibcode: 2009GeoRL..3614815F.

Giles, D. M., Sinyuk, A., Sorokin, M. G., Schafer, J. S., Smirnov, A., Slutsker, I., Eck, T. F., Holben, B. N., Lewis, J. R., Campbell, J. R., Welton, E. J., Korkin, S. V., and Lyapustin, A. I. (2019). Advancements in the Aerosol Robotic Network (AERONET) Version 3 database – automated near-real-time quality control algorithm with improved cloud screening for Sun photometer aerosol optical depth (AOD) measurements. *Atmospheric Measurement Techniques*, 12(1):169–209. Publisher: Copernicus GmbH.

González, R., Toledano, C., Román, R., Fuertes, D., Berjón, A., Mateos, D., Guirado-Fuentes, C., Velasco-Merino, C., Antuña-Sánchez, J. C., Calle, A., Cachorro, V. E., and de Frutos, Á. M. (2020). Daytime and nighttime aerosol optical depth implementation in CÆLIS. *Geoscientific Instrumentation, Methods and Data Systems*, 9(2):417–433. Publisher: Copernicus GmbH.

Hirdman, D., Sodemann, H., Eckhardt, S., Burkhart, J. F., Jefferson, A., Mefford, T., Quinn, P. K., Sharma, S., Ström, J., and Stohl, A. (2010). Source identification of short-lived air pollutants in the Arctic using statistical analysis of measurement data and particle dispersion model output. *Atmospheric Chemistry and Physics*, 10(2):669–693. Publisher: Copernicus GmbH.

Holben, B. N., Eck, T. F., Slutsker, I., Tanré, D., Buis, J. P., Setzer, A., Vermote, E., Reagan, J. A., Kaufman, Y. J., Nakajima, T., Lavenu, F., Jankowiak, I., and Smirnov, A. (1998). AERONET—A Federated Instrument Network and Data Archive for Aerosol Characterization. *Remote Sensing of Environment*, 66(1):1–16.

Intergovernmental Panel on Climate Change (IPCC) (2023). *Climate Change 2021 – The Physical Science Basis: Working Group I Contribution to the Sixth Assessment Report of the Intergovernmental Panel on Climate Change*. Cambridge University Press, Cambridge.

Iqbal, M. (1983). *An introduction to solar radiation*. Academic Press.

Jain, P., Barber, Q. E., Taylor, S. W., Whitman, E., Castellanos Acuna, D., Boulanger, Y., Chavardès, R. D., Chen, J., Englefield, P., Flannigan, M., Girardin, M. P., Hanes, C. C., Little, J., Morrison, K., Skakun, R. S., Thompson, D. K., Wang, X., and Parisien, M.-A. (2024). Drivers and Impacts of the Record-Breaking 2023 Wildfire Season in Canada. *Nature Communications*, 15(1):6764. Publisher: Nature Publishing Group.

Kabanov, D. M., Maslovsky, A. S., Radionov, V. F., Sakerin, S. M., Sidorova, O. R., and Chernov, D. G. (2023). Seasonal and Interannual Variability of Aerosol Characteristics According to the Data of Long-Term (2011–2021) Measurements at the Russian Scientific Center on the Spitzbergen Archipelago. *Atmospheric and Oceanic Optics*, 36(6):645–654.

Kannemadugu, H. B. S., Sudhakaran Syamala, P., Taori, A., Bothale, R. V., and Chauhan, P. (2023). Atmospheric aerosol optical properties and trends over Antarctica using in-situ measurements and MERRA-2 aerosol products. *Polar Science*, 38:101011.

Kaskaoutis, D. G., Kambezidis, H. D., Hatzianastassiou, N., Kosmopoulos, P. G., and Badarinath, K. V. S. (2007). Aerosol climatology: dependence of the Angstrom exponent on wavelength over four AERONET sites. *Atmospheric Chemistry and Physics Discussions*, 7(3):7347–7397. Publisher: Copernicus GmbH.

Kazadzis, S., Kouremeti, N., Nyeki, S., Gröbner, J., and Wehrli, C. (2018). The World Optical Depth Research and Calibration Center (WORCC) quality assurance and quality control of GAW-PFR AOD measurements. *Geoscientific Instrumentation, Methods and Data Systems*, 7(1):39–53. Publisher: Copernicus GmbH.

Kendall, M. G. (1955). Rank correlation methods. *Oxford University Press*, 4.

Kieffer, H. H. and Stone, T. C. (2005). The Spectral Irradiance of the Moon. *The Astronomical Journal*, 129(6):2887. Publisher: IOP Publishing.

Kim, S.-W., Jefferson, A., Yoon, S.-C., Dutton, E. G., Ogren, J. A., Valero, F. P. J., Kim, J., and Holben, B. N. (2005). Comparisons of aerosol optical depth and surface shortwave irradiance and their effect on the aerosol surface radiative forcing estimation. *Journal of Geophysical Research: Atmospheres*, 110(D7). _eprint: https://onlinelibrary.wiley.com/doi/pdf/10.1029/2004JD004989.

Klonecki, A., Hess, P., Emmons, L., Smith, L., Orlando, J., and Blake, D. (2003). Seasonal changes in the transport of pollutants into the Arctic troposphere-model study. *Journal of Geophysical Research: Atmospheres*, 108(D4). _eprint: https://onlinelibrary.wiley.com/doi/pdf/10.1029/2002JD002199.

Mann, H. B. (1945). Nonparametric Tests Against Trend. *Econometrica*, 13(3):245–259. Publisher: [Wiley, Econometric Society].

Mazzola, M., Lanconelli, C., Lupi, A., Busetto, M., Vitale, V., and Tomasi, C. (2010). Columnar aerosol optical properties in the Po Valley, Italy, from MFRSR data. *Journal of Geophysical Research: Atmospheres*, 115(D17). _eprint: https://onlinelibrary.wiley.com/doi/pdf/10.1029/2009JD013310.

Mazzola, M., Stone, R. S., Herber, A., Tomasi, C., Lupi, A., Vitale, V., Lanconelli, C., Toledano, C., Cachorro, V. E., O'Neill, N. T., Shiobara, M., Aaltonen, V.,

Stebel, K., Zielinski, T., Petelski, T., Ortiz de Galisteo, J. P., Torres, B., Berjon, A., Goloub, P., Li, Z., Blarel, L., Abboud, I., Cuevas, E., Stock, M., Schulz, K. H., and Virkkula, A. (2012). Evaluation of sun photometer capabilities for retrievals of aerosol optical depth at high latitudes: The POLAR-AOD intercomparison campaigns. *Atmospheric Environment*, 52:4–17.

Mazzola, M., Stone, R. S., Kouremeti, N., Vitale, V., Gröbner, J., Stebel, K., Hansen, G. H., Stone, T. C., Ritter, C., and Pulimeno, S. (2024). Monitoring aerosol optical depth during the Arctic night: Instrument development and first results. *Atmospheric Research*, 311:107667.

McArthur, L. J. B. (2005). World Climate Research Programme - Baseline Surface Radiation Network (BSRN) - Operations Manual Version 2.1. Place: Downsview, Ontario, CANADA Publisher: Experimental Studies Division, Atmospheric Environment Service.

Nakajima, T., Campanelli, M., Che, H., Estellés, V., Irie, H., Kim, S.-W., Kim, J., Liu, D., Nishizawa, T., Pandithurai, G., Soni, V. K., Thana, B., Tugjsurn, N.-U., Aoki, K., Go, S., Hashimoto, M., Higurashi, A., Kazadzis, S., Khatri, P., Kouremeti, N., Kudo, R., Marenco, F., Momoi, M., Ningombam, S. S., Ryder, C. L., Uchiyama, A., and Yamazaki, A. (2020). An overview of and issues with sky radiometer technology and SKYNET. *Atmospheric Measurement Techniques*, 13(8):4195–4218. Publisher: Copernicus GmbH.

Ohneiser, K., Ansmann, A., Chudnovsky, A., Engelmann, R., Ritter, C., Veselovskii, I., Baars, H., Gebauer, H., Griesche, H., Radenz, M., Hofer, J., Althausen, D., Dahlke, S., and Maturilli, M. (2021). The unexpected smoke layer in the High Arctic winter stratosphere during MOSAiC 2019–2020. *Atmospheric Chemistry and Physics*, 21(20):15783–15808. Publisher: Copernicus GmbH.

O'Neill, N. T., Baibakov, K., Hesaraki, S., Ivanescu, L., Martin, R. V., Perro, C., Chaubey, J. P., Herber, A., and Duck, T. J. (2016). Temporal and spectral cloud screening of polar winter aerosol optical depth (AOD): impact of homogeneous and inhomogeneous clouds and crystal layers on climatological-scale AODs. *Atmospheric Chemistry and Physics*, 16(19):12753–12765. Publisher: Copernicus GmbH.

Posyniak, M. and Markowicz, K. (2009). Measurement of aerosol optical thickness over the Atlantic Ocean and in West Antarctica, 2006–2007. *Acta Geophysica*, 57(2):494–508.

Pulimeno, S., Bruschi, F., Feltracco, M., Mazzola, M., Gilardoni, S., Crocchianti, S., Cappelletti, D., Gambaro, A., and Barbaro, E. (2024). Investigating the Presence of Biomass Burning Events at Ny-Ålesund: Optical and Chemical Insights from Summer-Fall 2019. *Atmospheric Environment*, 320:120336.

Quinn, P. K., , G., S., , E., A., , E. G., D., , T., R.-A., , and Gong, S. L. (2007). Arctic haze: current trends and knowledge gaps. *Tellus B: Chemical and Physical Meteorology*, 59(1):99–114. Publisher: Taylor & Francis _eprint: https://doi.org/10.1111/j.1600-0889.2006.00236.x.

Raatz, W. E., Schnell, R. C., Bodhaine, B. A., and Oltmans, S. J. (1985). Observations of Arctic haze during polar flights from Alaska to Norway. *Atmospheric Environment (1967)*, 19(12):2143–2151.

Rodríguez, E., Toledano, C., Cachorro, V., De Leeuw, G., De Frutos, A., Gausa, M., and Holben, B. (2012). Comparison of aerosol optical properties at the sub-arctic stations ALOMAR-Andenes, Abisko and Sodankylä in late spring and summer 2007. *Atmospheric Research*, 107:20–30.

Román, R., González, R., Toledano, C., Barreto, Á., Pérez-Ramírez, D., Benavent-Oltra, J. A., Olmo, F. J., Cachorro, V. E., Alados-Arboledas, L., and de Frutos, Á. M. (2020). Correction of a lunar-irradiance model for aerosol optical depth retrieval and comparison with a star photometer. *Atmospheric Measurement Techniques*, 13(11):6293–6310. Publisher: Copernicus GmbH.

Sakerin, S., Kabanov, D., Rostov, A., Turchinovich, S., and Knyazev, V. (2013). Sun photometers for measuring spectral air transparency in stationary and mobile conditions. *Atmospheric and Oceanic Optics*, 26:352–356.

Sen, P. K. (1968). Estimates of the Regression Coefficient Based on Kendall's Tau. *Journal of the American Statistical Association*, 63(324):1379–1389. Publisher: ASA Website _eprint: https://www.tandfonline.com/doi/pdf/10.1080/01621459.1968.10480934.

Sharma, S., Andrews, E., Barrie, L. A., Ogren, J. A., and Lavoué, D. (2006). Variations and sources of the equivalent black carbon in the high Arctic revealed by long-term observations at Alert and Barrow: 1989–2003. *Journal of Geophysical Research: Atmospheres*, 111(D14). _eprint: https://onlinelibrary.wiley.com/doi/pdf/10.1029/2005JD006581.

Shaw, G. E. (1976). Error analysis of multi-wavelength sun photometry. *pure and applied geophysics*, 114(1):1–14.

Shaw, G. E. (1983). Sun Photometry. *Bulletin of the American Meteorological Society*, 64:4–10. Publisher: AMS ADS Bibcode: 1983BAMS...64....4S.

Shaw, G. E. (1995). The Arctic Haze Phenomenon. *Bulletin of the American Meteorological Society*, 76. Section: Bulletin of the American Meteorological Society.

Sheridan, P. (2015). Aerosol Measurements at South Pole: Climatology and Impact of Local Contamination. *Aerosol and Air Quality Research*, 16.

Smirnov, A., Holben, B. N., Giles, D. M., Slutsker, I., O'Neill, N. T., Eck, T. F., Macke, A., Croot, P., Courcoux, Y., Sakerin, S. M., Smyth, T. J., Zielinski, T., Zibordi, G., Goes, J. I., Harvey, M. J., Quinn, P. K., Nelson, N. B., Radionov, V. F., Duarte, C. M., Losno, R., Sciare, J., Voss, K. J., Kinne, S., Nalli, N. R., Joseph, E., Krishna Moorthy, K., Covert, D. S., Gulev, S. K., Milinevsky, G., Larouche, P., Belanger, S., Horne, E., Chin, M., Remer, L. A., Kahn, R. A., Reid, J. S., Schulz, M., Heald, C. L., Zhang, J., Lapina, K., Kleidman, R. G., Griesfeller, J., Gaitley, B. J., Tan, Q., and Diehl, T. L. (2011). Maritime aerosol network as a component of AERONET – first results and comparison with global aerosol models and satellite retrievals. *Atmospheric Measurement Techniques*, 4(3):583–597. Publisher: Copernicus GmbH.

Smirnov, A., Holben, B. N., Slutsker, I., Giles, D. M., McClain, C. R., Eck, T. F., Sakerin, S. M., Macke, A., Croot, P., Zibordi, G., Quinn, P. K., Sciare, J., Kinne, S., Harvey, M., Smyth, T. J., Piketh, S., Zielinski, T., Proshutinsky, A., Goes, J. I., Nelson, N. B., Larouche, P., Radionov, V. F.,

Goloub, P., Krishna Moorthy, K., Matarrese, R., Robertson, E. J., and Jourdin, F. (2009). Maritime Aerosol Network as a component of Aerosol Robotic Network. *Journal of Geophysical Research: Atmospheres*, 114(D6). _eprint: https://onlinelibrary.wiley.com/doi/pdf/10.1029/2008JD011257.

Sofieva, V. F., Rozanov, A., Szelag, M., Burrows, J. P., Retscher, C., Damadeo, R., Degenstein, D., Rieger, L. A., and Bourassa, A. (2024). CREST: a Climate Data Record of Stratospheric Aerosols. *Earth System Science Data*, 16(11):5227–5241. Publisher: Copernicus GmbH.

Stock, M., , Christoph, R., , Veijo, A., , Wenche, A., , DõRthe, H., , Andreas, H., , Renate, T., , and Dethloff, K. (2014). Where does the optically detectable aerosol in the European Arctic come from? *Tellus B: Chemical and Physical Meteorology*, 66(1):21450. Publisher: Taylor & Francis _eprint: https://doi.org/10.3402/tellusb.v66.21450.

Stohl, A. (2006). Characteristics of atmospheric transport into the Arctic troposphere. *Journal of Geophysical Research: Atmospheres*, 111(D11). _eprint: https://onlinelibrary.wiley.com/doi/pdf/10.1029/2005JD006888.

Theil, H. (1992). A Rank-Invariant Method of Linear and Polynomial Regression Analysis. In Raj, B. and Koerts, J., editors, *Henri Theil's Contributions to Economics and Econometrics: Econometric Theory and Methodology*, pages 345–381. Springer Netherlands, Dordrecht.

Toledano, C., Cachorro, V., Gausa, M., Stebel, K., Aaltonen, V., Berjón, A., Ortiz De Galisteo, J., De Frutos, A., Bennouna, Y., Blindheim, S., Myhre, C., Zibordi, G., Wehrli, C., Kratzer, S., Hakansson, B., Carlund, T., De Leeuw, G., Herber, A., and Torres, B. (2012). Overview of sun photometer measurements of aerosol properties in Scandinavia and Svalbard. *Atmospheric Environment*, 52:18–28.

Tomasi, C., Kokhanovsky, A. A., Lupi, A., Ritter, C., Smirnov, A., O'Neill, N. T., Stone, R. S., Holben, B. N., Nyeki, S., Wehrli, C., Stohl, A., Mazzola, M., Lanconelli, C., Vitale, V., Stebel, K., Aaltonen, V., de Leeuw, G., Rodriguez, E., Herber, A. B., Radionov, V. F., Zielinski, T., Petelski, T., Sakerin, S. M., Kabanov, D. M., Xue, Y., Mei, L., Istomina, L., Wagener, R., McArthur, B., Sobolewski, P. S., Kivi, R., Courcoux, Y., Larouche, P., Broccardo, S., and Piketh, S. J. (2015). Aerosol remote sensing in polar regions. *Earth-Science Reviews*, 140:108–157.

Tomasi, C., Lupi, A., Mazzola, M., Stone, R. S., Dutton, E. G., Herber, A., Radionov, V. F., Holben, B. N., Sorokin, M. G., Sakerin, S. M., Terpugova, S. A., Sobolewski, P. S., Lanconelli, C., Petkov, B. H., Busetto, M., and Vitale, V. (2012). An update on polar aerosol optical properties using POLAR-AOD and other measurements performed during the International Polar Year. *Atmospheric Environment*, 52:29–47.

Tomasi, C., Vitale, V., Lupi, A., Di Carmine, C., Campanelli, M., Herber, A., Treffeisen, R., Stone, R. S., Andrews, E., Sharma, S., Radionov, V., von Hoyningen-Huene, W., Stebel, K., Hansen, G. H., Myhre, C. L., Wehrli, C., Aaltonen, V., Lihavainen, H., Virkkula, A., Hillamo, R., Ström, J., Toledano, C., Cachorro, V. E., Ortiz, P., de Frutos, A. M., Blindheim, S., Frioud, M., Gausa,

M., Zielinski, T., Petelski, T., and Yamanouchi, T. (2007). Aerosols in polar regions: A historical overview based on optical depth and in situ observations. *Journal of Geophysical Research: Atmospheres*, 112(D16). _eprint: https://onlinelibrary.wiley.com/doi/pdf/10.1029/2007JD008432.

Vernier, J.-P., Aubry, T. J., Timmreck, C., Schmidt, A., Clarisse, L., Prata, F., Theys, N., Prata, A. T., Mann, G., Choi, H., Carn, S., Rigby, R., Loughlin, S. C., and Stevenson, J. A. (2024). The 2019 Raikoke eruption as a testbed used by the Volcano Response group for rapid assessment of volcanic atmospheric impacts. *Atmospheric Chemistry and Physics*, 24(10):5765–5782. Publisher: Copernicus GmbH.

Vernier, J.-P., Thomason, L. W., Pommereau, J.-P., Bourassa, A., Pelon, J., Garnier, A., Hauchecorne, A., Blanot, L., Trepte, C., Degenstein, D., and Vargas, F. (2011). Major influence of tropical volcanic eruptions on the stratospheric aerosol layer during the last decade. *Geophysical Research Letters*, 38(12). _eprint: https://onlinelibrary.wiley.com/doi/pdf/10.1029/2011GL047563.

Warneke, C., Bahreini, R., Brioude, J., Brock, C. A., de Gouw, J. A., Fahey, D. W., Froyd, K. D., Holloway, J. S., Middlebrook, A., Miller, L., Montzka, S., Murphy, D. M., Peischl, J., Ryerson, T. B., Schwarz, J. P., Spackman, J. R., and Veres, P. (2009). Biomass burning in Siberia and Kazakhstan as an important source for haze over the Alaskan Arctic in April 2008. *Geophysical Research Letters*, 36(2). _eprint: https://onlinelibrary.wiley.com/doi/pdf/10.1029/2008GL036194.

Wehrli, C. (2000). Calibrations of filter radiometers for determination of atmospheric optical depth. *Metrologia*, 37(5):419.

Welch, A. M., Matthews, T., Sheesley, R. J., Wang, H., Barsanti, K. C., Nielsen, N., Xu, X., Niu, L., Guenther, A. B., and Czimczik, C. I. (2025). Summertime Carbonaceous Aerosol in Interior Versus Coastal Northern Alaska. *Journal of Geophysical Research: Atmospheres*, 130(8):e2024JD042080. _eprint: https://onlinelibrary.wiley.com/doi/pdf/10.1029/2024JD042080.

Xian, P., Zhang, J., O'Neill, N. T., Toth, T. D., Sorenson, B., Colarco, P. R., Kipling, Z., Hyer, E. J., Campbell, J. R., Reid, J. S., and Ranjbar, K. (2022). Arctic spring and summertime aerosol optical depth baseline from long-term observations and model reanalyses – Part 1: Climatology and trend. *Atmospheric Chemistry and Physics*, 22(15):9915–9947. Publisher: Copernicus GmbH.

Zielinski, T., Bolzacchini, E., Cataldi, M., Ferrero, L., Graßl, S., Hansen, G., Mateos, D., Mazzola, M., Neuber, R., Pakszys, P., Posyniak, M., Ritter, C., Severi, M., Sobolewski, P., Traversi, R., and Velasco-Merino, C. (2020). Study of Chemical and Optical Properties of Biomass Burning Aerosols during Long-Range Transport Events toward the Arctic in Summer 2017. *Atmosphere*, 11:84.

Chapter 7

Conclusions

The research presented in this thesis provides a comprehensive assessment of aerosol behavior in polar regions, addressing long-standing gaps in the understanding of seasonal variability, sources, composition, and long-term trends. By integrating ground-based, ship-borne, and by combining optical and chemical analyses with trajectory modeling, this work has advanced both methodological approaches and scientific knowledge of polar aerosols. A central challenge in polar aerosol research is the lack of continuous observations, particularly during the polar night when solar radiation is absent. This limitation was overcome through the innovative adaptation of sun photometers to lunar photometry, demonstrating that nighttime aerosol optical depth measurements are reliable and consistent with solar photometry. This methodological development has allowed for the generation of year-round AOD datasets at Arctic and Antarctic stations, filling critical observational gaps.

The first manuscript highlighted the utility of a multi-disciplinary approach to identify subtle aerosol pollution events at Svalbard, Norway. Despite the absence of strong wildfire signals in hourly optical measurements, twelve mild pollution events were detected, originating primarily from North America during the summer and shifting to Euro-Asian sources in late autumn. Positive matrix factorization revealed five distinct aerosol sources, demonstrating the predominance of sea salt in coarse particles, the significant contribution of anthropogenic sulfate in fine particles, and the presence of biogenic aerosols during the light season. Even the minor biomass burning contribution, representing only two percent of total aerosol mass, was detectable in fine particles, underscoring the ability of the combined optical-chemical-trajectory approach to capture long-range transport of aged aerosols. These findings establish a framework for robust source attribution in environments where aerosol signals are subtle, emphasizing the importance of integrating multiple measurement types to accurately characterize aerosol dynamics.

Building upon this, the second manuscript demonstrated the feasibility and reliability of lunar photometry in Arctic conditions. Long-term observations at Barrow and Ny-Ålesund confirmed that lunar-derived AOD values are consistent with established solar photometry, with uncertainties only slightly higher than daytime measurements. This innovation not only enables year-round monitoring of aerosols in high-latitude regions but also provides a foundation for assessing nighttime radiative forcing and cloud–aerosol interactions. The ability to monitor aerosols continuously, independent of solar illumination, represents a major step forward in polar atmospheric research and opens new avenues for evaluating the climate impact of aerosols during the extended polar night.

The third manuscript expanded the spatial and temporal coverage to include fifteen Arctic and eleven Antarctic stations, combining solar, lunar, and ship-borne measurements to capture seasonal cycles and long-term trends in aerosol optical properties.

Results confirmed the pronounced seasonality of polar aerosols, with lower AOD and higher Ångström exponents during summer, reflecting cleaner air dominated by fine-mode particles, and higher AOD with lower exponents in winter-spring, consistent with the Arctic haze phenomenon and enhanced transport of mid-latitude anthropogenic emissions. In Antarctica, coastal stations exhibited higher summer AOD dominated by fine particles, whereas winter and spring were characterized by an increasing influence of coarse-mode sea-spray aerosols. Trend analyses revealed decreasing AOD at the European-influenced Arctic site of Andenes, likely due to emission regulations, while Antarctic stations such as Syowa and the South Pole exhibited increasing trends, suggesting evolving aerosol sources and transport pathways. These findings emphasize the importance of high-precision, multi-platform observations to capture regional and seasonal variability, as well as the dynamic responses of polar aerosols to anthropogenic and natural forcings.

Collectively, the results of this thesis provide critical insights into polar aerosol climatology and demonstrate the scientific value of combining innovative observational techniques with chemical and optical characterization. The work highlights how even subtle aerosol signals can be identified, attributed to their sources, and monitored across seasons and years, yielding a more complete understanding of their role in climate processes. At the same time, limitations remain, including uneven spatial coverage, particularly in the Russian Arctic, and data scarcity from the interior of Antarctica, which constrain the generalizability of some conclusions. Instrumental changes and differences across photometer models also introduce uncertainties in long-term trend analyses, underscoring the need for standardized, continuous observations.

Looking forward, future research should expand observational networks to undersampled regions, integrate multi-platform and satellite data, and further investigate episodic events such as wildfires and volcanic eruptions to quantify their impact on polar aerosol composition and radiative forcing. This thesis establishes a foundation for such endeavors, demonstrating the feasibility and value of high-precision, year-round aerosol monitoring in the harshest and most remote regions of the Earth. By bridging methodological innovation with multi-year, multi-site observations, this work has advanced our understanding of polar aerosol dynamics, highlighting the delicate interplay of natural and anthropogenic sources, seasonal cycles, and long-term environmental change. In doing so, it contributes not only to the scientific knowledge of polar atmospheres but also to the broader understanding of the Earth's climate system under rapidly evolving environmental pressures.

Acknowledgements

Pur riconoscendo l'importanza del sostegno ricevuto, ho scelto di non includere i ringraziamenti in forma scritta in questa tesi. Preferisco esprimere direttamente la mia gratitudine a chi mi ha accompagnato in questo percorso.

List of Figures

List of Tables